III-2

Materials Sciences

Highlight

BL7U

Electronic Structure of Triple- Layer Cuprate Superconductor $Bi_2Sr_2Ca_2Cu_3O_{10+\delta}$ Observed by ARPES

S. Ideta[1], T. Yoshida[2], S. Ishida[3], K. Takashima[4], S. Uchida[3], A. Fujimori[4] and K. Tanaka[1]

[1]*National Institutes of Natural Science, Institute for Molecular Science, Okazaki, 444-8585, Japan*
[2]*Graduate School of Human and Environmental Studies, Kyoto University, Kyoto 606-8501, Japan*
[3]*National Institute of Advanced Industrial Science and Technology (AIST), Tsukuba 305-8568, Japan*
[4]*Department of Physics, University of Tokyo, Tokyo 113-0033, Japan*

Effects of intra-multilayer interaction between the CuO_2 planes, which may contribute to the enhancement of the critical temperature (T_c) in the multi-layer high-T_c cuprate superconductors (HTSCs) [1], have been investigated to elucidate the mechanism of superconductivity. The Bi-based HTSC is classified by the number of the neighboring CuO_2 layers (n): single-layer ($n = 1$) $Bi_2Sr_2CuO_{6+\delta}$ (Bi2201), double-layer ($n = 2$) $Bi_2Sr_2CaCu_2O_{8+\delta}$ (Bi2212), and triple-layer ($n = 3$) $Bi_2Cr_2Ca_2Cu_3O_{10+\delta}$ (Bi2223). The T_c of optimally doped Bi2223, 110 K, is the highest among the Bi-family cuprates. In spite of both extensive experimental and theoretical studies [2-6], the microscopic origin of the T_c enhancement in the triple-layer HTSCs still remains unclear.

In recent ARPES studies of Bi2223, we have reported two bands originating from the outer and inner CuO_2 planes [7-9]. Here, we report an ARPES study of Bi2223 using low-energy photons with linear polarization along the Cu-O bond direction. We observed three bands and three Fermi surfaces (FSs) resulting from interaction between the three CuO_2 planes.

High-quality single crystals of optimally doped Bi2223 ($T_c = 110$ K) were grown by the travelling solvent floating zone method. ARPES experiments were carried out at BL 7U of UVSOR using linearly polarized light of $h\nu = 7$ eV - 8.5 eV. The total energy resolution and angular resolution were set at 7 - 8 meV and 0.05 deg, respectively. Temperature was set at $T = 12$ K and clean sample surfaces were obtained by cleaving the single crystals *in-situ* in an ultrahigh vacuum better than 7×10^{-9} Pa.

A schematic picture of FSs is shown in Fig. 1(a). The FS from the outer plane (previously denoted as OP) is split into two FSs due to the bonding and antibonding combinations of the two OPs, as denoted by OP-B and OP-A, respectively. Their superstructures due to the structural modulation of the BiO layer are also shown. Energy-momentum (E-k) intensity taken in the SC state along the momentum cuts indicated by black curves in panel (a) are shown in Figs. 1(b)-1(e). While the OP band is not clearly split near the nodal region [Fig.1(b)], away from the nodal region, this seemingly single feature splits into two dispersions as indicated by arrows for OP-B and OP-A bands.

In conclusion, we have observed the splitting of the triple-layer bands by ARPES. This result may give a key to elucidate the mechanism of the triple-layer cuprate superconductivity with the highest T_c of 110 K.
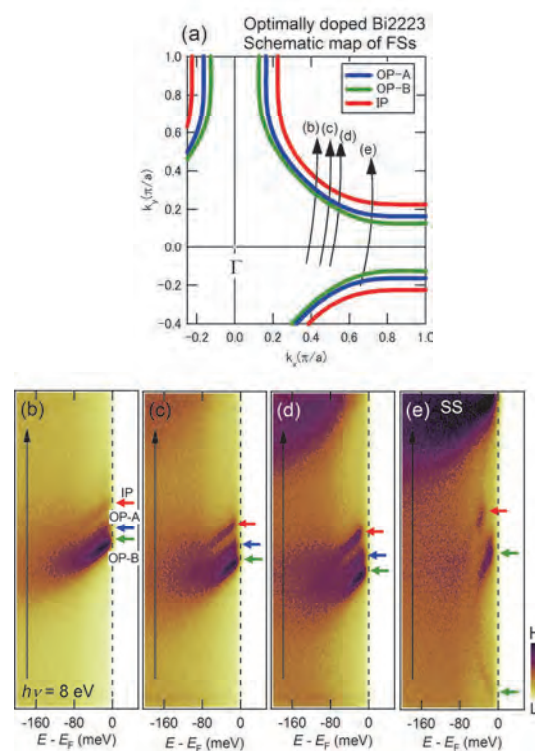

Fig. 1. Energy-momentum intensity plots in the Cu-O bond direction taken with $h\nu = 8$ eV at $T = 12$ K. ARPES intensity plots [(b)-(e)] correspond to cuts in panel (a). IP, OP-B, and OP-A denote the inner-plane, bonding outer-plane, and antibonding outer-plane bands, and SS is the superstructures.

[1] J. M. Wheatley *et al*., Nature **333** (1988) 121.
[2] E. Pavarini *et al*., Phys. Rev. Lett. **87** (2001) 047003.
[3] S. Chakcraverty *et al*., Nature **428** (2004) 53.
[4] S. Okamoto *et al*., Phys. Rev. Lett. **101** (2008) 156401.
[5] D. L. Feng *et al*., Phys. Rev. Lett. **88** (2002) 107001.
[6] T. Sato *et al*., Phys. Rev. Lett. **91** (2003) 157003.
[7] S. Ideta *et al*., Phys. Rev. Lett. **104** (2010) 227001.
[8] S. Ideta *et al*., Phys. Rev. B **85** (2012) 104515.
[9] S. Ideta *et al*., Physica C **470** (2010) S14-S16.

BL1B

Terahertz Spectroscopy of Solid Acid Proton Conductor
CsHSO₄ - CsH₂PO₄ Single Crystals

T. Awano

Faculty of Engineering, Tohoku Gakuin University, Tagajo 985-8537, Japan

Ⅲ-2

Proton conductors are interested because of the use in fuel cells. Those in medium temperature are important for eco-system in house with high efficiency. Inorganic solid acids such as $Cs_2(HSO_4)(H_2PO_4)$ crystal are newly discovered proton conductors in such medium temperature. Especially, this crystal keeps high ionic conductivity once after heating above 380 K. It is interesting to make clear the mechanism of such conductivity dependence on thermal history.

Meanwhile, terahertz spectral region is located between vibration and translation motion of the mobile ion. The "attempt mode" of conduction ion is also observed in superionic conducting crystals of silver, cuprous and alkali ions at the frequency as their atomic mass. This vibrational mode is directly connected with translational movement of conduction ion. Namely, the conduction ions surrounded by tetrahedral cage try to move out at this frequency.

Three methods have been reported for crystal growth of $Cs_2(HSO_4)(H_2PO_4)$. Haile who discovered this compound obtained it from stoichiometric aqueous solutions of cesium carbonate, sulfuric acid and phosphate acid [1]. By this method, both of $Cs_2(HSO_4)(H_2PO_4)$ and $Cs_3(HSO_4)_2(H_2PO_4)$ are grown. Other two methods were used by some groups. The one is growth from stoichiometric aqueous solutions of $CsHSO_4$ and CsH_2PO_4 [2]. The other is growth from stoichiometric sulfuric acid solution of CsH_2PO_4 [3]. $Cs_3(HSO_4)_2(H_2PO_4)$ also has superionic conducting phase at high temperatures [4]. The grown $Cs_2(HSO_4)(H_2PO_4)$ and $Cs_3(HSO_4)_2(H_2PO_4)$ single crystals were 0.2 mm × 2 mm × 6 mm and 5 mm × 8 mm × 15 mm in maximum size after one week growth, respectively.

Figure 1 shows reflectivity spectra of $Cs_3(HSO_4)_2(H_2PO_4)$. Anisotropic peaks were observed as shown in the figure. The proton conduction assisted by hydrogen bond with rotating of SO_4 or PO_4 tetrahedron occur along *b*-axis of the crystal. Reflectivity increase at low wave number region at the E//*b* spectrum at 300 K seems to be due to the proton conduction.

Figure 2 shows reflectivity spectra of $Cs_2(HSO_4)(H_2PO_4)$. Anisotropic peaks were observed also in these spectra, however, the difference was not so clear. Crystal structures of $Cs_3(HSO_4)_2(H_2PO_4)$ and $Cs_2(HSO_4)(H_2PO_4)$ are similar and corresponding peaks were observed. The high temperature phase is cubic and there was no difference with direction of electric field. Increase at low wave number was also observed at the 300 K spectrum.
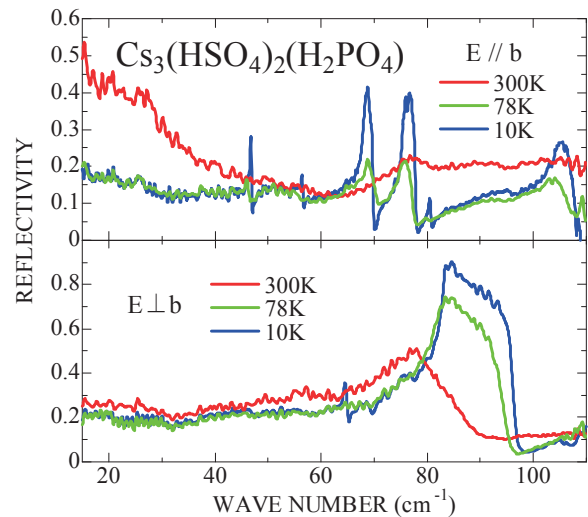

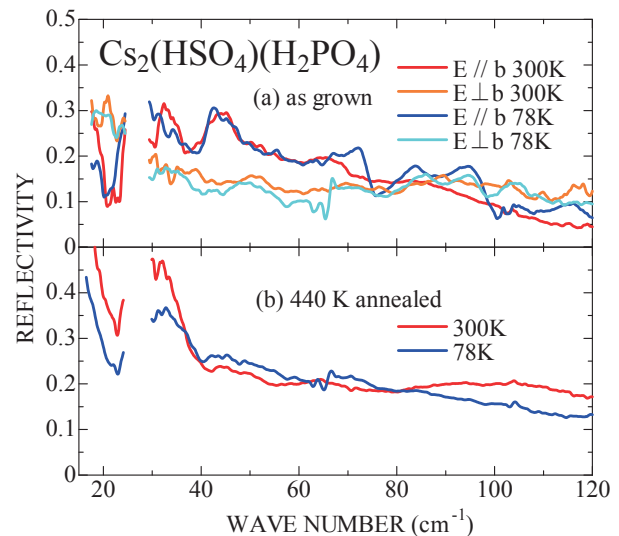Fig. 1. Reflectivity spectra of $Cs_3(HSO_4)_2(H_2PO_4)$ crystal from $CsCO_3$, H_2SO_4 and H_3PO_4.

Fig. 2. Reflectivity spectra of $Cs_2(HSO_4)(H_2PO_4)$ crystal from $CsHSO_4$ and CsH_2PO_4; (a) as grown (b) after heating at 440 K.

[1] C. R. I. Chisholm and S. M. Haile, Acta Cryst. B **55** (1999) 937.
[2] A. Matsuda, T. Kikuchi, K. Katagiri, H. Muto and M. Sakai, Solid State Ionics **177** (2006) 2421.
[3] Y. Yamane, K. Yamada and K. Inoue, Solid State Ionics **179** (2008) 483.
[4] S. M. Haile, G. Lentz, K.-D. Kreuer and M. Maier, Solid State Ionics **77** (1995) 128.

BL2B

Degradation of CH$_3$NH$_3$PbI$_3$ to PbI$_2$ Driven by Annealing in Vacuum

S. Tanaka[1], T. Kajikawa[1] and K. R. Koswattage[2]

[1]*Graduate School of Science and Engineering, Kindai University, Osaka 577-0818, Japan*
[2]*Center for Frontier Science, Chiba University, Chiba 263-8522, Japan*

Organolead halide perovskites have recently emerged as a photovoltaic material for high- efficiency organic photovoltaic [1-3]. The organolead halide perovskites have the advantageous characteristics for the photovoltaics such as the direct bandgap near the visible region, the small electron/hole effective masses, the large absorption coefficients, and long diffusion length of excited carriers, etc. The power conversion efficiency (PCE) of the organic photovoltaic used perovskites is approaching the PCE of silicon solar cells. However, there are several problems for practical use of the perovskite solar cells. One of the problems is its stability. A prototype organolead halide CH$_3$NH$_3$PbI$_3$ (MAPbI$_3$) shows degradation to PbI$_2$, a material has different electronic properties from those of the starting perovskite. As the degradation mechanisms of MAPbI$_3$, the chemical degradation through the interaction with water and the thermodynamic degradation through the creation of volatile molecular defects has been proposed [4]. In this report, we studied effect of the thermal annealing of MAPbI$_3$ on the electronic structure by using photoelectron spectroscopy to understand an impact of the decomposition of the perovskite structure.

Thin films of organolead halide perovskite MAPbI$_3$ were fabricated by the 2-step vapor deposition method at the Kindai University. As the first step, lead chloride (PbCl$_2$) was deposited on a pre-cleaned indium-tin-oxide substrate. Methylammonium iodide (CH$_3$NH$_3$I) was subsequently deposited on the PbCl$_2$ film as the second step. Upon CH$_3$NH$_3$I deposition, PbCl$_2$ reacted with CH$_3$NH$_3$I *in situ* and formed MAPbI$_3$ films. The fabricated samples were stored in dark, and transferred to the UVSOR BL2B. The samples were exposed in air before the photoelectron measurements. Hence the surface of samples would be partially degraded.

Figure 1 shows the photograph of the MAPbI$_3$ sample before and after annealing. The annealing treatment was performed in vacuum with a base pressure of 3×10^{-7} Pa. The annealing temperature and time were 140 °C and 10 min, respectively. During the annealing, the pressure was increased to 3×10^{-5} Pa. The red-brownish color of MAPbI$_3$ film was turned yellowish after the annealing treatment. This indicated the annealing treatment induced the degradation of MAPbI$_3$ to PbI$_2$. The photoelectron spectra of before and after the annealing treatment were measured with the photon energy of 100 eV. The results are shown in Fig. 2. The secondary cutoff of the sample was shifted toward higher kinetic energies after annealing. On the other hand, the Pb 5d core-levels were shifted toward lower kinetic energies after annealing. The

photoelectron signal from I 4d core-levels were also shifted toward lower kinetic energies with same values by annealing. (not shown here) The valence band region showed slight changes of shape but no significant shift of the valence band edge position. However, the signal-to-noise ratio of the spectrum was not adequate to detailed discussions about the valence band region.

The coordination number of Pb ions in the MAPbI$_3$ lattice is 6 and is also maintained in the PbI$_2$ lattice. Therefore, it is expected that the chemical environment for Pb ions in MAPbI$_3$ are similar that in PbI$_2$. Hence, the variation of kinetic energy of Pb 5d photoelectrons implies differences of the interaction from the surrounding molecules during the escape process. The shift toward the same direction of I 4d core-levels may also support this assumption. Further analysis of photoelectron spectra to understanding the effects of MAPbI$_3$ degradation is in progress.
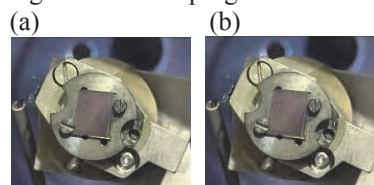

Fig. 1. Photograph of the CH$_3$NH$_3$PbI$_3$ thin film (a) before and (b) after annealing.
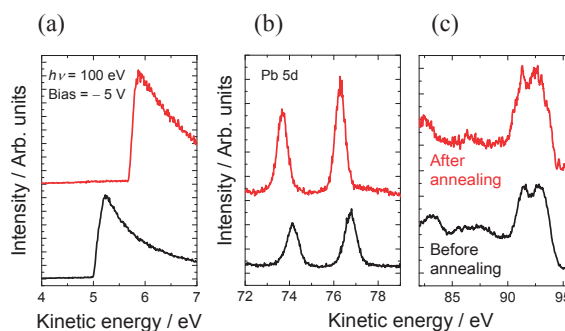

Fig. 2. Photoelectron spectra of (a) secondary electron cutoff, (b) Pb 5d and (c) valence band regions. Bias voltage of −5 V was applied for the secondary electron measurements. Black and red line are the photoelectron spectrum of before and after annealing treatment, respectively.

[1] A. Kojima *et al.*, J. Am. Chem. Soc. **131** (2009) 6050.
[2] M. M. Lee *et al.*, Science **338** (2012) 643.
[3] P. P. Boix *et al.*, J. Phys. Chem. Lett. **6** (2015) 898.
[4] I. Deretzis *et al.*, Appl. Phys. Lett. **106** (2015) 131904.

BL2A

Trial of Line Analysis for Si-Doped Porous Hydroxyapatite Prepared on Mg-Based Alloy

M. Sato[1], M. Togo[2] and A. Nakahira[2, 3]

[1]Institute for Materials Research, Tohoku University, Sendai 980-8577, Japan
[2]Graduate school of Engineering, Osaka Prefecture University, Sakai 599-8531, Japan
[3]Kansai Center for Industrial Materials Research, Tohoku University, Sakai 599-8531, Japan

Hydroxyapatite (HAp) has been widely used as alternate materials our hard tissue due to its excellent biocompatibility and osteo-conductivity. In addition, HAp also has protein absorption ability and ion-exchange ability. On the basis of these properties, we have prepared the functional element-doped HAp such as Mg, Si, Fe, Cu, and Ag by conventional wet process so far and investigated the effect of addition of those elements on generation phase, microstructure, and other properties. Since HAp powders are usually coating on the surface of implant in a practical use, structural investigation of these interface is important in order to perform of its full potential as artificial hard tissue. Hydrotermal Hot Press (HHP) is unique technique to obtain HAp bulk sample having a porous structure [1]. This porous structure has many advantages for bone formation. In this study, Si-doped HAp was grafted with AZ-31 (Mg-3Al-1Zn) alloy by HHP method, and elution behavior of Mg ion from AZ-31 substrate toward a HAp phase was investigated by XAFS measurement.

First of all, Si-doped amorphous calcium phosphate (ACP) powder was prepared by sol-gel method using calcium metal, tetraethyl orthosilicate (TEOS), phosphoric acid and ethanol at 273 K. Since the Ca/P ratio of obtained ACP powder is usually around 1.5, the obtained Si-doped ACP and $Ca(OH)_2$ powders were mixed so that their (Ca+Si)/P ratio is 1.67. And then, Si-doped HAp bulk sample was prepared on AZ-31 alloy by hydrothermal hot press method at 423 K for 2h. In order to obtain the interface information, obtained bulk sample was cut and polished, and synchrotron beam was irradiated respectively at the substrate, the interface and the HAp phase by changing a measurement position of sample. The Si K-edge and Mg K-edge XANES spectra for obtained bulk sample were corrected by fluorescence method using InSb and Beryl double crystal monochrometer and silicon drift detector (SDD) at BL2A in UVSOR, respectively. Figure 1 shows Si K-edge XANES spectra of Si-HAp prepared by HHP process obtained from interface and HAp phase. The obtained XANES spectra did not change by the obtaining position and resembled to that of calculated spectrum. This result indicate that the added Si ion exist into HAp structure and Si doped HAp bulk sample had been obtained by HHP technique. Moreover the shape of spectrum did not change by correcting position.

Figure 2 shows Mg K-edge XANES spectra of sample obtained at different position. Obtained

XANES spectra changed by changing the position, and that obtained from HAp phase showed similar spectrum to calculated spectra. This result indicates that the Mg ion eluted from substrate during HHP process forms a solid solution with HAp structure. In addition, spectrum obtained from near-interface has similar trend to that of $Mg(OH)_2$. From this result, it is suggested that the local structure around Mg atom changes gradually toward the HAp phase from substrate.
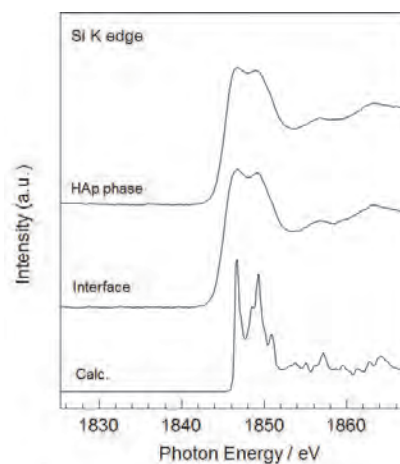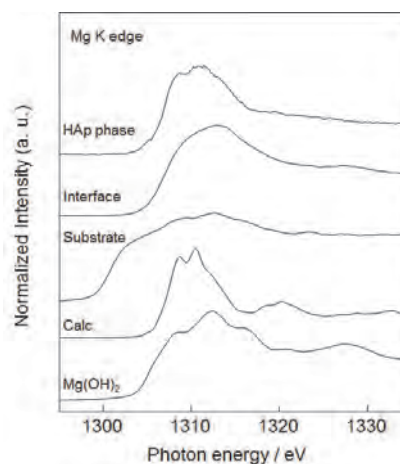

Fig. 1. Si K-edge XANES spectra of samples.

Fig. 2. Mg K-edge XANES spectra of samples.

[1] T. Onoki, S. Yamamoto, H. Onodera and A. Nakahira: Mater. Sci. Eng. C **31** (2011) 499.

BL2A

Mo L-Edge XANES Study on the Formation of Catalytically Active Mo Carbide Species on H-MFI for MTB Catalysts

H. Aritani[1], S. Mogi[1], N. Naijo[1], T. Sugawara[1], M. Akutsu[1], K. Kawashima[1] and A. Nakahira[3]

[1]Graduate School of Engineering, Saitama Institute of Technology, Fukaya 369-0293 Japan
[2]Advanced Science Research Laboratory, Saitama Institute of Technology, Fukaya 369-0293 Japan
[3]Graduate School of Engineering, Osaka Prefecture University, Sakai 599-8531 Japan

MTB (Methane To Benzene) reaction is one of a revolutionary process for direct conversion of natural gas to petroleum compounds, *i.e.*, from methane to benzene. Mo-modified H-MFI is a typical catalyst with high activity for MTB. During the methane dehydroaromatizaiton, Mo_2C-like active carbide species are formed on H-MFI catalysts. However, deactivation of MTB reactivity can not be avoided because of carbon contamination due to excess dehydrogenation of methane. In this case, structural change of active Mo species should be occur during the deactivation [1]. For highly active and durable reactivity for MTB reaction, detail of local structure of active Mo species and their structural changes needs to characterize. In the present study, Mo L_{III}-edge XANES study has been applied to characterize the active Mo species on H-MFI during the MTB reaction.

Catalyst samples were prepared by impregnation of each H-GaAlMFI (Si/Al_2=40) support with $MoO_2(acac)_2$−$VO(C_5H_7O_2)_3$−$CHCl_3$ solution (5wt% as MoO_3), and followed by dried and calcined at 773 K. The H-GaAlMFI (Al/Ga=100) supports were synthesized hydrothermally at 413 K for a week, and followed by ion-exchanging with NH_4Cl and calcined at 873 K. The catalytic MTB reactivity was evaluated by means of fixed-bed flow reaction at 1023 K, as described in a separate paper [1]. Mo L_{III}-edge XANES spectra were measured in BL2A of UVSOR-IMS in a total-electron yield mode using InSb double-crystal monochromator. Photon energy was calibrated by using Mo metal-foil. REX-2000 (Rigaku Co,) software was used for normalization of each XANES spectrum.

In our previous study, Mo-V (Mo/V=40) co-modified H-GaAlMFI (Al/Ga=100) catalyst shows higher activity and lower deactivation rate than Mo/H-MFI. In the case of Mo/H-MFI, partially carbonized Mo (Mo^{2+} and Mo^{4+}) species can be seen after CO pretreatment. Figure 1 shows the L_{III}-XANES spectra of reduced MoO_2 by CH_4(10-20%)-H_2 treatment at 973 K. Metallic Mo are formed, as well as the reduction with H_2. In this case, formation of Mo-carbide species such as Mo_2C can not be seen. In contrast, Mo_2C-like carbide species seems to be formed on the Mo-V/H-GaAlMFI catalyst by CO(2%)-H_2 treatment at 1023 K, as shown in Fig. 2. It suggests that Mo_2C-like carbide species are formed before the MTB reaction by CO pretreatment. After the MTB reaction, metallic Mo species are also seen during the reaction for 10-200 minutes. For Mo/H-MFI, formation of α-Mo_2C species

is remarkable during the MTB reaction after 60 minutes. These results indicate that formation of α-Mo_2C species relates to the deactivation, and inhibition of the carbonization is effective for high and durable MTB reactivity.
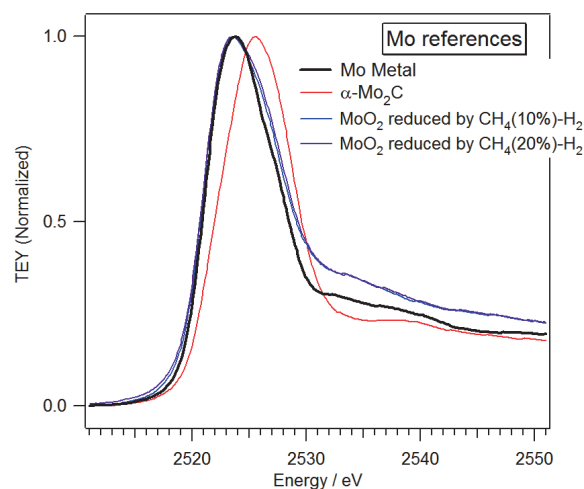

Fig. 1. Mo L_{III}-edge XANES of reference Mo compounds (Mo metal and α-Mo_2C) and reduced MoO_2 with CH_4-H_2 atmosphere at 973 K.
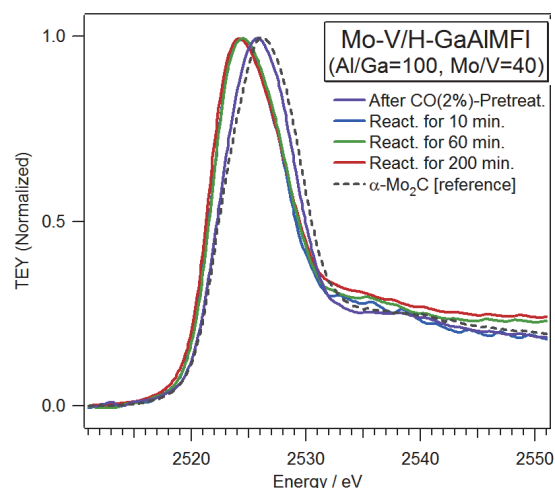

Fig. 2. Mo L_{III}-edge XANES of Mo-V/H-GaAlMFI catalysts after MTB reaction for 0-200 minutes at 1023 K.

[1] H. Aritani, H. Shibasaki, H. Orihara and A. Nakahira, J. Environm. Sci. **21** (2009) 736.

BL2A

X-Ray Absorption Near-Edge Structure Analysis of Yb Ions in Er-Doped CaZrO$_3$

A. Kanemoto[1] and T. Yamamoto[1,2]

[1]*Faculty of Science and Engineering, Waseda University, Tokyo 169-8555, Japan*
[2]*Institute of Condensed-Matter Science, Waseda University, Tokyo 169-8555, Japan*

Phosphor materials have been extensively studied because of their importance in industrial applications. Among them, rare-earth doped oxides with perovskite structures are very attractive inorganic phosphors, because of their luminescence efficiency and stability. In addition to such conventional phosphors, upconversion type phosphors, which can emit photons with higher energy (shorter wavelength) by irradiation of lower energy (longer wavelength) photons, have been also actively investigated. It was reported that Er doped CaZrO$_3$ shows such upconversion luminescence by irradiation of approx. 1000 nm photons to produce green emissions and additional Yb doping enhances luminescence intensity of Er-doped CaZrO$_3$ [1]. In order to understand the upconversion mechanism and the reason why Yb doping could enhance emission intensity, it is essential to know local environment of Yb ions in Er-doped CaZrO$_3$. In the current study, we tried to analyze electronic structure of dilute Yb ions in Er-doped CaZrO$_3$ by Yb-M X-ray absorption near-edge structure (XANES) measurements.

Samples were synthesized by the solid state reaction method. Reagent grade high purity powders of CaCO$_3$, ZrO$_2$, Er$_2$O$_3$ and Yb$_2$O$_3$ were weighed changing the concentration of Yb ions. These powders were mixed and ground in an agate mortar for 30 min, which were pressed into pellet form. Resultant pellets were sintered in air at 1673 K for 6 hrs.

Crystal structure of the synthesized specimens was examined by powder X-ray diffraction. Although tiny amount of secondary phases appears, majority of the sample specimens could be determined to be crystallized in orthorhombic perovskite structured CaZrO$_3$.

Yb-M XANES measurements were performed at BL2A of UVSOR. Incident beams were monochromatized with InSb double-crystal monochrometer. Sample powders were placed upon the carbon adhesive tape, which are attached on first Cu-Be dinode of the electron multiplier.

Observed Yb-M$_5$ XANES spectra of Yb codoped Er-CaZrO$_3$ were compared with that of Yb$_2$O$_3$, which are shown in Fig. 1. As shown in this figure, fine structures of Yb-M$_5$ XANES spectra of the samples here synthesized, i.e., Yb doped CaZrO$_3$:Er, are almost identical without any dependencies upon concentration of Yb ions in Er-doped CaZrO$_3$. In addition, those show similar profiles as that of Yb$_2$O$_3$. Hence it can be concluded that the doped Yb ions are trivalent state from the current XANES analysis.
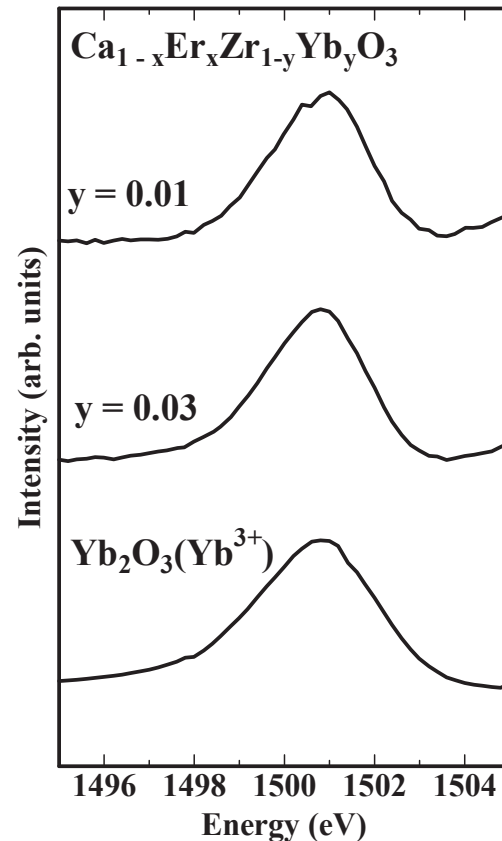

Fig. 1. Observed Yb-M$_5$ XANES spectra of Yb-doped CaZrO$_3$:Er and that of Yb$_2$O$_3$.

[1] V. Singh *et al.,* J. Appl. Phys. **112** (2012) 063105.

BL2A

Structural Evaluation of AlPO-5 Synthesized by Hydrothermal Process with XAFS

A. Nakahira[1, 2], M. Togo[1], H. Takahashi[1], K. Yoshikawa[1], M. Sato[3] and H. Aritani[4]

[1]Faculty of Engineering, Osaka Prefecture University, Sakai 599-8531, Japan
[2]Kansai Center, IMR, Tohoku University, Sakai 599-8531, Japan
[3]Institute of Materials Research, Tohoku University, Sendai 980-8577, Japan
[4]Saitama Institute of Technology, Fukaya 369-0293, Japan

ALPO-5 is one of the most popular aluminum phosphates ($AlPO_4$), although there are many of aluminum phosphate, generically known as "AlPO-n". These aluminum phosphates, AlPO-n, have the unique framework structures similar to zeolites. Also, they have unique microporous structures and are expected to be used as a catalyst and a molecular sieve [1-2]. Recently these microporous aluminum phosphates have attracted much attention, because AlPO-n framework can be incorporated with cationic species from monovalent to pentavalent. Also, the syntheses of heteroatom-doped AlPO-n were attempted to modify the microporous structures and enhance their properties through a variety of processing. For example, molecular-sieve catalysts of AlPO are significantly useful for the selective oxidation of linear alkanes, such as the catalytic oxidation in air of cyclohexane [3]. In this study, AlPO-5 were focused on among AlPO-n families. In special, the synthesis for AlPO-5 was attempted by hydrothermal process and the structural evaluations were carried out for samples by hydrothermal process.

AlPO-5 were synthesized by the hydrothermal method. $Al(OH)_3$ and aluminum alkoxide as an aluminum source and phosphoric acid as a phosphorus source were used. Furthermore, TEAOH (tetraethylammonium hydroxide) were used as an organic template. The molar composition of the hydrothermal synthesis materials was Al:P:TEAOH:H_2O = 2:2:X:250 (X=3~6).

These starting reagents were mixed under magnetic stirring and pH was maintained to be pH3 with H_2SO_4 solution. After aging for 1h, starting materials solutions were transferred into teflon-lined stainless steel autoclave and carried out by the hydrothermal treatment at 423 K to 463 K for 0 h to 48 h. After the hydrothermal treatments, obtained samples were collected with Buchner filter and washed with sufficient deionized water. And after drying at 323 K overnight, samples were crushed with agate mortar. The dried samples were characterized by X-ray diffraction analysis (XRD) and FT-IR and TG-DTA. Microstructures were observed with FE-SEM. The local structures around Al-*K* for the obtained products were characterized by measuring X-ray adsorption near edge structure (XANES) at BL2A in UVSOR.

Various aluminum phosphates were synthesized though hydrothermal treatment under a variety of hydrothermal conditions (hydrothermal temperatures, synthetic time, various pressures, and various starting materials).

The evaluation of X-ray diffraction analysis revealed that products obtained by the hydrothermal process at 443 K for 12 h to 48 h were identified to be crystalline AlPO-5 without another phase. SEM observation showed that products were rectangular with approximately 5 μm in length and 500 nm in diameter. Figure 1 shows the results of Al-*K* XANES spectra of AlPO-5 samples synthesized by the hydrothermal treatment for 0 h to 12 h. From these results, the local structure of Al-*K* XANES forAlPO-5 synthesized by the hydrothermal treatment for 12 h was different from ones for AlPO-5 samples synthesized by the hydrothermal treatment for 0 h to 8 h, suggesting that AlPO-5 local-structure was successfully synthesized by the hydrothermal treatment for 12 h.
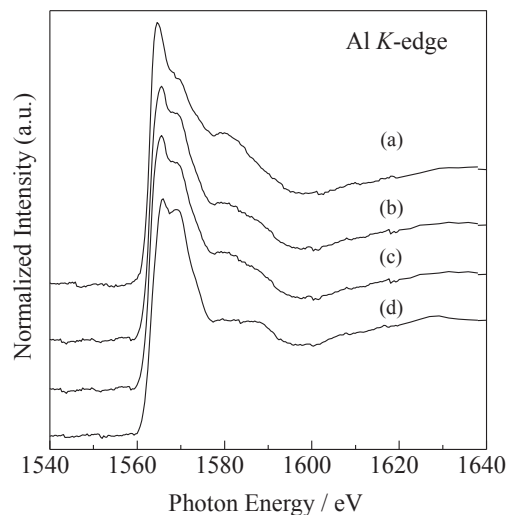

Fig. 1. Al-*K* XANES spectra of AlPO-5 synthesized by the hydrothermal treatment for 0 h to 48 h. (a) 0h, (b) 4h, (c) 8h, and (d) 12h.

[1] D. R. Pyke, P. Whitney, and H. Houghton, Applied Catalysis, **18** (1985) 173.
[2] D. Li, J. Yao and H. Wang, Progress in Natural Science: Materials International **22** (2012) 684.
[3] J. M. Thomas, R. Raja, G. Sankar and R. G. Bell, Nature **398** (1999) 27.

BL2A

In Situ Observation of the Dielectric Breakdown of Insulating Material Using Soft X-Ray Absorption Spectroscopy

E. Kobayashi[1], K. K. Bando[2], K. K. Okudaira[3] and T. Okajima[1]

[1]Kyushu Synchrotron Light Research Center, Tosu, 841-0005, Japan
[2]National Institute of Advanced Industrial Science and Technology, Tsukuba, 305-8565, Japan
[3] Chiba University, Chiba, 263-8522, Japan

Insulating materials are used in various parts of electric device. In recent years, it has become necessary to develop excellent insulating material with improvement in performance. In this study, the electronic state on aluminum oxide thin film under voltage applied conditions was studied by using near-edge X-ray absorption fine structure (NEXAFS). Aluminum oxide is recognized as an important material because it is the prototype of wide-gap insulator. The elementary processes of dielectric breakdown of insulating materials are not understood very well from a microscopic point of view.

An alumina film was made on a polished stainless steel plate by dip-coating with a diluted alumina sol (Kawaken Fine Chemicals, F1000). The coated plate was dried at 333 K, 6 hours and calcined at 573 K, 3 hours in an oven.

Al K-edge NEXAFS spectra of aluminum oxide thin film were measured at the beamline 2A of the UVSOR. The experimental setup for NEXAFS measurement is shown in Fig. 1. The soft x-ray was passed through a metal mesh and was irradiated to the sample. The fluorescence from sample was detected by silicon drift detectors. Potential of the sample was applied between the metal mesh and metal plate. All experiments were performed at room temperature.

Figure 2 shows the Al K-edge NEXAFS spectra of aluminum oxide obtained from PFY mode at various applied voltage. The spectra were measured while applying a voltage. This sample was breakdown at ~ 14 V. After breakdown, the potential to the sample could not be applied. These spectral features are almost same. And the spectra show two strong peaks at around 1569 eV and 1572 eV, respectively. These spectral features are also different from those of Al_2O_3 powder [1]. This indicates the local structure of Al in aluminum oxide thin film using in this study is different from those in Al_2O_3 crystal.

Inset of the Fig. 2 shows the expanded spectra at rising part of the spectra. The spectra with under applied voltages of 8 V show little energy shift. But the spectra at over 9.9 V are shifted slightly to the low energy side. Then, the spectrum after the breakdown was shifted significantly to the low energy side. This trend was also observed for an aluminum oxide thin film calcined at 473 K.
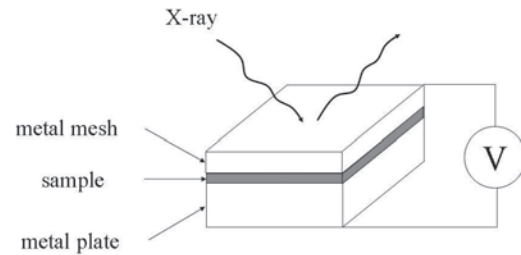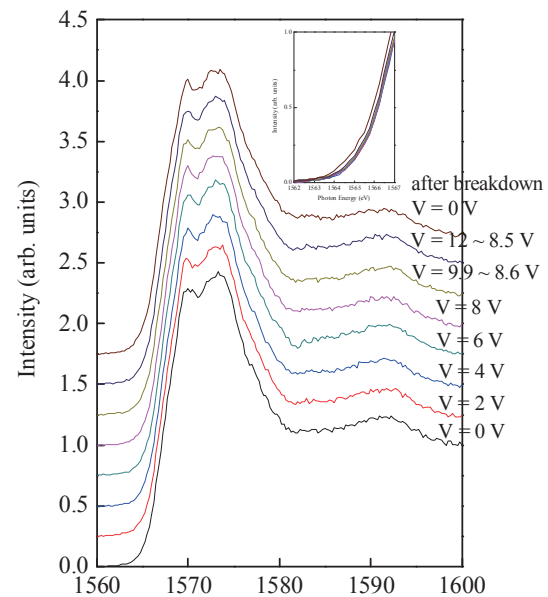

Fig. 1. Experimental setup.

Fig. 2. Al K-edge NEXAFS spectra of aluminum oxide thin film obtained from PFY mode at various applied voltage.

[1] M. Mogi *et al.,* Mat. Trans. **45** (2004) 2031.

BL3B

Material Dependence of Multiple Luminescence from Self-Trapped Excitons in Orthoborates with Complex Oxoabions upon Vacuum UV Excitation

N. Kodama, K.Yanagidaira, M. Kudo and T. Takahashi

Graduate School of Engineering and Resource Science, Akita University, Akita 010-8502, Japan

We report the temperature and material dependence of multiple intrinsic luminescence spectra from self-tapped excitons(STEs) in the three low-symmetry orthoborates with complex oxoanions : $LaSc_3(BO_3)_4$ (LSB), $Ca_4LaO(BO_3)_3$ (CLOB), and $YSc(BO_3)_2$(YSB). Furthermore, we examine the possibility of generating "multiple self-trapped excitons"(MSTE) in LSB, CLOB, and YSB crystals upon excitation by photons with more than twice the band gap energy, on the basis of STE excitation spectra in the VUV region.

Absorption spectrum of an LSB single crystal is shown in Figure 1. The absorption increased rapidly below about 200 nm. This result indicates that the band edge of LSB is around 200 nm. Moreover, the rise wavelength (rising) of absorption was in agreement with that of excitation. On the basis of this result, the rises around 200 nm were assigned to the band edges of LCOB and YSB, similar to that of LSB.

Figures 2(a), 2(b), and 2(c) show the temperature dependence of the intrinsic luminescence spectra for LSB, LCOB, and YSB, respectively, at 11 or 8 K, The luminescence spectra exhibited multiple bands of STE(I) and (II) (and/or (III)) for LSB, LCOB, and YSB, respectively, located at energies corresponding to the STE bands. The luminescence spectra for LSB under VUV excitation contained three distinct broad bands associated with STE(I), (II), and (III), with peaks at 245–272 nm, 311–320 nm, and 386–389 nm, respectively, in the range of 11–293 K, as shown in Fig. 1(a). For CLOB and LSB, three distinct broad bands (two weak bands and one intense band) appeared. These bands are associated with STE(I), (II), and (III), with peaks at 245–273 nm, 326–328 nm, and 410–413 nm, respectively, in the range of 8–293 K, as shown in Fig. 2(b). YSB exhibited one intense broad emission band, with the shortest wavelength of the three samples, associated with STE(I) with a peak at 247–254 nm, and another broad band associated with STE(II) with a peak at 290–296 nm in the range of 8–293 K

As the STE(I) emission intensity decreased in LSB and YSB, the STE(II) and STE(III) emission intensities increased. This suggests that there are multiple (three in LSB, two in YSB) local minima on the adiabatic potential energy surfaces, i.e., barriers for exciton self-trapping in LSB and YSB.

The decay times for the luminescence in LSB at 78 K were 20 ns for STE(I), 230 ns and 4.5 μs for STE(II), and 7.4 μs for STE(III). The decay times for the luminescence in CLOB at 78 K were 24 ns for STE(I), 540 ns and 2.0μs for STE(II), and 6.0 μs for STE(III). For YSB, the decay times for STE(I) and (II) luminescence at 293 K were 23 and 643 ns, respectively. Taking into account the above results, the site symmetry of the BO_3^{3-} oxoanion group, and the B-O bond length, we considered the structures and spin states of the STEs in LSB, CLOB, and YSB crystals. The existence of multiple stable structures and spin states for STEs in these crystals can be inferred from the temperature dependence of the intensities and

decay times of the STE luminescence, as follows. The fast decay components of STE(I) and STE(II) in LSB and CLOB and the fast component of STE(I) in YSB originate from singlet STE states in the BO_3^{3-} group with C_1 or Cs symmetry, respectively. In contrast, the slow components of STE(II) and STE(III) in LSB have been ascribed to a triplet STE with C_1 symmetry and those of CLOB have been ascribed to a triplet STE with Cs symmetry. Furthermore, the slow component of STE(II) in YSB is thought to originate from a triplet STE with C_1 symmetry.

The excitation spectra of LSB, CLOB, and YSB shown in Figs. 3(a), (b), and (c), measured at 293 K, 8 K, and 293 K, respectively, were detected at various fixed wavelengths. The excitation spectra of LSB increased stepwise in intensity with increasing excitation energy; that is, with decreasing excitation wavelength. The features of the excitation spectra below the band edge are very similar to those of CLOB and YSB. The excitation intensities at 90 nm for LSB, LCOB, and YSB were two to five times greater than at 180 nm, near the band edge. These results suggest that two or more electron–hole pairs are produced from one absorbed photon when excited by photons with energies greater than or equal to twice the band gap energy; that is, it may be possible to generate double- or multiple-self-trapped excitons (double- or multiple-STEs) in LSB, CLOB, and YSB.

Fig.1

Fig.2 (a) Fig.2 (b) Fig.2 (c)
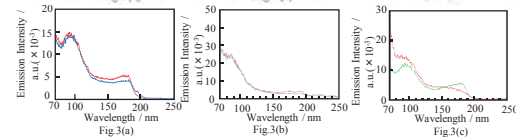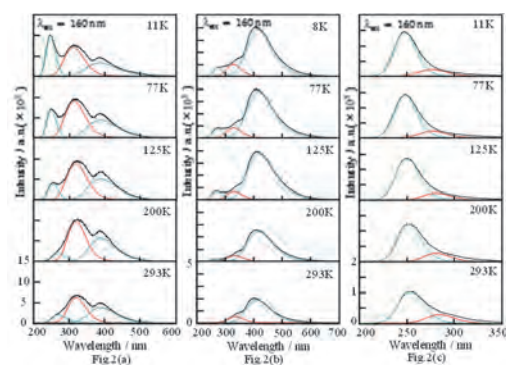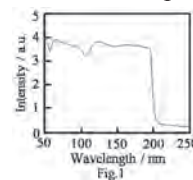

Fig.3(a) Fig.3(b) Fig.3(c)

Fig. 1. The absorption spectrum of an LSB single crystal at 293 K.

Fig. 2. Temperature dependence of intrinsic luminescence spectra in (a) LSB, (b) CLOB, and (c) YSB in the range of 11(8)– 293 K.

Fig. 3. Excitation spectra obtained by monitoring the intensity of the intrinsic luminescence at different fixed wavelengths in (a) LSB at 293 K, (b) CLOB at 8 K, and (c) YSB at 293 K.

BL3B

Transmittance Spectra and Other Properties of Metal Elements Doped LiCaAlF₆ Single Crystals

C. Tanaka[1], S. Kurosawa[2], Y. Yokota[2], A. Yamaji[1], R. Murakami[1], T. Horiai[1], H. Chiba[1],
Y. Ohashi[1], K. Kamada[2,3] and A. Yoshikawa[1,2,3]

[1] *Institute for Materials Research, Tohoku University, Sendai 980-8577, Japan*
[2] *New Industry Creation Hatchery Center (NICHe), Tohoku University, Sendai 980-0845, Japan*
[3] *C&A corporation, Sendai 980-8579, Japan*

Neutron detectors using neutron scintillators have been investigated to find their application in the homeland security scanning. A ^{3}He-gas proportional counter has been used widely as a conventional sensor for the thermal neutron detection due to the high capture cross-section for the thermal neutrons and the low sensitivity to γ-rays. However, the importance of alternative neutron detectors such as scintillators has increased due to the supply crisis of ^{3}He gas by the excessive demand. Therefore, the neutron scintillators have become gradually of interest as an alternative for the ^{3}He gas.

In the search for novel neutron scintillators, we have developed a LiCaAlF₆ (LiCAF) scintillator crystal containing ^{6}Li with the high capture cross-section for the thermal neutrons. In addition, the effective atomic number and density of the LiCAF are relatively low which results in the desired small detection efficiency for γ-ray.

The ns^2-type cations such as In$^+$ and Pb^{2+} are expected to show luminescence. In this study, we grew LiCAF crystals doped by the ns^2-type elements and investigated their properties to obtain a new candidate for the doping ion in the LiCAF crystal.

Non-doped and In, Pb-doped LiCAF crystals with the diameter of 2 mm were grown by a micro-pulling-down (μ-PD) method. We measured transmittance spectra of the polished specimens of non-doped and In, Pb doped LiCAF by the SI-Photodetector (AXUV 100 (IRD)) in the wavelength range from 80 to 300 nm at liquid helium temperature at BL3 of UVSOR.

Transmittance spectra of the Non-doped and In, Pb doped LiCAF are shown in Fig. 1. The spectrum of In-doped LiCAF has no remarkable difference from non-doped one except for the onset of the transmittance drop near the band-edge which is shifted towards longer wavelengths. This may be caused by some defects created by the doping. In the transmittance spectra of Pb doped LiCAF specimen an intense absorption peak was observed at 196 nm followed by other absorption peaks at shorter wavelengths and the band edge of LiCAF host at about 115 nm. Absorption peaks at 196 and 135 nm could be ascribed to the so called A and C absorption bands of the Pb^{2+} center [1].

Radioluminescence spectra of non-doped and Pb doped LiCAF crystals under X-ray irradiation were measured at RT. The emission peaks around 290, 380 and 510 nm were observed for non-doped LiCAF crystal, and were ascribed to self-trapped and trapped exciton [2]. In this wavelength region, an emission peak around 205-210 nm was observed and ascribed to Pb^{2+} center consistently with the previous report about the Pb doped LiCAF crystal [3]. In addition, we revealed that there was another emission peak around 830 nm in the long wavelength region. This emission peak can originate from defect in the structure due to nonstoichiometry of LiCAF lattice caused by Pb evaporation, or Pb$^+$ center like in the LiBaF₃ lattice which has the emission around 880 nm in [4].
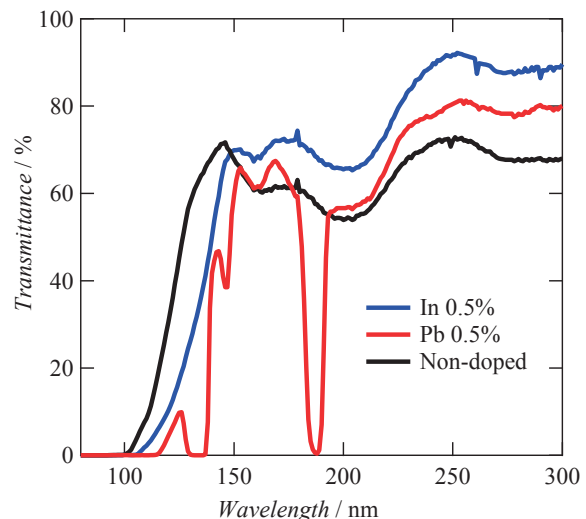

Fig. 1. Transmittance spectra of non-doped and In, Pb doped LiCAF in 80 – 300 nm at liquid helium temperature.

[1] P. W. M. Jacobs, J. Phys. Chem. Solids **52** (1991) 35.
[2] M. True, Y. Chen, M. Kirm, S. Vielhauer and G. Zimmerer, J. Lumin. **124** (2007) 279.
[3] A. Novoselov, J. Pejchal, M. Nikl and A. Yoshikawa, Nucl. Sci. Symp. Conf. Rec. N**45-7** (2007) 2184.
[4] L. Prado, N. D. Vieira Jr, S. L. Baldochi, S. P. Morato, J. P. Denis, N. Tercier and B. Blanzat, J. Phys. Chem Solids **57** (1996) 413

BL3B

Charge Transfer Luminescence of Ce-Doped and Undoped Ytterbium Pyrosilicate

T. Horiai[1], S. Kurosawa[2], R. Murakami[1], A. Yamaji[1], Y. Shoji[1, 3], J. Pejchal[4], Y. Ohashi[1, 3], K. Kamada[2, 3], Y. Yokota[2] and A. Yoshikawa[1, 2, 3]

[1]*Institute for Materials Research, Tohoku University, Sendai 980-8577, Japan*
[2]*New Industry Creation Hatchery Center (NICHe), Tohoku University, Sendai 980-8579, Japan*
[3]*C&A Corporation, Sendai 980-8579, Japan*
[4] *Institute of Physics CAS, Cukrovamicka 10, Prague, 162 00, Czech Republic*

Charge transfer (CT) luminescence of Yb^{3+} can have fast scintillation decay time, and such scintillation materials are expected to be applied to medical imaging. In previous study, the charge transfer luminescence of Ce-doepd Yb_2SiO_5 was evaluated, and the intensity became highest at near 40 K [1,2]. In this study, we search the CT luminescence for pyrosilicate group as the first step.

We prepared Ce-doped and undoped $Yb_2Si_2O_7$ single crystals grown by the micro-pulling-down method, and photoluminescence spectra for these samples were evaluated within 7.5-300 K at BL3 of UVSOR. The emission spectra were examined with a spectrometer (spectoropro-300i, Acton research).

Figures 1 and 2 shown the temperature dependences of the PL emission spectra for the undoped and Ce-doped $Yb_2Si_2O_7$ single crystals under 210 nm excitation in the temperature range of 7.5-300K, respectively. Since absorption edge was around 230 nm, the 210 nm photons were selected as an exaction source. Moreover, variations of the excitation wavelengths demonstrated that the strongest emission was observed at 210 nm excitation.

The undoped $Yb_2Si_2O_7$ had emission peaks at around 420 and 580 nm. The intensity of the 420 nm emission band was degraded when temperature of the specimen exceeded 100K, while that of the 580 nm band remained almost constant and independent on temperature. Thus, 420 nm band would be originated by CT system to $^2F_{5/2}$ of Yb^{3+}, and thermal quenching was observed. On the other hand, the emission at 580 nm may originate from defects.

Oppositely, the intensity of the 420 nm emission band of the Ce-doped $Yb_2Si_2O_7$ increased when temperature of the specimen became higher. Mainly this peak was assigned to Ce^{3+} 5d-4f emission, and CTS to $^2F_{5/2}$ of Yb^{3+}components can be included. 580 nm emission peak was also observed in the PL spectra of Ce-doped $Yb_2Si_2O_7$, while this emission was suppressed at RT. Moreover, from 200 to 300 K, Ce^{3+} emission intensity increased. Thus, the electron can be re-trapped into Ce^{3+} absorption band, and this result suggested energy transfer from this defect site to Ce^{3+}.
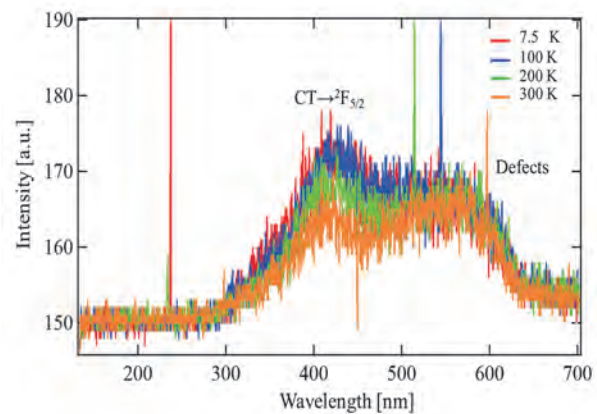

Fig. 1. The photoluminescence of undoped YbPS excited by 210 nm within 7.5-300 K.
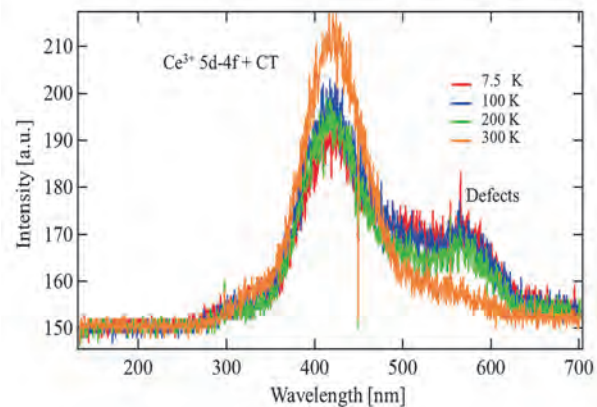

Fig. 2. The photoluminescence of Ce-doped YbPS excited by 210 nm within 7.5-300 K.

[1] L. V. Pieterson *et al*., J. Luminescnece **91** (2000) 177.
[2] D. W. Cook *et al.,* J. Luminescence **79** (1998) 185.

BL3B

Evaluation of the Bandgap Energies for Garnet-Type Infra-Red Scintillators

A. Yamaji[1], S. Kurosawa[1, 2], R. Murakami[1], T. Horiai[1], M. Kitaura[3], Y. Ohashi[1], K. Kamada[2], Y. Yokota[2], A. Ohnishi[3] and A. Yoshikawa[1,2]

[1] Institute for Materials Research, Tohoku University, Sendai 980-8577, Japan
[2] New Industry Creation Hatchery Center, Tohoku University, Sendai 980-8579, Japan
[3]Yamagata University, Yamagata 990-8560, Japan

Inorganic scintillator crystals have been widely used for radiation detection such as high energy physics, security applications and medical imaging. Recently, we have studied the real-time dose monitor system during the radiation therapy using scintillator with infrared emission. Radiation therapy is one of the primary treatments of tumor; however, radiation overdoses which cause medical accidents or under-doses which cause incomplete treatments have often been reported. Thus, real-time dose monitoring systems are required.

One of the concepts for the monitoring is the use of a 2-3 mm size scintillator material in the irradiated area (tumor) in the patient's body [1]. When the scintillator is irradiated with the incident X-rays, the intensity of the scintillation light give us information related to the dose in real time. Since human body had a low absorption region from approximately 700-1400 nm [2], scintillator with near infrared emission could be applied in the real time dose monitor system. Thus, we have investigated the optical and scintillation properties of some materials in the near infra-red region.

In this work, we grew garnet-type oxide crystals for scintillators with near infrared emission and evaluated their optical properties. Since the light yield depends on the band gap energy of a host crystal, we estimated the band-gap energies of the studied crystals. Band gap measurement is useful for the material design of scintillator.

The crystal growth of garnet-type oxide crystals were performed from the melt by the micro pulling down method using an Ir crucible with a radio frequency heating system. Nominal compositions of grown crystals were $Gd_3Ga_5O_{12}$ (GGG), $Lu_3Ga_5O_{12}$ (LGG), $Y_3Ga_5O_{12}$ (YGG) and $(Gd_{0.9}M_{0.1})_3Ga_{4.7}M'_{0.3}O_{12}$ (M = Mg, Ca, Sr and Ba, M' = Zr, Hf), respectively. The crystals were mechanically polished to the 1 mm thickness.

Transmittance spectra were measured at the beam line BL3B at the UVSOR facility; The specimens were glued on holes (1.5 mm diameter) of a copper plate with a silver paste (Fujikura Kasei, DOTITE D-550), and their temperature was kept at 8 K with liquid helium in order to suppress lattice vibrations. Transmitted light was detected with a silicon photodetector (IRD, AXUV 100).

The transmittance spectra were obtained as shown in Fig.1. Band gap energies were estimated from the absorption edges of these transmittance spectra. The calculated bandgaps are listed in table 1. These results contribute to the material design of scintillator with near infrared emission
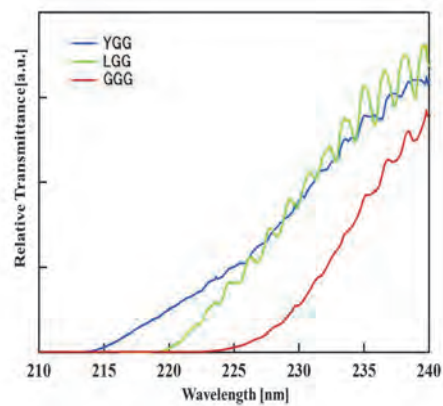

Fig. 1. Transmittance spectra of YGG, LGG and GGG crystals at 8 K.

Table 1. Bandgaps of garnet-type oxide crystals.

	Absorption band [nm]	Band gap [eV]
$Gd_3Ga_5O_{12}$	223	5.4
$Lu_3Ga_5O_{12}$	219	5.8
$Y_3Ga_5O_{12}$	214	5.7
$(Gd_{0.9}Mg_{0.1})_3Ga_{4.7}Zr_{0.3}O_{12}$	235	5.2
$(Gd_{0.9}Ca_{0.1})_3Ga_{4.7}Zr_{0.3}O_{12}$	236	4.9
$(Gd_{0.9}Sr_{0.1})_3Ga_{4.7}Zr_{0.3}O_{12}$	248	4.7
$(Gd_{0.9}Ba_{0.1})_3Ga_{4.7}Zr_{0.3}O_{12}$	254	4.6
$(Gd_{0.9}Mg_{0.1})_3Ga_{4.7}Hf_{0.3}O_{12}$	235	5.2
$(Gd_{0.9}Ca_{0.1})_3Ga_{4.7}Hf_{0.3}O_{12}$	238	4.9
$(Gd_{0.9}Sr_{0.1})_3Ga_{4.7}Hf_{0.3}O_{12}$	248	4.7
$(Gd_{0.9}Ba_{0.1})_3Ga_{4.7}Hf_{0.3}O_{12}$	255	4.6

[1] E. Nakata et al., Presentation at Radiological Society of North America (2008).
[2] Y. Y. Huang et al., Dose-Response (Prepress) Formerly Nonlinearity in Biology, Toxicology, and Medicine (2009).

BL3B

Determination of the Band-Gap Energy of (Gd, La)$_2$Si$_2$O$_7$ Scintillator Crystals Using the UVSOR Facility

R. Murakami[1], S. Kurosawa[2], A. Yamaji[1], M. Kitaura[4], T. Horiai[1], Y. Shoji[1,3],
Y. Ohashi[1], Y. Yokota[2], K. Kamada[2,3], A. Ohnishi[4] and A. Yoshikawa[1,2,3]

[1]*Institute for Materials Research, Tohoku University, Sendai, Japan*
[2]*New Industry Creation Hatchery Center, Tohoku University, Sendai, Japan*
[3]*C&A Corp., Sendai, Japan*
[4]*Yamagata University, Yamagata, Japan*

Inorganic scintillating materials are widely used for the medical imaging, oil well logging, astronomy, etc. Silicate scintillators such as Ce:Gd$_2$SiO$_5$ (Ce:GSO) and Ce:(Lu,Y)$_2$SiO$_5$ (Ce:LYSO) are applied in these fields, due to their high light outputs, short decay times, and so on. For example, Ce:GSO, has a good light output of ~12,500 photons/MeV and short scintillation decay time of ~56 ns [1]. Recent studies demonstrated that pyrosilicate-type crystals including Ce:Gd$_2$Si$_2$O$_7$ (Ce:GPS) and Ce:Lu$_2$Si$_2$O$_7$ (Ce:LPS) are also very promising scintillating materials [2,3]. Their light output exceeds that of Ce:GSO over two times [4]. Heavily Ce-doped (~10%) GPS crystals can be successfully grown from melt, and have the diameter over 1 inch. On the other hand, undoped GPS crystals cannot be grown from melt, because this material melts incongruently. However, heavily Ce-doped GPS crystals are not favorable, because high Ce concentration would lead to the degradation of light yield due to concentration quenching and self-absorption. In contrast, Ce:(Gd,La)$_2$Si$_2$O$_7$ (Ce:La-GPS) does not demonstrate the quenching problems. In Ce:La-GPS, part of Ce^{3+} is easily substituted with inactive La^{3+}, because both Ce^{3+} and La^{3+} have similar ionic radius [5].

Scintillation properties of Ce:La-GPS have been investigated using the crystals grown by the floating zone (FZ) method [5,6]. La 9% substituted crystal showed high light output (~36,000 photons/MeV) and high energy-resolution (~5.0%, 662 keV, FWHM) [5]. The FZ-grown crystals were a few mm in dimensions. Alternatively, the Ce:La-GPS crystals grown by the Czochralski (Cz) process were over 1 inch in diameter. It was also demonstrated that 25 - 50% La-substituted GPS crystals can be repeatedly grown by the Cz method [7].

Such pyrosilicate-type scintillators show high light output at high temperature. The light output of Tl:NaI, which have been used for oil well logging degrade to roughly 80% at 150˚C [8], while the light output of the Ce:La-GPS does not almost degrade at temperature over 150˚C [9]. One of the important keys is the tolerance for the photoionization, and it depends on the energy difference between the top of 5*d* level and conduction band. However, band-gap energy of La-GPS has not been reported; therefore, there are few guides for the material design.

We have succeeded the growth of undoped La-GPS with the chemical composition of (Gd,La)$_2$Si$_2$O$_7$ single crystals by the micro-pulling-down (μ-PD) method. The crystals with 1 mm thickness were cut from the ingots and were polished. The band-gap energies were determined at the BL3B beamline in the UVSOR facility. The transmittance spectra were measured at low temperature (~5 K) with the liquid He under ultra-high vacuum (~10^{-7} Pa). The band-gap energies were estimated to be 7.1 -7.2 eV.

[1] K. Takagi and T. Fukuzawa, Appl. Phys. Lett., **42** (1983) 43.
[2] C. L. Melcher *et al.,* Delft Unviersity Press (SCINT95), ISBN 90-407-1215-8, (1996) 309.
[3] S. Kawamura *et al.,* IEEE Nuclear Sci. Symp. Conf. Rec. (2006) 1160.
[4] S. Kawamura *et al.,* IEEE TNS **54** No.4 (2007) 1383.
[5] A. Suzuki, A. Yoshikawa *et al.,* Appl. Phys. Express **5** (2012) 102601.
[6] S. Kurosawa *et al.,* NIMA **744** (2014) 30.
[7] A. Yoshikawa *et al.,* Cryst. Growth Des., **15** (2015) 1642.
[8] Saint Gobain, NaI(Tl) Data Sheet, http://www.crystals.saint-gobain.com/uploadedFiles/SG-Crystals/Documents/NaI(Tl)%20Data%20Sheet.pdf
[9] S. Kurosawa *et al.,* NIMA **772** (2015) 72.

BL3B

Evaluation of Ce:(Gd, La)₂Si₂O₇ Scintillator Using an UVSOR Beam Line

S. Kurosawa[1], R. Murakami[2], Y. Shoji[2,3], A. Yamaji[2], T. Horiai[2], Y. Ohashi[2],
Y. Yokota[1], K. Kamada[1,3] and A. Yoshikawa[1,2,3]

[1]*Institute for Materials Research, Tohoku University, Sendai, Japan*
[2]*New Industry Creation Hatchery Center, Tohoku University, Sendai, Japan*
[3]*C&A Corp., Sendai, Japan*

Scintillators are used in various fields such as medical imaging, astronomy and so on. Evaluation of temperature dependences of some scintillation parameters such as light output and decay time is important to understand if the scintillation material is suitable for applications in low or high temperature conditions.

In oil well logging, scintillator is exposed to temperatures above 350 K measuring the subsurface geologic formation properties. Therefore, scintillator with a high light output even at high temperatures is required.

Recently, scintillation properties of $(Ce_{0.01}, Gd_{0.90}, La_{0.09})_2Si_2O_7$ (Ce:La-GPS) have been reported. The Ce:La-GPS crystal had a light output of approximately 35,000 photons/MeV, FWHM energy resolution of 5.0% at 662 keV [1,2]. Moreover, the light output over 35,000 photons/MeV was found constant in the temperature range from 0 to 423 K. In addition, FWHM energy resolution of Ce:La-GPS (roughly 7–8%) at 662 keV remained constant up to 373 K [3]. Thus, this crystal can be applied to oil well logging or other radiation detection application at high temperature conditions.

In this study, we evaluated luminesce properties of Ce:La-GPS in low temperature in BL3B of UVSOR. The luminescence was measured with a spectrometer (spectoropro-300i, Acton research) consisting of a CCD camera from approximately 5 – 300 K.

Figure 1 shows the emission intensity around 390 nm originated from $5d$-$4f$ transition of Ce^{3+} as function of temperature, where excitation wavelength was approximately 240 nm originated from $4f$-$5d_4$ translon of Ce^{3+}. This result showed that the luminescence intensity remained constant, not only up to 400 K, also down to 5 K.

Compared with other scintillation materials, we found the invariable properties is rare case; in general, intensities of several scintillators doped with Ce^{3+} increase as temperature fall or disappear at low temperature (5-100 K). Thus, we found Ce:La-GPS has "strange" and "unique" temperature dependence.

We also measured thermo-luminesce for this material in UVSOR (BL3B), and we found that this material had small number of traps between valence and conduction band compared with conventional scintillators. Some traps would suppress the light output (luminance intensity), and the suppression from the traps are related to temperature. Thus, the small number of traps would be related to be "strange" and

"unique" temperature dependence.

Moreover, we also measured the bandgap energy of La-GPS in UVSOR, and this material had wider gap energy than conventional scintillators [4]. This wide bandgap can be related to the "strange" and "unique" temperature dependence in high temperature region (up to approximately 400 K), because, in this case, the energy difference between the bottom of the conduction band and excitation band of Ce^{3+} ($5d_1$ level) can be wider than conventional scintillators. Due to the wide energy, even in high temperature, electron located in excitation band of Ce^{3+} can de-excite to grand state of Ce^{3+} ($4f$), and a scintillation photon is generated. On the other hand, in the case of the low difference, electrons tend to move from the excitation band of Ce^{3+} to conduction band, and light output is quenched.
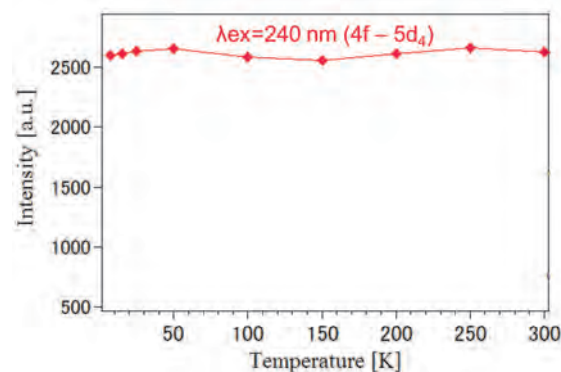

Fig. 1. Intensity of Ce^{3+} $5d$-$4f$ transition as a function of temperature.

[1] A. Suzuki, S. Kurosawa, A. Yoshikawa *et al.,* Applied Physics Express **5** (2012) 102601.
[2] S. Kurosawa, A. Yoshikawa *et al.*, Nucl. Inst. and Meth. in Phys. Res. A **774** (2014) 30.
[3] S. Kurosawa, A. Yoshikawa *et al.,* Nucl. Inst. and Meth. in Phys. Res. A **772** (2015) 72.
[4] R. Murakami and S. Kurosawa, UVSOR Activity Report, submitted.

BL3B

Thermoluminescence of SrHfO₃ Ceramics

H. Chiba[1,] S. Kurosawa[1,2,] R. Murakami[1,] A. Yamaji[1,] Y. Ohashi[1,] J. Pejchal[1,3,] K. Kamada[2,4,]
Y. Yokota[1,2] and A. Yoshikawa[1,2,4]

[1]Institute for Materials Research, Tohoku University, Sendai 980-8577,Japan
[2]New Industry Creation Hatchery Center(NICHe), Sendai 980-8579,Japan
[3]Instiue of Physics, AS CR, Cukrovarnická 10,162 53 Prague ,Czech Republic
[4]C&A Corporation, Sendai 980-8577,Japan

In Positron Emission Tomography (PET), Lutetium based scintillators are typically used because of their good performance and high density. However, Lu-containing scintillators have high-rate intrinsic background of roughly 300 counts/s/cm^3 because natural abundance of ^{176}Lu radio isotope (beta emitter) is 2.59%. This is why Lu-containing scintillators can have worse sensitivity. Hafnium has a high atomic number of 72, and the abundance of its only radioisotope is less than 0.2% (^{174}Hf, half-life is more than 1015 year). Thus, a new scintillator containing Hafnium can have low intrinsic background and high detection efficiency.

Recently, SrHfO₃ doped with Ce (Ce:SHO) has attracted attention as a scintillating material due to a high density of 7.65 g/cm^3, a high effective atomic number of 64 and negligible intrinsic-background [1]. Al/Ce:SrHfO₃ ceramics can be prepared by the Spark Plasma Sintering(SPS) method due to the high melting point of Hafnium [2]. It has improved optical properties and radiation response when compared to the Al-free material.

Considering the above, we fabricated Al/Ce:SrHfO₃ by the SPS method; For starting materials, HfO_2 (99.95% pure), $SrCO_3$ (99.99% pure), α-Al_2O_3 (99.99% pure), CeO_2 (99.99% pure) powders were used. Ce:SHO ceramic samples were pre-sintered in a chamber filled with air. SHO ceramic samples were prepared from the SHO powder using a 10-mm-diameter carbon punch and 30-mm-diameter carbon dies, SPS chamber (Fuji Denpa, DR.SINTER)

We used carbon punch and dies were used in the sintering process under vacuum, strongly reduction environment is established. This leads to creation of the oxygen vacancies in the material. These defects decrease the light output of the samples, they need to be investigated to optimize the material performance. Thus, thermoluminescence method was employed.

In BL3B of UVSOR, we used thermoluminescence measurement from 4 K to room temperature for SrHfO₃ samples; The samples were irradiated at 220 nm for 10 minutes at very low temperature 4~6 K. After the irradiation, we raised temperature slowly and measured the emission intensity with a CCD.

The thermoluminescence glow curve is shown in Fig.1hawse can observe some peaks from 100 to 200K, and these peaks may originate from Oxygen defects.

As for future plans, we will investigate how the annealing can diminish Oxygen defects concentration using the same method.
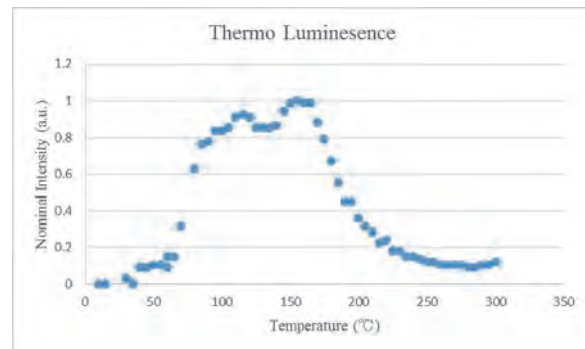

Fig. 1. Thermo Luminescence spectra of AlCeSrHfO₃.

[1] E. Mihóková, V. Jary´, L. S. Schulman and M. Nikl, Chemical Physics Letters (in press).
[2] S. Kurosawa et al., Radiat. Meas.**56** (2013) 155.
[3] S. Blahuta et al., IEEE Transaction on Nuclear Science NS **60** (2013) 3134.

BL3B

Study of Emitting Mechanism on UV Emitting ZnAl$_2$O$_4$ Phosphor Using Vacuum Ultra Violet Photoluminescence System

H. Kominami[1], T. Ito[1] and S. Kubota[2]

[1]Graduate School of Integrated Science and Technology, Shizuoka University, Hamamatsu 432-8651 Japan
[2]Faculty of Engineering, Shizuoka University, Hamamatsu 432-8651 Japan

In our previous work, it was found that ZnO-based oxide materials showed UV emission under excitation by electron beam. Especially, ZnAl$_2$O$_4$ showed strong UV emission peaked around 250 nm. However, the basic property and the emission mechanism of ZnAl$_2$O$_4$ were not cleared. For the evaluation of the physical properties, it is difficult to evaluate because it is the influence of surface scattering, such as the absorption coefficient and refractive index reflectance. By thinning the ZnAl$_2$O$_4$, we thought that it is possible to evaluate these fundamental properties and the mechanism of UV emission from ZnAl$_2$O$_4$. In this study, ZnAl$_2$O$_4$ thin firm was prepared by sputtering and thermal diffusion to the sapphire substrate.

ZnAl$_2$O$_4$ thin films was prepared by thermal diffusion of ZnO film to sapphire substrate. After deposition, the films were annealed in air. From crystal analysis, ZnAl$_2$O$_4$ polycrystalline was obtained.

Figure 1 shows CL spectra of the ZnAl$_2$O$_4$ thin films before and after annealing for 2, 100 and 200 hours, respectively, excited at anode voltage of 10 and 4 kV and sample current density of 30 μA/cm^2. Both films showed UV emission from ZnAl$_2$O$_4$. From the spectrum of 2 hours annealing, in spite of ZnO thick film was still remained, the visible emission around 500 nm was not appeared. CL intensity of 100 hours annealed film showed 25 times stronger than that of 2 hours annealing. In other words, it suggested that the not only increasing of thickness but also improvement of crystallinity of ZnAl$_2$O$_4$ film by longer annealing time.

Figure 2 shows PL excitation spectra of ZnAl$_2$O$_4$ powders prepared by different ZnO/Al$_2$O$_3$ ratio. The excitation band was shifted to higher energy when Zn/Al ratio was decreased. It indicates that Zn/Al ratio was influenced the optical properties. The red line in the figure is the transmittance spectrum of ZnAl$_2$O$_4$ thin film. The absorption edge was closed to lower ZnO/Al$_2$O$_3$ ratio. It seems that the film was not stoichiometry. Moreover, the refraction index and dielectric constant were not obtained from the analysis of transmittance and reflection spectra. It was thought that the ZnAl$_2$O$_4$ film was not uniform and clear the boundary between ZnAl$_2$O$_4$ and substrate. To obtain the optical parameters such as refraction index and dielectric constant, it is necessary to prepare the film which is clear boundary at the each layer.
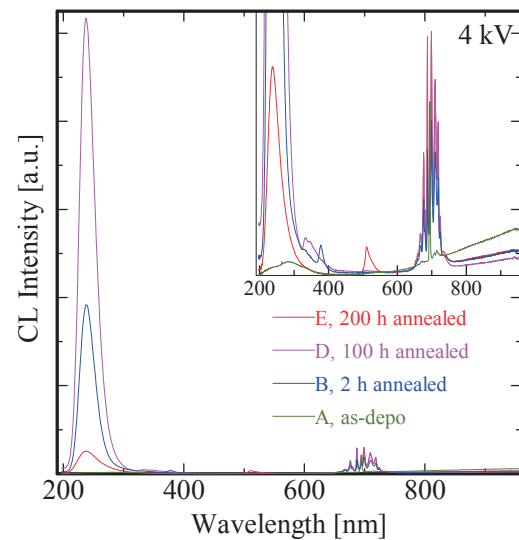

Fig. 1. Cathodoluminescence of ZnAl$_2$O$_4$ thin films prepared by thermal diffusion of ZnO and sapphire substrate, excited by anode voltages of 4 and 10 kV and sample current density of 30 μA/cm^2.
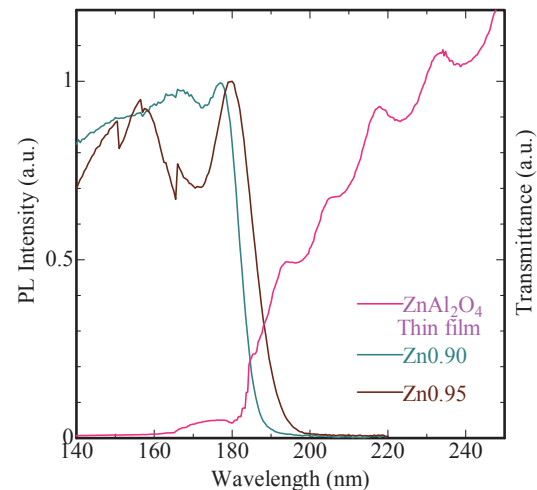

Fig. 2. Photoluminescent excitation spectra of ZnAl$_2$O$_4$ powders and transmittance spectrum of ZnAl$_2$O$_4$ thin film measured at BL3B.

BL3B, BL7B

PL Spectra of Laser Irradiated *a*-CN$_x$ Thin Films

K. Nakamura[1], K. Ikeda[1], K. Fukui[1] and K. Yamamoto[2]

[1]Department of Electrical and Electronics Engineering, University of Fukui, Fukui 910-8507, Japan
[2]Far-infrared region Development Research Center, University of Fukui, Fukui 910-8507, Japan

Amorphous carbon nitride (*a*-CN$_x$) is known to have an interesting mechanical, electrical and optical properties. Therefore, it has been actively carried out research on synthesis, structure and properties. The *a*-CN$_x$ has also been expected as an inexpensive white light emitting diode material. However, since the optical properties of *a*-CN$_x$ are sensitive to the preparation conditions, photoluminescence (PL) spectra of the samples evaporated under same conditions are, in some cases, different with each other. Recently, it is found that laser irradiated *a*-CN$_x$ thin films after depositing show much higher PL intensity than those of as-deposited *a*-CN$_x$ thin films, and their PL spectra have better reproducibility [1,2]. In this report, we show the RF power dependence of the combined excitation emission spectra (CEES) by using laser irradiated *a*-CN$_x$ thin films.

All samples on Si substrates are deposited about 1 μm by the RF-sputtering method at Ryukoku University [1]. The sputtering conditions with graphite target in the low pressure nitrogen gas environment of every samples are same without RF power of 40 W, 60 W and 100 W. Beam diameter of laser-irradiation is about 1.2 mm, and irradiation time is 240 minutes by using He-Cd laser (325 nm) with 20 mW. All CEES measurements have been performed at BL3B and BL7B at about 20 K.

Figure 1 shows CEES of RF power 60 W *a*-CN$_x$ thin film. High intensity regions are represented by warm colors. It is found that the PL peak is located around 2.8 eV, and peak energy has no excitation energy dependence. It means that this emission process is unique process upon the band to band excitation of *a*-CN$_x$. Figure 1 also suggest that this PL is strongly excited around 4.5 eV and 5.5 eV. Both the excitation energy independence of the PL peak and the existence of two peaks (4.5 eV and 5.5 eV) in the excitation spectra are observed in both 40 W and 100 W *a*-CN$_x$.

Figure 2 shows the emission spectra at the excitation energy 4.6 eV for all samples. All spectra normalized by the maximum intensity. Although it is clear that the emission peak is shifted to lower photon energy side with an increase of the RF power, these three samples are emitted almost same photon energy region from 1.6 eV to 4.0 eV. In addition to the asymmetric spectral shape of these emission bands, it probably suggests that these PL bands consists of many emission bands which are continuously distributed from 1.6 eV to 4.0 eV, and RF power affects the distribution of the *a*-CN$_x$ component which corresponds to each emission band.

In summary, we measured the combined excitation emission spectra of laser irradiated *a*-CN$_x$ thin films.

Upon band to band excitation, *a*-CN$_x$ thin film show a wide visible range emission band. This band consists of many emission bands which reflect the variation of the *a*-CN$_x$ components and/or structures. However, all emission bands are commonly excited same two photon energy range around 4.5 eV and 5.5 eV.
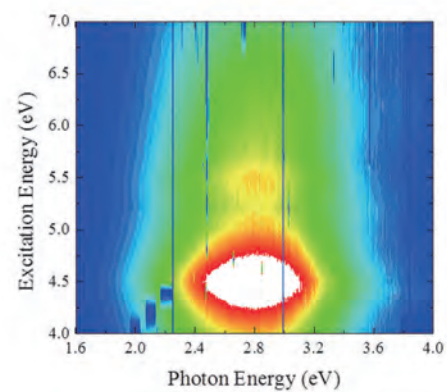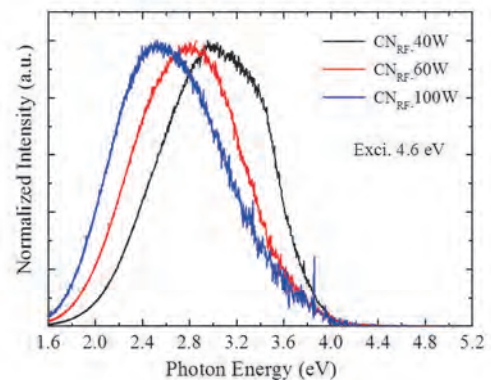

Fig. 1. CEES of a-CNRF-60W at 9K.

Fig. 2. Emission Spectrum at 9K.

[1] M. Satake *et al.,* 2013 JSAP Autumn Meeting 28p-PB3-11.
[2] D. Itoh *et al.,* UVSOR Activity Reports **41** (2014) 68.

BL3B

Energy Transfer from I⁻ Centers to In⁺ Centers in Co- Doped NaCl:I⁻, In⁺ Crystals

A. Iguchi and T. Kawai

Graduate School of Science, Osaka Prefecture University, Sakai 599-8531, Japan

Ⅲ-2

Alkali halide crystals have the wide band-gap up to the vacuum ultraviolet energy region and are a suitable candidate host for doping of impurity ions. Though optical studies for impurity centers doped in the alkali halide crystals have been extensively performed, energy transfer between two kinds of impurity centers in co-doped alkali halide crystals is comparatively less studied [1,2]. In this study, we have investigated the energy transfer from I⁻ centers to In⁺ centers in NaCl crystals co-doped with the I⁻ and In⁺ ions at the BL-3B line of UVSOR.

Figure 1 shows the absorption spectrum of NaCl:In⁺ and the luminescence spectrum of NaCl: I⁻ in the energy range from 4.4 to 6.0 eV. In NaCl:In⁺, the absorption band observed around 5.2 eV is called the C absorption band and is attributed to the intra-ionic transition from the $^1A_{1g}$ to $^1T_{1u}$ states [3,4]. In NaCl:I⁻, the luminescence band appearing around 5.3 eV is called the NE luminescence band and comes from the one-center type localized exciton, which is localized mainly on the central site of a substituted I⁻ impurity with small lattice relaxation [5]. The NE luminescence band in NaCl:I⁻ has an large overlap with the C absorption band in NaCl:In⁺. The fact indicates the potential of the energy transfer from the I⁻ centers to the In⁺ centers in co-doped NaCl:I⁻, In⁺ crystals. According to the Förster model [6,7], the critical distance between both centers for resonant energy transfer is estimated to be about 3.0 nm from the overlap with the luminescence and absorption bands.

Figure 2 shows the excitation spectra in NaCl:I⁻, NaCl:In⁺, and co-doped NaCl:I⁻,In⁺ crystals at room temperature (RT). The NE luminescence band in NaCl:I⁻ is efficiently excited in the energy region around 6.4 eV and 7.3 eV, where the absorption band due to the I⁻ centers is located. In NaCl:In⁺, the luminescence band at 3.0 eV, which comes from the In⁺ centers, is efficiently excited at the C absorption bands of the In⁺ centers.

In the co-doped NaCl:I⁻,In⁺ crystal, the excitation spectrum for the 3.0 eV luminescence band of the In⁺ centers has the broad band around 5.7 eV in addition to the C band of the In⁺ centers. Since the 5.7 eV band corresponds to the excitation band for the NE luminescence band in NaCl:I⁻, the fact implies the existence of the energy transfer from the I⁻ centers to the In⁺ centers in the co-doped NaCl:I⁻, In⁺ crystal. In order to clarify the energy transfer mechanism from the I⁻ centers to the In⁺ centers in the co-doped NaCl:I⁻, In⁺ crystals, the measurements of the decay kinetics of the luminescence are needed.

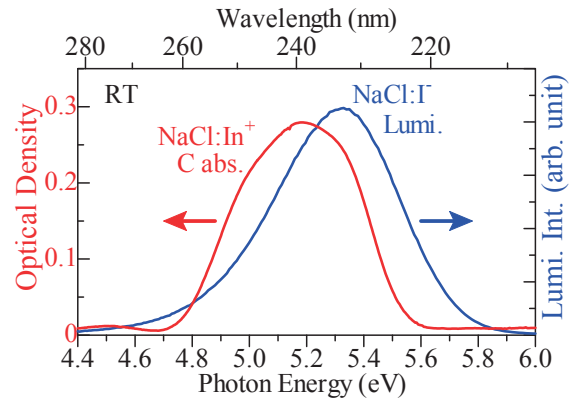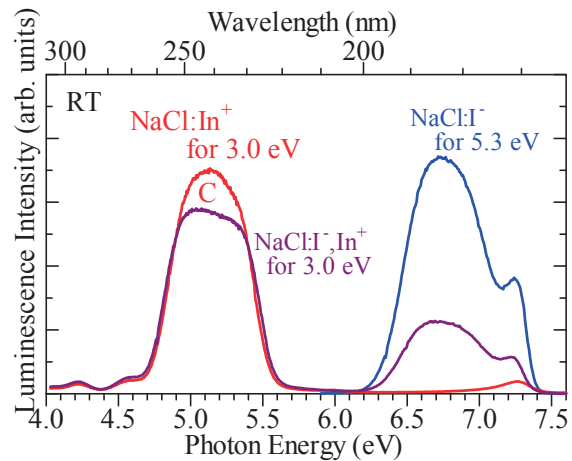Fig. 1. Luminescence spectrum (blue) of NaCl:I⁻ and absorption spectrum (red) of NaCl:In⁺ at RT.

Fig. 2. Excitation spectra of NaCl:In⁺ (red), NaCl:I⁻ (blue), and co-doped NaCl:I⁻, In⁺ (purple).

[1] A. F. Muñoz and J. O. Rubio, Phys. Rev. B **38** (1988) 9980.
[2] A. Méndez *et al.*, J. Lumin. **79** (1998) 269.
[3] A. Ranfagni *et al.*, Advances in Physics **32** (1983) 823.
[4] P. W. M. Jacobs, J. Phys. Chem. Solids **52** (1991) 35.
[5] I. Akimoto *et al.*, Phys. Status Solidi C **6** (2009) 342.
[6] T. Förster, Disc. Faraday Soc. **27** (1959) 7.
[7] D. L. Dexter, J. Chem. Phys. **21** (1953) 836.

BL3B

Luminescence of Copper-Heavily-Doped Cesium Iodide Crystals

T. Hirai[1] and T. Kawai[2]

[1] College of Science and Engineering, Ritsumeikan University, Kusatsu 525-8577, Japan
[2] Graduate School of Science, Osaka Prefecture University, Sakai 599-8531, Japan

Impurity ions doped into insulating materials, such as Tl: CsI and Tb: Gd_2O_2S, have been widely used as scintillators in γ- and X-ray detectors. In order to remarkably improve performance of those detectors, attempts have been recently made to develop a new type of scintillator utilizing semiconductor microcrystals instead of the impurity ions, since the radiative recombination rates of excitons in semiconductor microcrystals should be much higher than those in the impurity ions [1]. In the present study, we have focused on microcrystals of semiconducting Cu compounds that can be formed in a CsI crystal [2]. We have investigated photoluminescence (PL) and photoluminescence excitation (PLE) spectra of Cu heavily doped into CsI bulk crystals, which were prepared by the Bridgman method, by use of synchrotron radiation at the BL3B line in UVSOR.

Figure 1 shows a PL spectrum (black) of a Cu (10 mol%): CsI crystal at 5 K under excitation at 200 nm, which corresponds to the band-to-band excitation of CsI. A strong PL band is observed at 440 nm. A weak PL band can be also observed at around 405 nm as a shoulder of the PL band at 440 nm. In addition, there appear two PL bands at 290 and 340 nm, which originate from radiative recombination of self-trapped excitons (STEs) in CsI [3]. Three PLE spectra detected at 340 (violet), 440 (red) and 405 (blue) nm are also shown in Fig. 1. The PLE spectrum for the 340-nm PL band corresponds to that for the PL bands of STEs in CsI. In the PLE spectrum for the 405-nm PL band, two PLE bands are observed at 260 and 280 nm. For the 440-nm PL band, there appear three PLE bands at 245, 270 and 290 nm.

In Fig. 2, a PL spectrum (black) of a Cu (40 mol%): CsI crystal under excitation at 200 nm at 5 K is shown. According to the phase diagram of the CuI-CsI system [4], the mixed melts of 60 mol% CsI and 40 mol% CuI form $Cs_3Cu_2I_5$ crystals. In the PL spectrum, there appear two PL bands at 440 and 405 nm, which are quite similar to the 440- and 405-nm PL bands in Cu (10 mol%): CsI (Fig. 1). Futhermore, two PLE spectra detected at 440 (red) and 405 (blue) nm shown in Fig. 2 are likely to correspond to those for the 440- and 405-nm PL bands shown in Fig. 1. These PL and PLE spectra suggest that those PL bands in the two samples have the same origin. The 440-nm PL band is certainly identical to the 440-nm PL band arising from radiative recombination of excitons in $Cs_3Cu_2I_5$, which has been reported by Hirao et al. [5]. Although the origin of the 405-nm PL band is unclear, the PL band perhaps comes from Cu impurities in CsI crystals.

From the above results, we can conclude that the Cu

(10 mol%): CsI crystal contains $Cs_3Cu_2I_5$ microcrystals. Additionally, we notice that the excitation of CsI host crystals in the Cu (10 mol%): CsI crystal gives rise to the photoluminescence originating from the $Cs_3Cu_2I_5$ microcrystals.
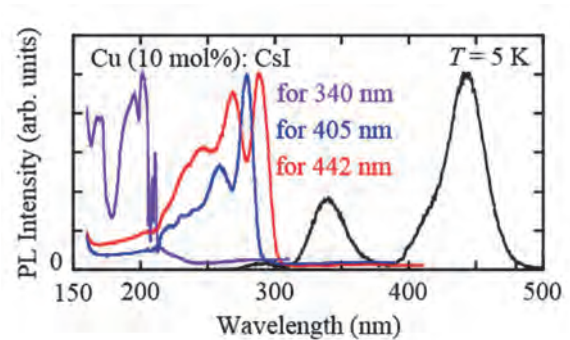

Fig. 1. PL spectrum of a Cu (10 mol%) : CsI crystal under excitation at 200 nm (black), and its PLE spectra detected at 340 (violet), 405 (blue) and 440 (red) nm.
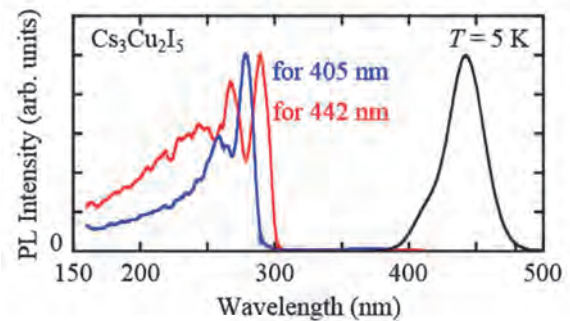

Fig. 2. PL spectrum of $Cs_3Cu_2I_5$ excited at 200 nm (black) , and its PLE spectra detected at 405 (blue) and 440 (red) nm.

[1] K. Shibuya et al., Rev. Sci. Instrum. 78 (2007) 083303.
[2] M. Nakayama et al., Japanese Unexamined Patent Application No. 2003-147343.
[3] H. Nishimura et al., Phys. Rev. B 51 (1995) 2167.
[4] A. Wojakowska et al., J. Chem. Eng. Data 48 (2003) 468.
[5] N. Hirao et al., Meet. Abs. Phys. Soc. Jpn. 58 (2003) 742.

Ⅲ-2

BL3B

Excitation and Emission Spectra of Pr^{3+} in Ga- Doped SrY$_2$O$_4$

M. Yoshino, S. Nishiki and S. Watanabe

Graduate School of Engineering, Nagoya University, Nagoya 464-8603, Japan

The trivalent lanthanide ions (e.g., Ce^{3+}, Nd^{3+}, Er^{3+}) in Oxide crystals have drawn attentions due to their application for luminescent materials in NIR to UV regions such as solid-state lasers or phosphors. The trivalent cerium ion, Pr^{3+}, has also attracted attentions as luminescence centers. In this work, the excitation spectra and emission spectra for Pr^{3+} in Ga-doped SrY$_2$O$_4$ crystal have been measured. For the comparison, the spectra for host oxide, Ga-doped SrY$_2$O$_4$ have been also measured. The Ga-doped SrY$_2$O$_4$ sample and Pr,Ga-doped SrY$_2$O$_4$ sample are produced by solid state reactions. Pr-doped samples are annealed in N$_2$-H$_2$ atmosphere. The concentration of Ga and Pr in the samples are 3 mol% and 1 mol%, respectively. The emission spectrum of Ga-doped SrY$_2$O$_4$ at 200 nm excitation is shown in Fig. 1. The broad peaks from interband optical transition exist around 400 nm. The excitation spectrum monitored at 400 nm emission is shown in Fig. 2. The peak near 200 nm relates the absorption from the optical transition around the band edge in Ga-doped SrY$_2$O$_4$. This corresponds with that in the spectrum monitored at 423 nm in SrY$_2$O$_4$ [1]. The emission spectrum for Pr^{3+} in Ga-doped SrY$_2$O$_4$ is shown in Fig. 3. The spectrum shows sharp peaks originated from Pr^{3+} 4f-4f transition and the broad peaks of interband optical transition from the host are weak while the excitation wavelength is 200 nm. It can be said that excitation energy could transferred from host to Pr^{3+} ion. Figure 4 shows the excitation spectrum monitored 520 nm for Pr^{3+} in Ga-doped SrY$_2$O$_4$. The peaks around 320 nm and 280nm originate in the absorption of the 4f-5d transitions of Pr^{3+}. Then, in the excitation at around 320 nm and 280 nm, Pr^{3+} ions are excited directly, the emission spectrum mainly shows the sharp peaks originated from Pr^{3+} 4f-4f transition as shown in Fig. 3.

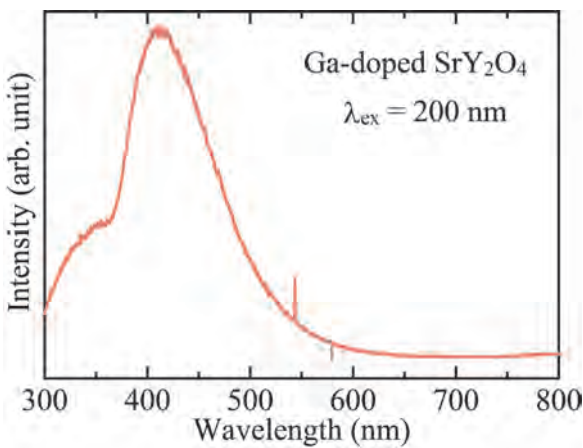[1] M. Yoshino, S. Watanabe and Y. Ichikawa, UVSOR Activity Report **36** (2009) 122.
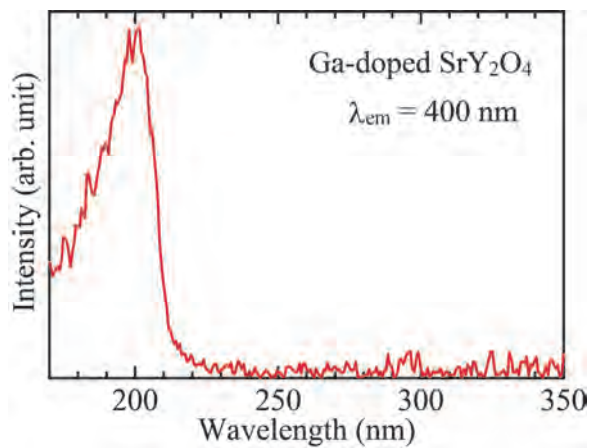
Fig. 1   Emission spectrum of Ga-doped SrY$_2$O$_4$.
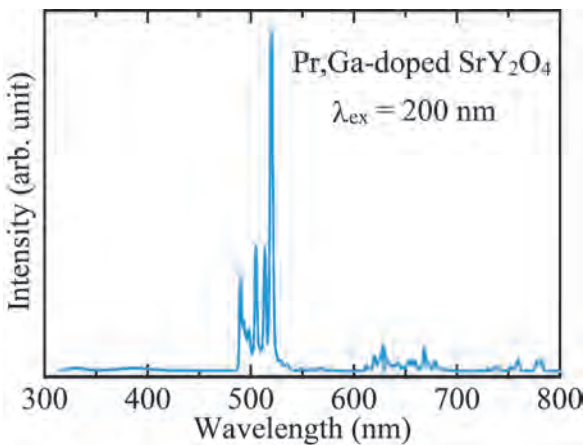

Fig. 2   Excitation spectrum of Ga-doped SrY$_2$O$_4$.
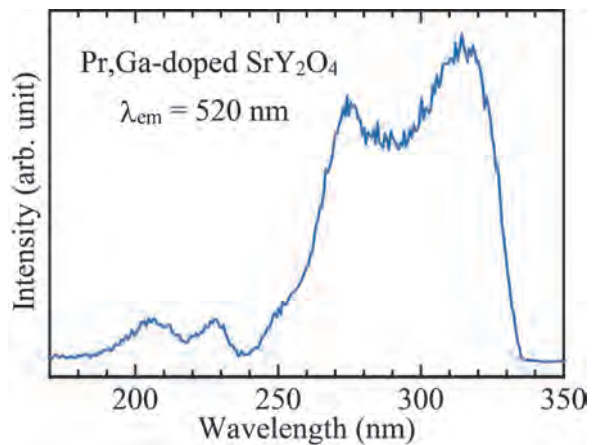

Fig. 3. Emission spectrum of Pr, Ga-doped SrY$_2$O$_4$.

Fig. 4. Excitation spectrum of Pr, Ga-doped SrY$_2$O$_4$.

BL3B

Photoluminescence of TlBr-TlI Mixed Crystals

N. Ohno[1] and K. Matsui[2]

[1]Fundamental Electronics Research Institute, Osaka Electro-Communication University,
Neyagawa 572-8530, Japan
[2]Graduate School of Engineering, Osaka Electro-Communication University,
Neyagawa 572-8530, Japan

Thallous halide crystals are compound semi-conductors attractive for fabrication of γ ray detectors. They exhibit high stopping power originated from high atomic number and high density [1]. TlCl and TlBr crystalize in cubic CsCl-type structure, while the stable form of TlI is orthorhombic structure below 170ºC [2] and is cubic CsCl-type one above it [3,4]. Therefore, it is difficult to grow a large-sized single crystal of TlI under atmospheric conditions. In the present study, mixed singles of TlBr-TlI in cubic CsCl-type structure have been grown and examined to reveal the optical properties such as the optical absorption, photoluminescence and luminescence excitation spectra.

The crystals $TlBr_xI_{1-x}$ were grown by the Bridgeman method after mixing appropriate amounts of purified TlBr and TlI. A plate of the sample cut from as-grown crystals was polished with alumina abrasive plastic film, then etched in hot distilled water. The optical measurements were made at 10 K and at temperatures up to 300 K at BL3B station.

Figure 1 shows and absorption spectra (black curves) of $TlBr_xI_{1-x}$ mixed crystals for different compositions measured at 10 K. In pure TlBr (x=1.0), the fundamental absorption edge is of the indirect-forbidden exciton transition [5]. As clearly seen in Fig.1, the indirect absorption edge moves to lower energy with increasing iodine concentration. At x=0.4, the absorption-edge energy is located at around 2.0 eV. Below x≤0.3, the absorption spectra showed no clear absorption edge which was ascribed to the phase transition in $TlBr_xI_{1-x}$ mixed crystals. In I-rich mixed crystal, the cubic phase becomes unstable below the room temperature.

On exciting $TlBr_xI_{1-x}$ mixed crystals with light at the energy above the indirect absorption edge, a Stokes-shifted broad luminescence band is observed as clearly seen in Fig. 1 (blue curves). In TlBr (x=1.0), the shape of the spectra is almost Gaussian as previously observed in lightly I-doped TlBr [6]. The broad band was identified to be originated from annihilation of excitons self-trapped at an iodine ion due to the impurity-induced self-trapping. It is worth noting in Fig. 1 that the amount of the Stokes shift and the full width at the half maximum of the observed luminescence band become continuously smaller as the iodine concentration is increased. Therefore, with increasing I-ion concentration in $TlBr_xI_{1-x}$ mixed crystals, the lattice relaxation of the

self-tapped excitons decreases due to the smaller exciton-phone interaction, resulting in decreasing of Stokes shift of the luminescence band width.
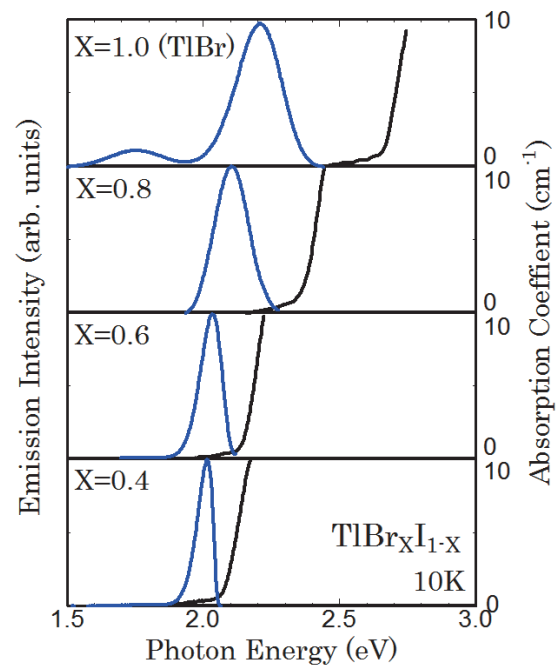

Fig. 1. Photoluminescence (blue) and absorption coefficient (black) spectra of $TlBr_xI_{1-x}$ at 10 K.

[1] K. Hitomi, T. Shoji and K. Ishii, J. Crystal Growwth **379** (2013) 93.
[2] N. Ohno and M. Itoh, J. Phys. Soc. Jpn. **62** (1993) 2966.
[3] K. Heidrich, W. Staude, J. Treusch and H. Overhof, Solid State Commun. **16** (1975) 1043.
[4] A. Fujii and I. Ishikawa, J. Phys. Soc. Jpn. **56** (1987) 4581.
[5] J. Nakahara, K. Kobayashi and A. Fujii, J. Phys. Soc. Jpn. **37** (1974) 1312.
[6] J. Nakahara and K. Kobayashi, J. Phys. Soc. Jpn. **40** (1976) 180.

BL3B

VUV Absorption Spectra of Racemic Alanine Crystals

S. Tanaka, M. Kitaura and A. Ohnishi

Department of Physics, Faculty of Science, Yamagata University, Yamagata 990-8560, Japan

Amino acids are simple chiral molecules with L- and D-forms. Protein molecules are composed of only L-amino acids. This is called "homochirality", which has attracted much attention in relation to the mystery of life. It has been generally accepted that the homochirarity of proteins comes from the creation of L-amino acids by circularly polarized VUV light in outer space region. So far, VUV absorption spectra of amino acids have been studied using aqueous solutions [2] and thin films [3]. To our knowledge, there is no report on VUV absorption spectra of amino acid crystals. We have measured VUV reflectivity spectra of L-alanine single crystals to obtain the spectra of various optical constants. In the present study, we have measured reflectivity spectra of racemic alanine crystals, and investigated the change of VUV absorption spectra on crystal structure, which gives us information on intermolecular interaction among alanine molecules.

Racemic alanine single crystals were obtained from saturated aqueous solution of commercial alanine powder. The crystals are of needle shape. The crystal axes were distinguished by two polarizers arranged in a cross Nicole alignment. To obtain VUV absorption spectra, we performed the Kramers-Kronig (K-K) analysis of reflectivity spectra. In the K-K analysis, it is necessary to determine absolute reflectivity over the energy range as wide as possible. We obtained absolute reflectivity by the correction using refractive indexes in the transparent region below 2 eV.

Figure 1 shows VUV absorption spectra of a racemic alanine crystal for different configurations of linearly polarized light. A few peaks appear below 15 eV. No remarkable peak is found above 15 eV. This feature is similar to VUV absorption spectra of L-alanine crystals [4]. On the other hand, there is a linear dichroism between them. Figure 2 shows VUV absorption spectra extended in the 5-12 eV range. Absorption peaks for a racemic alanine crystal are apparently broader than those for L-alanine crystals [4]. The reason for such broadening of absorption peaks is not clear. To clarify it, theoretical approaches based on electronic state calculations are effective. Theoretical calculations were applied for alanine molecules [5,6]. However, there is no instance applied for alanine bulk crystals. Therefore, theoretical calculations for alanine bulk crystals are desired.
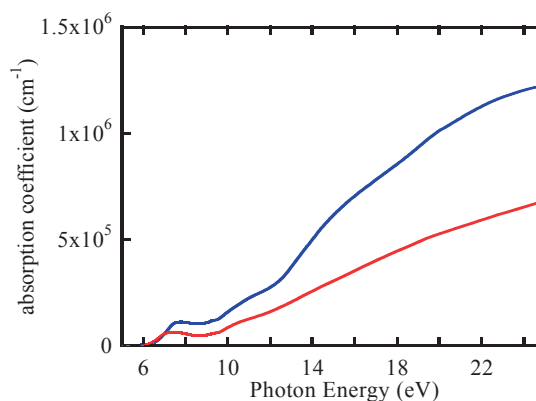

Fig. 1. VUV absorption spectra of a racemic alanine crystal, derived from the Kramers-Kronig analysis of reflectivity spectra in 5-25 eV range. The data were measrued at room temperature.
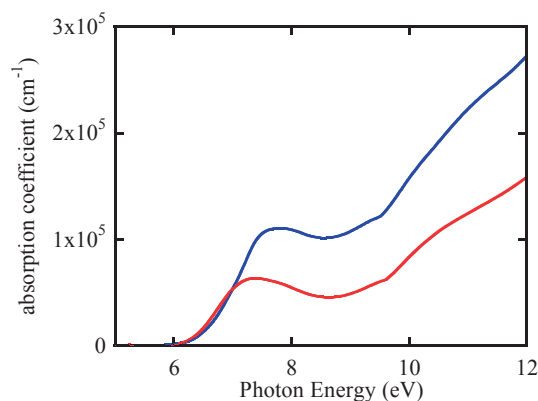

Fig. 2. VUV absorption spectra of a racemic alanine crystal, extended in the 5-12 eV range.

[1] P. A. Snyder *et al*., Biopolymers **12** (1973) 975.
[2] T. Inagaki *et al*., Biopolymers **12** (1973) 1353.
[3] M. Tanaka *et al*., J. Electron Spectrosc. Relat. Phenom. **181** (2001) 177.
[4] S. Tanaka *et al.,* UVSOR ACTIVITY REPORT **42** (2015) 70.
[5] F. Kaneko *et al*., J. Phys. Soc. Jpn. **78** (2009) 013001.
[6] T. Kaneko *et al*., CHIRALITY **23** (2011) E52.

BL3B

Construction of Vacuum Referred Binding Energy Diagram in Gd$_3$(Al,Ga)$_5$O$_{12}$:Ce^{3+} Phosphors

K. Asami[1], J. Ueda[1], M. Kitaura[2] and S. Tanabe[1]

[1] Graduated School of Human and Environmental Studies, Kyoto University,
Kyoto 606-8501, Japan
[2] Department of Physics, Faculty of Science, Yamagata University,
Yamagata 990-8560, Japan

Ce^{3+}- doped Gd$_3$Al$_{5-x}$Ga$_x$O$_{12}$ (GAG*G*) is a promising optical material for the scintillator [1]. It is known that the quantum efficiency (QE) of GAG*G*: Ce^{3+} becomes lower with increasing Ga content, *x* [2]. To understand optical properties of a phosphor, an electronic structure of host material should be investigated. Dorenbos suggested the construction method of the vacuum referred binding energy (VRBE) diagram [3]. This diagram can be constructed from the spectroscopy data of host exciton energy and charge transfer transition (CTS) of Eu^{3+}. To determine those transition energies, we measured photoluminescence excitation (PLE) spectra of both Ce^{3+}- and Eu^{3+}- doped GAG*G* at UVSOR BL3B.

Figure 1 (a) shows the PLE spectra of Ce^{3+}- doped GAG*G* phosphors with various Ga content. In PLE spectra, the host exciton peaks are observed at around 200 nm and three bands derived from Ce^{3+} are observed at 220 nm (4f-5d$_{3, 4, 5}$), 350 nm (4f-5d$_2$) and 450 nm (4f-5d$_1$). Several peaks at 270 nm and 310 nm are due to the intra – 4f transitions of Gd^{3+} in the host [1]. From the host exciton peaks, the bandgap energies of GAG*G* (x = 1, 2, 3 and 4) are estimated to be 6.84, 6.81, 6.63 and 6.55 eV, respectively. With increasing Ga content, the bandgap becomes narrower. Figure 1 (b) shows the PLE spectra of Eu^{3+}: GAG*G* phosphors. The strong broad band is located at around 250 nm, which is attributed to CTS of O^{2-}-Eu^{3+}→O$^-$-Eu^{2+}. With increasing Ga content, the peak wavelength of CTS shifts to longer. The top of valence band is calculated by subtracting the CTS energy from the determined 4f state energy of Eu^{2+}.

Based on the method of VRBE diagram construction by Dorenbos [3], the VRBE diagram of Ce^{3+}-doped GAG*G* are constructed by using measurement data obtained in Fig.2 . The energy E_v which is top of valence band shifts higher with increasing Ga content while the energy E_c which is the bottom of conduction band slightly changes. When the energy of Ce^{3+}:5d$_1$ is close to E_c, the excited electrons located at Ce^{3+}:5d$_1$ state tend to move to the conduction band by thermal ionization. From this diagram, with increasing Ga content, the energy gap between E_c and Ce^{3+}:5d$_1$ becomes smaller. Therefore QE of Ce^{3+} in GAG*G* system becomes decrease by thermal ionization quenching.
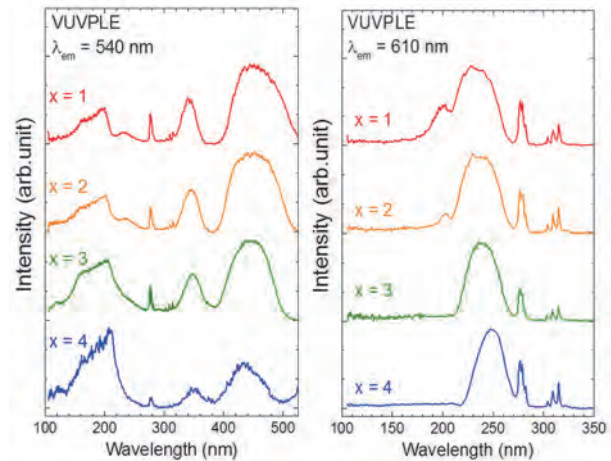

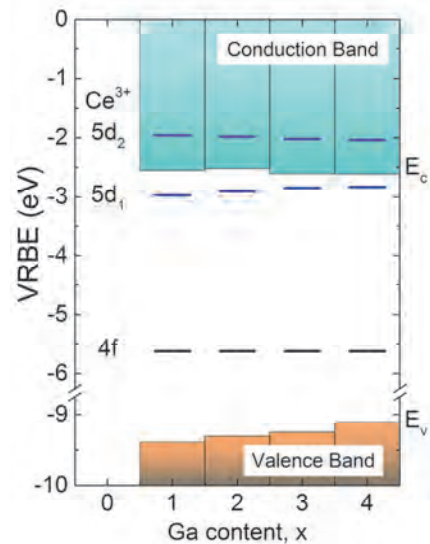Fig. 1. PLE spectra of (a). Ce^{3+}-doped GAG*G* (Left) and (b). Eu^{3+}-doped GAG*G* (Right).

Fig. 2. Constructed VRBE diagram of Ce^{3+}:GAG*G*.

[1] M. Kitaura, A. Sato, K. Kamada, A. Ohnishi and M. Sasaki, J. Appl. Phys. **115** (2014) 083517.
[2] J. M. Ogiegło, A. Katelnikovas, A. Zych, T. Jüstel, A. Meijerink and C. R. Ronda, J. Phys. Chem. A **117** (2013) 2479.
[3] P. Dorenbos, J. Lumin. **134** (2013) 310.

BL3B, BL6B

Local Structure of Gd³⁺ and Ce³⁺ Ions in $Gd_3Al_{5(1-x)}Ga_{5x}O_{12}$ Crystals Studied by UV and IR Absorption Spectroscopy

C. Oyama[1], M. Kitaura[1], M. Ishizaki[1], K. Kamada[2], S. Kurosawa[2], A. Ohnishi[1] and K. Hara[3]

[1]*Faculty of Science, Yamagata University, Yamagata 990-8560, Japan*
[2]*NICHe, Tohoku University, Sendai 980-0845, Japan*
[3]*RIE, Shizuoka University, Hamamatsu 432-8011, Japan*

The Ce:$Gd_3Al_2Ga_3O_{12}$ (Ce:GAGG) garnet crystals has been known as an inorganic scintillators with high light output, high energy resolution, and no hygroscopic nature [1]. The scintillation properties strongly depend, especially on the composition ratio of Al^{3+} and Ga^{3+} ions. The control of the composition ratio of Ga^{3+} and Al^{3+} ions is of great importance to bring out the high performance of Ce:GAGG. The crystals of garnet type have three cation sites named A, B, and C, in which cations are coordinated by eight, six, and four oxygen ions, respectively. The chemical formula of oxide garnets is expressed as $A_3B_2C_3O_{12}$. Al^{3+} and Ga^{3+} ions can regularly occupy octahedral (B) and tetrahedral (C) sites. So far, the distribution of Al^{3+} and Ga^{3+} ions has been investigated in garnet solid solutions. Although there are a number of reports on this subject, it still remains obscure which sites Ga^{3+} ions occupy preferentially [2,3]. From the viewpoint of basic science and industrial application, it is worthwhile to investigate the site preference of Ga^{3+} ions in Ce:$Gd_3Al_{5(1-x)}Ga_{5x}O_{12}$ crystals. In the present study, Gd^{3+} and Ce^{3+} 4f-4f absorption spectra of undoped and cerium-doped $Gd_3Al_{5(1-x)}Ga_{5x}O_{12}$ ($0.4 \leq x \leq 1$) crystals have been measured at low temperatures below 10 K in ultraviolet and infrared ranges [4]. Generally, the 4f-4f transitions of rare- earth ions give rise to narrow absorption peaks, and they are expected to be sensitive to cation distribution. Thus, Gd^{3+} and Ce^{3+} 4f-4f absorption peaks can utilize as a probe to clarify the site preference of Ga^{3+} ions.

Figure 1 shows absorption spectra of undoped $Gd_3Al_{5(1-x)}Ga_{5x}O_{12}$ (a) and cerium-doped $Gd_3Al_{5(1-x)}Ga_{5x}O_{12}$ (b), which are due to 4f-4f transitions of Gd^{3+} and Ce^{3+} ions, respectively. In Fig. 1(a), the peak positions and spectral widths of absorption peaks for $x = 0.4$ were almost the same as those for $x = 1.0$. This result suggests that, for $x = 0.4$, Ga^{3+} and Al^{3+} ions occupy octahedral and tetrahedral sites, respectively. This opinion is consistent with that by Ogiegro *et al*. [2], but is inconsistent with that by Kanai *et al*. [3] The peak positions for $x = 0.6$ and 0.8 are shifted to lower energy side. The spectral widths were clearly broader, compared to that for $x = 0.4$ and 1.0. The peak shift and spectral broadening indicate that, for $x = 0.6$ and 0.8, Ga^{3+} and Al^{3+} ions occupy both of octahedral and tetrahedral sites. In Fig. 1(b), the position of the absorption peak shifts to lower wavenumber side with increasing x. This is explained by the reduction of crystal field strength at Ce^{3+} ions, which is due to the

replacement of Ga^{3+} ions for Al^{3+} ions [5]. The spectral width for $x = 0.4$ is largest of all x, suggesting the variety of crystal field at Ce^{3+} ion sites. In oxide garnets, oxygen vacancies and antisite ions are known as primary imperfections [6]. It is thus likely that various Ce^{3+} ions coupled with such imperfections are formed. The present study reveals that the variety of Ce^{3+} ions coupled with imperfections is the largest for $x = 0.4$. The reason for this is unclear, so that it is an open subject to be solved in near future.
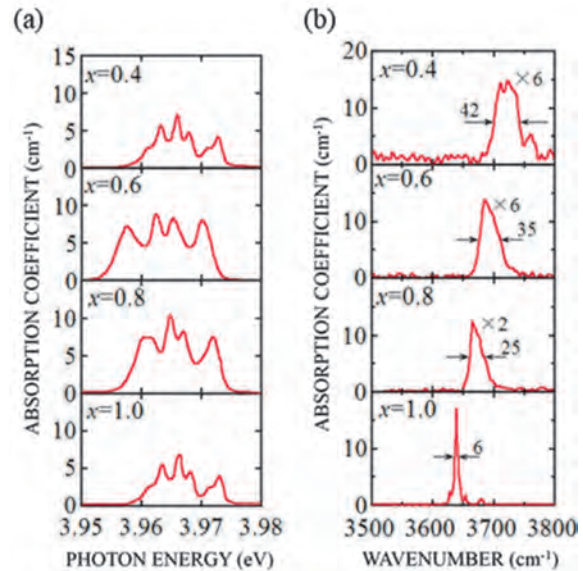

Fig. 1. Absorption spectra due to 4f-4f transitions of Gd^{3+} ions in undoped $Gd_3Al_{5(1-x)}Ga_{5x}O_{12}$ (a) and Ce^{3+} ions in cerium-doped $Gd_3Al_{5(1-x)}Ga_{5x}O_{12}$ (b). These data were observed below 10 K.

[1] K. Kamada *et al*., J. Cryst. Growth **352** (2012) 88.
[2] J. M. Ogiegro *et al*., J. Phys. Chem. C **35** (2013) 322.
[3] T. Kanai *et al*., J. Am. Ceram. Soc. **462** (2008) 456.
[4] For $x = 0$ and 0.2, it is not possible to obtain single crystals of garnet phase.
[5] P. Dorenbos, J. Lumi. **151** (2014) 224.
[6] M. Kitaura *et al*., J. Appl. Phys. **115** (2014) 083517.

BL4U

Observation of Morphology of a Fuel Cell by Using a Humidity Control Sample Cell for STXM

T. Ohigashi[1, 2], Y. Inagaki[1], T. Horigome[1] and N. Kosugi[1, 2]

[1] UVSOR Synchrotron, Institute for Molecular Science, Okazaki 444-8585, Japan
[2]School of Physical Sciences, The Graduate University for Advanced Studies (SOKENDAI), Okazaki 444-8585, Japan

One of the advantages of a scanning transmission X-ray microscopy (STXM) is tolerance for ambient conditions of samples. Due to high transmittance of the X-ray, the STXM does not require a vacuum condition but enables to observe electronic states of various samples in atmospheric pressure or in water. Moreover, a focusing optical element of the STXM, namely, a Fresnel zone plate, has characteristics such as long working distance and long focal depth. These features enable to perform *in-situ* observation, which is impossible for an electron microscopy; therefore, various sample cells have been developed widely [1]. Control of humid atmosphere around the sample is sometimes needed as a promising *in-situ* observation method [2]; for example, a fuel cell working under high humid atmosphere and high temperature. In this study, we have developed a humidity control sample cell and performed a test measurement.

The present humid control sample cell (shown in Fig. 1) is a small chamber consisted of two silicon nitride membranes (thickness of 100 nm) as windows [3]. A small sensor to measure humidity and temperature (SHT7x, Sensirion AG) is set inside of the chamber. The cell has three ports for inlet/outlet of gas flowing and two of them were used in this study. The inlet and outlet were connected to a feedthrough of the STXM chamber with stainless tubes and dry/humid helium gas is flowed into the cell to control the humidity. Humidity in the gas is added by bubbling pure water in a bottle and its flow rate is controlled by using a needle valve manually. The inside of the STXM chamber was transferred by helium gas until air pressure. As a performance test, we could change the humidity from 16.1 to 80.4% at 29°C (temperature inside of the STXM chamber was higher than RT).

By using the cell, morphological change of thin sections of a fuel cell fixed on Formvar membrane was used as a test sample. 2-dimensional distributions of fluorine in the polymer were obtained by using the K-absorption edge of fluorine (687 eV). X-ray transmission images below and above of the edge (682 and 692 eV) were obtained. After conversion to optical density images, the distribution of fluorine was obtained by subtracting these images. The distribution of fluorine of the humidity at 16% and 8% are shown in Fig. 2. In these images, bright areas show high concentration of fluorine and dark areas like cracks are seen on the center. By changing the humidity from 16% to 80%, 11% of the dark area decreased. This change of the area was caused by swelling of water vapor of the polymer.

As a future plan, temperature control and auto-control (i.e. feedback of the humidity and temperature) system are under consideration. As further application of this humid cell, observation of living biological samples, such as cells and bacteria, will be performed.
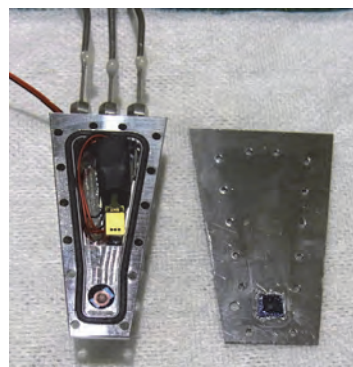

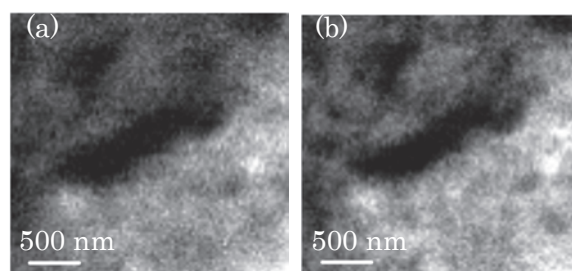Fig. 1. The inside and the base plate of the humidity control sample cell.

Fig. 2. Distribution of fluorine in the fuel cell (bright pixels show high concentration). The humidity of the cell were at (a) 16% and (b) 80%.

[1] X. H. Zhu *et al.*, UVSOR Activity Report **41** (2014) 72.
[2] V. Berejnov *et al.*, ECS Transactions **41** (2011) 395-402.
[3] T. Ohigashi *et al.*, accepted.

Influence of the Oxygen Vacancy at Ta/TaO$_x$ Interface on Resistive Switching Memories

Y. F. Wang[1], W. F. Pong[1], J. S. Chen[2], J. W. Chiou[3], T. Ohigashi[4] and N. Kosugi[4]

[1]Department of Physics, Tamkang University, Tamsui 251, Taiwan
[2]Department of Materials Science and Engineering, National Cheng Kung University, Tainan 701, Taiwan
[3]Department of Applied Physics, National University of Kaohsiung, Kaohsiung 811, Taiwan
[4]UVSOR Synchrotron, Institute for Molecular Science, Okazaki 444-8585, Japan

Ⅲ-2

In this work, we have studied the electronic structure and the location of oxygen vacancy in the interface of the Ta/TaO$_x$/Pt thin film and identify the type of conducting path by scanning transmission x-ray microscopy (STXM). The amorphous TaO$_x$ thin film of thickness of ~150 nm was deposited by electron beam evaporation on Pt/SiO$_2$/Si substrates. Active electrodes of Ta were thermally evaporated respectively on the TaO$_x$ thin film with an equivalent thickness of ~150 nm. As shown in Fig. 1, the STXM stack mapping displays the cross-sectional views of the Ta/TaO$_x$/Pt thin film. Obviously, due to a uniform diffusion occurs in the vicinity of the Ta/TaO$_2$ interface, the image of the Ta/TaO$_x$/Pt thin film revealed that the interfacial TaO$_x$ was ~180 nm in thickness. The experiments were performed at the 4U beamline. Figure 2 presents the corresponding O K-edge x-ray absorption near-edge structure (XANES) spectra of the Ta/TaO$_x$/Pt thin film. The O K-edge STXM-XANES spectra were recorded at three selected regions, *cyan*, *red* and *yellow*, in the Ta/TaO$_x$/Pt thin film, respectively. According to the dipole-transition selection rule, the features at ~530-545 eV are attributed to the electron excitations from O 1s-derived states to 2p-derived states, which are approximately proportional to the density of the unoccupied O 2p-derived states.[1] The intensities of the O K-edge STXM-XANES spectra of the *red* region are significantly higher than that of the *cyan* region, which reflects the increase in the number of unoccupied O 2p-derived states. In other words, the STXM-XANES results demonstrate that the population of defects at the O sites in the Ta/TaO$_x$ interface and confirming the enhanced density of states of O 2p-derived states, as the population of defects and dangling bonds at/above E_{CBM} or E_F in the Ta/TaO$_x$ interface. The STXM-XANES results intensely support the phenomena that the occurrence of O 2p vacancy at Ta/TaO$_x$ interface affects the resistive switching effect of the Ta/TaO$_x$/Pt thin film.
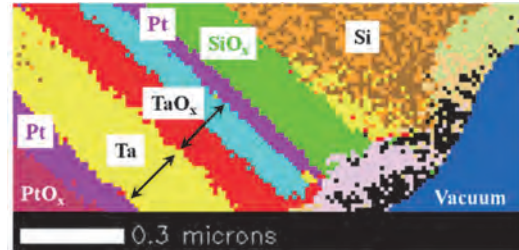

Fig. 1. The STXM stack mapping of the cross-sectional views of the Ta/TaO$_x$/Pt thin film.
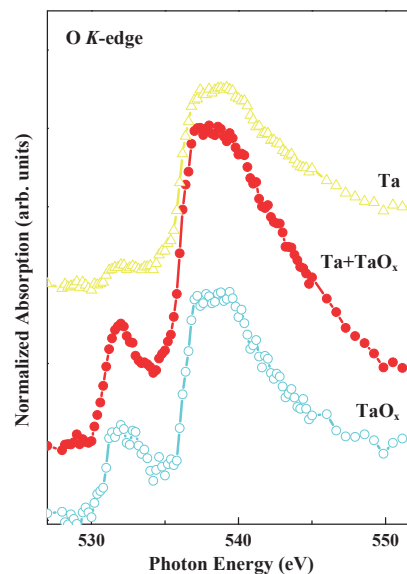

Fig. 2. The corresponding O K-edge STXM-XANES spectra were recorded at three selected regions, *cyan*, *red* and *yellow*, in the Ta/TaO$_x$/Pt thin film, respectively.

[1] J. W. Chiou *et al*., Appl. Phys. Lett. **81** (2002) 3389.

BL4U

Resolving the Electronic Structure of TiO$_2$ Core-Shell Nanostructures Using Scanning Transmission X-Ray Microscope

Y. F. Wang[1], S. H. Hsieh[1], J. W. Chiou[2], W. F. Pong[1], T. Ohigashi[3] and N. Kosugi[3]

[1]*Department of Physics, Tamkang University, Tamsui 251, Taiwan*
[2]*Department of Applied Physics, National University of Kaohsiung, Kaohsiung 811, Taiwan*
[3]*UVSOR Synchrotron, Institute for Molecular Science, Okazaki 444-8585, Japan*

In this work, a three-dimensional (3D) hierarchical TiO$_2$ is successfully constructed using scanning transmission x-ray microscopy (STXM). The core portion of the sample contains rutile TiO$_2$ nanowire (NW) while the rutile nanoparticles (RNP) and anatase TiO$_2$ are sequentially located on the shell region. The TiO$_2$ NW array provides a fast electron transport pathway due to its quasi-single-crystalline structure and the 3D configuration with NPs in the shell portion provides a large surface area for more efficient photo-charge separation without significantly sacrificing the electron collection efficiency [1] which attracted our interest to probe this nano-scale interface phenomenon.

Figure 1 shows the (a) scanning electron microscope (SEM) and (b) STXM images of focused ion beam (FIB) milled ANP/RNP/NW sample (above the red dashed line) on fluorine doped tin oxide (FTO) substrate (below the red dashed line). The STXM image was recorded at 460 eV. Fig. 2(a) shows the magnified STXM image in middle of sample of Fig. 1 (b), where Ti L$_{2,3}$-edge x-ray absorption near edge spectra (XANES) had been measured and analyzed by principle component analysis (PCA) method. Fig. 2(b) was generated by PCA method analyzed in the same area shown in Fig. 2(a) and indicates similar spectra with the same color which defines the spatial distribution of background (blue), Pt (yellow), carbon film (purple) and surface (red), semi-surface (green), shell (brown), semi-core (orange), core (cyan) regions of ANP/RNP/NW.

Figure 2(c) depicts the Ti L$_{2,3}$-edge XANES of different regions of ANP/RNP/NW. Line shapes of e$_g$-states in L$_3$-edge around 458 eV show the anatase phase TiO$_2$ in the surface (red) and semi-surface (green) regions [2], the rutile phase TiO$_2$ in core (cyan) region and mixed spectra of anatase and rutile phases in shell (brown) and semi-core (orange) regions. These results reveal that even the size of ANP is smaller than the spatial resolution of STXM [3], the spatial distribution of different phases of TiO$_2$ core-shell structures can still be successfully resolved under STXM after FIB milling.
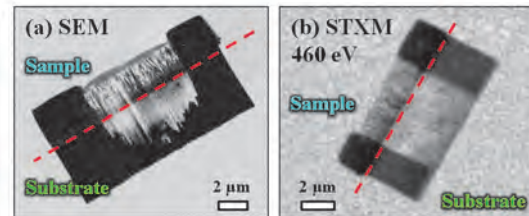

Fig. 1. (a) SEM image of ANP/RNP/NW on FTO. (b) STXM image of ANP/RNP/NW on FTO measured at 460 eV.
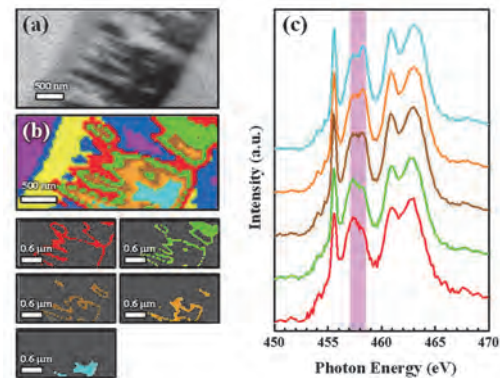

Fig. 2. (a) Magnified STXM image of ANP/RNP/NW. (b) Spatial distribution of background (blue), Pt (yellow), carbon film (purple) and surface (red), semi-surface (green), shell (brown), semi-core (orange), core (cyan) regions of ANP/RNP/NW. (c) Corresponding Ti L$_{2,3}$-edge XANES of different regions of ANP/RNP/NW.

[1] J. Y. Shin *et al*., Adv. Funct. Mater. **21** (2011) 3464.
[2] J. S. Yang, Appl. Mater. Interfaces **5** (2013) 7425.
[3] G. S. Henderson *et al*., Phys. Chem. Minerals **29** (2002) 32.

BL4U

Effect of Fe$_2$O$_3$ Coating on ZnO Nanorod Probed by Scanning Transmission X-Ray Microscopy

Y. X. Chen[1], Y. F. Wang[1], J. W. Chiou[2], C. L. Dong[1], W. F. Pong[1], T. Ohigashi[3] and N. Kosugi[3]

[1]*Department of Physics, Tamkang University, Tamsui 251, Taiwan*
[2]*Department of Applied Physics, National University of Kaohsiung, Kaohsiung 811, Taiwan*
[3]*UVSOR Synchrotron, Institute for Molecular Science, Okazaki 444-8585, Japan*

Ⅲ-2

A novel Fe$_2$O$_3$/ZnO core-shell nanorods for photoelectrochemical (PEC) water splitting is developed recently [1]. The PEC performances, such as photocurrent response and incident photons to electrons (IPCE), vary with the thickness of Fe$_2$O$_3$ coating layer. However, the mechanism of the improved PEC activity remains unclear. In this work, pristine and Fe$_2$O$_3$ coated-ZnO core-shell nanorods have been investigated by using x-ray spectroscopic coupled with microscopic approaches (i.e., x-ray absorption near-edge structure (XANES) and scanning transmission X-ray microscopy (STXM)).

Figures 1(a)-(d) present the O K-edge STXM images and its stack mappings of selected single nanorod of Fe$_2$O$_3$/ZnO and pristine ZnO. The stack mappings display blue, yellow, red and green areas, corresponding to the different regions that are associated with different thickness and chemical properties of the nanorods. Figures 1 (e)-(h) show the XANES spectra, which correspond to Figs. 1 (a)-(d). The different colored spectra reflect the various region of the nanorods. The O K-edge probes the electron transitions from O 1s core level to the O 2p-Zn 3d/4sp hybridized states. The area under the spectrum reflect the amount of density of unoccupied O 2p-derived states. Thus, based on the spectroscopic results, the electronic structures of the layer region and the core area differ in both samples. Besides, strong anisotropic effects are observed for both samples based on polarized-XANES. Notably, the density of states in the surface of the coated- and pristine nanorods are different and the results suggest that the oxygen-related deficiency is formed in the core-shell nanorods which can affect the photocatalytic activity.

The enhanced PEC performance of Fe$_2$O$_3$ coated ZnO compared with pristine ZnO is likely to be owing to the presence of interface that causes varied electron density of states in the core-shell structured nanorods.
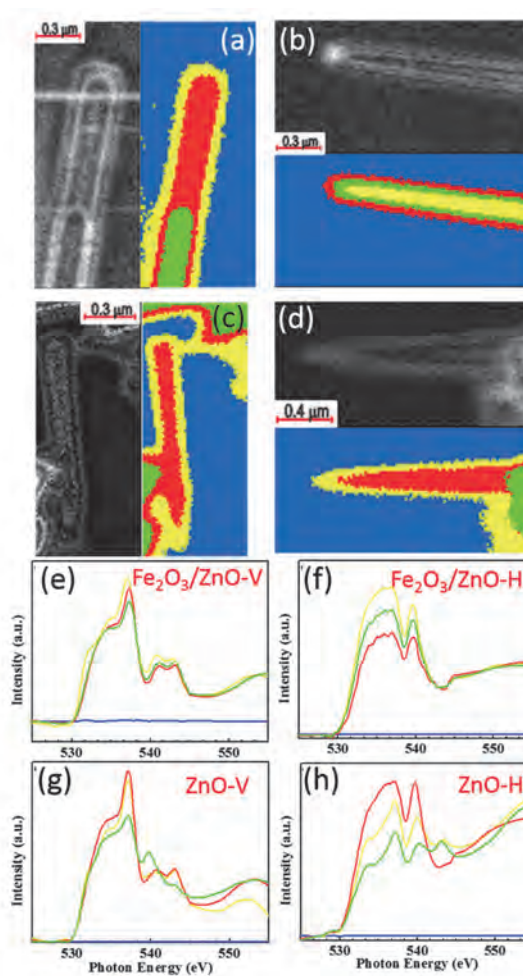

Fig. 1. Upper panel: Polarized O K-edge scanning transmission X-ray microscopy image and its corresponding stack mappings of selected single Fe$_2$O$_3$ coated- ((a)and (b)) and pristine ZnO nanorods ((c) and (d)). Lower panel: Polarized O K-edge STXM-XANES spectra of Fe$_2$O$_3$ coated- ((e) and (g)) and pristine ZnO nanorods ((f) and (h)). The color corresponds to the different region of the nanorods.

[1] Y. K. Hsu *et al.*, ACS Appl. Interfaces **7** (2015) 14157.

BL4U

Mapping Oxygen Activation on Different Surface Facet of Palladium Nanocrystals for Organic Catalysis

M. W. Lin[1], Y. L. Lai[1], M. H. Cao[2], T. Ohigashi[3], N. Kosugi[3], Q. Zhang[2] and Y. J. Hsu[1*]

[1]National Synchrotron Radiation Research Center, Hsinchu 300, Taiwan
[2] Institute of Functional Nano- & Soft Materials (FUNSOM) Soochow University, 215123, P. R. China
[3]Institute for Molecular Science, Okazaki 444-8585, Japan
Electronic mail: yjhsu@nsrrc.org.tw

The O_2 activation process where inert ground triplet O_2 is excited to produce highly reactive singlet O_2 involves a key step in many organic oxidation and cancer treatment. However, it puzzles scientist what factor induces the change of electron spin state of O_2 molecules, although it has demonstrated that the presence of noble metal nanoparticles can promote the generation of singlet O_2. In previous works, Q. Zhang *et al.,* first demonstrated that surface facet of metal nanocrystals is a key parameter for tuning the activities of generating singlet oxygen. The experiments and simulations elucidated that a spontaneous spin−flip process may occur during the molecular absorption when appropriate surface facets are selected. On a selected surface facet, the charge state of the Pd surface is a critical parameter to activate O_2 to generate a species that behaves like singlet O_2 both chemically and physically [1]. Based on this finding, we prepared a metal–semiconductor hybrid system in which the nanocrystals of Pd{100} facets are supported on TiO_2 surface. Through illumination of appropriate light, the electrons are anticipated be transferred from TiO_2 to metallic Pd catalysts and thus enhance the oxygen activation.

To confirm the charge transfer at the heterojunction between TiO_2 and Pd heterojunction, chemical maps of oxygen distributions within microaggregates of SiN/TiO_2-Pd were studied by scanning transmission X-ray microscopy (STXM). The TiO_2-Pd hybrid structures were obtained according to following procedures. The Pd nanocubes with 20 mg TiO_2-P25 were synthesized according to a previously described protocol [2]. In a typical synthesis, 8.0 mL of an aqueous solution containing poly(vinyl pyrrolidone) (PVP, MW = 55 000, Sigma– Aldrich, 856568-100g; 105 mg), l-ascorbic acid (AA, Sigma–Aldrich, A0278-25g; 60 mg), and KBr (300 mg) was heated in a 50 mL three- necked flask for 10 min at 80 ºC with magnetic stirring. Subsequently, 3.0 mL of an aqueous solution of potassium palladium(II) chloride ([K2PdCl4], Aladdin, 1098844-1g ; 63 mg) was added with a pipette, and the reaction mixture was stirred at 80 ºC for 3 h. The powders were collected by centrifugation and washed with deionized water to remove excess PVP. The final product was dissolved into the deionized water and then dipped onto the SiN substrate.

Figure 1 displays the STXM images of (a) SiN/TiO_2-Pd (cubes {100} facets) and (b) SiN/TiO_2-Pd (octahedrons {111} facets), which are optical density

(OD) maps obtained at 530.9 eV, the major characteristic absorption peaks of TiO_2. The bright region represents elemental distributions of O in TiO_2. The corresponding micro NEXAFS spectra extracted from different color circles as shown in Figs. 1(a) and (b) are displayed in Figs. 2(a) and 2(b), respectively. The resonance at 530.9 eV for both surface facet is assigned to $1\sigma u \rightarrow 1\pi g*$ transition for TiO_2 contacted with Pd surface. Noticeably, the absorption peak at higher photon energy for TiO_2-Pd{100} (at 533.3 eV) shifts to lower photon energy in comparison with TiO_2-Pd{111} (at 533.6 eV), indicating that significant electrons are transferred from TiO_2 to the Pd{100} surface. The preliminary results indicate that the chemical mapping of oxygen activation on different surface facet of Pd nanocrystals will shed light on designing high efficient noble metal nanocatalysts for organic oxidation and cancer treatments.
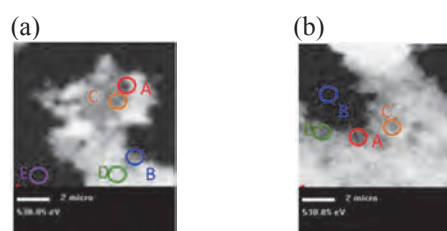

Fig. 1. The OD images of (a) SiN/TiO_2-Pd (cubes {100} facets) and (b) SiN/TiO_2-Pd (octahedrons {111} facets) obtained at 530.9 eV.
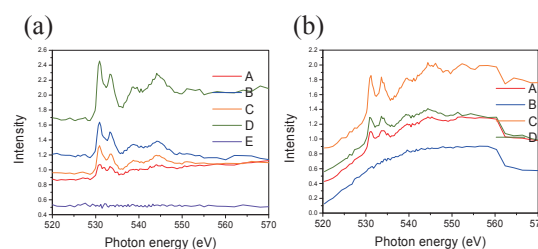

Fig. 2. Micro-NEXAFS spectra of the O *K*-edge extracted from the Figs. 1(a), and 1(b), respectively.

[1] L. Ran, M. Keke, Y. Xiaodong, Y. Wensheng, H. Yaobing, W. Jianyong, F. Yao, W. Xisheng, W. Xiaojun, X. Yi and X. Yujie, J. Am. Chem. Soc. **135** (2013) 3200.
[2] B. Li, R. Long, X. Zhong, Y. Bai, Z. Zhu, X. Zhang, M. Zhi, J. He, C. Wang, Z.-Y. Li and Y. Xiong, Small **8** (2012) 1710.

BL4B

Valence State Analysis of Mn Ions Doped in CaTiO$_3$

T. Murai[1], K. Mori[1], D. Yamada[1], H. Murata[2] and T. Yamamoto[1,3]

[1]Faculty of Science and Engineering, Waseda University, Tokyo 169-8555, Japan
[2]Association of International Arts and Science Institute of Natural Science, Yokohama City University, Yokohama 236-0027, Japan
[3]Institute of Condensed-Matter Science, Waseda University, Tokyo 169-8555, Japan

Multiferroic materials, which have both ferroelectric and ferromagnetic properties, have been extensively studied for their potential applications in industry. It was reported that the ABO$_3$ type oxides, e.g., BiFeO$_3$ and YMnO$_3$, show multiferroic properties, and, on the other hand, dilute doping of the magnetic element into the ferroelectric material gives ferromagnetic property, which means such materials also have a multiferroic property. One of the examples of the later ones is Fe doped Bi$_4$Ti$_3$O$_{12}$ [1]. To understand the mechanism of newly appeared ferromagnetism by dilute doping of magnetic element in such ferroelectric materials, it is mandatory to know the local environment of doped ions. However, it is not so easy to determine the local environment of such dilute dopants that one often skips such important analysis. In the case of the valence state analysis of 3d transition metals, analysis with L$_{2,3}$-edge X-ray absorption spectrum (XAS) is quite powerful. We could successfully determine local environment of Mn and Fe ions doped in Bi$_4$Ti$_3$O$_{12}$ by such XAS analysis [2, 3]. In the current study, valence state of Mn ions in Mn-doped CaTiO$_3$ is investigated by the Mn-L$_3$ XAS measurements.

Samples were prepared by the solid state reaction method. High purity powders of CaCO$_3$, TiO$_2$ and Mn$_2$O$_3$ were used as starting materials. These powders were weighed by changing the concentration of Mn ions, which were mixed and ground in an agate mortar for 30 min. with ethanol. After drying these mixtures, they were calcined in air for 2 hrs at 1423 K. Resultant powders were mixed and ground again, which were pressed into pellet form. These pellets were sintered in air at 1523 K for 6 hrs.

Crystal structures of the sintered samples were examined by the powder X-ray diffraction with Cu-Kα X-rays. Resultant XRD patterns show no extra peaks except for those from orthorhombic perovskite structured CaTiO$_3$. In addition, lattice parameters deduced from the observed XRD pattern decrease due to the doping of Mn ions in CaTiO$_3$. These results suggest doped Mn ions are substituted at one of the cation sites, i.e., Ca^{2+} or Ti^{4+} sites, in CaTiO$_3$.

Mn-L$_3$ X-ray absorption spectrum of Mn doped CaTiO$_3$ were measured at BL4B in UVSOR. Incident beam was monochromatized by varied-spacing plane grating (800 l/mm) and energy resolution was tuned by controlling the heights of the slits settled at upper and lower reaches of grating. Samples were placed on the carbon adhesive tape, which was attached on the first Cu-Be dinode of the electron multiplier. All the XAS measurements were carried out in a total electron yield (TEY) mode by collecting the sample drain current.

Observed Mn-L$_3$ XAS spectrum of Mn-doped CaTiO$_3$ is shown in Fig. 1 together with those of MnO (Mn^{2+}) and MnO$_2$ (Mn^{4+}), in which that of MnO$_2$ shows much better agreement with experimental profile of Mn-doped CaTiO$_3$. From these results, i.e., reduction of cell parameter by XRD and XANES analysis, it can be concluded that Mn ions are substituted as Mn^{4+} ions in CaTiO$_3$.
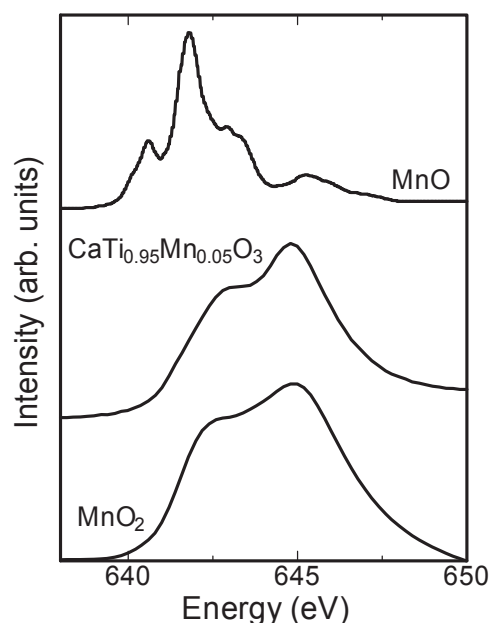

Fig. 1. Observed Mn-L$_3$ X-ray absorption spectra of Mn-doped CaTiO$_3$ (middle) and Mn oxides (MnO: top and MnO$_2$: bottom).

[1] X. Q. Chen et al., Solid State Comm. **150** (2010) 1221.
[2] K. Nishimura et al., IEEE Trans. Mag. **50** (2014) 2502306.
[3] K. Nishimura et al., UVSOR Activity Report 2013.

BL4B

Effect of Carbon Substitution on the Magnetic Properties of Nano-Architectural ZnO

Y. F. Wang[1], W. F. Pong[1], J. W. Chiou[2], Y. Takagi[3], T. Ohigashi[3], T. Yokoyama[3] and N. Kosugi[3]

[1]*Department of Physics, Tamkang University, Tamsui 251, Taiwan*
[2]*Department of Applied Physics, National University of Kaohsiung, Kaohsiung 811, Taiwan*
[3]*UVSOR Synchrotron, Institute for Molecular Science, Okazaki 444-8585, Japan*

Based on our previous publication in Nanoscale 6, 9166-9176 (2014) entitled "Observation of the origin of d^0 magnetism in ZnO nanostructure using x-ray-based microscopic and spectroscopic techniques", we observed zinc vacancies (V_{Zn}) induced orbital moments in oxygen sites near the surface of nano-architectural ZnO via combined synchrotron based techniques and first principle calculations [1]. Moreover, since the carbon-doped ZnO have been proposed and observed to be ferromagnetic with Curie temperature well above room temperature, and different carbon-related defects can result entirely different magnetism in carbon-doped ZnO as theoretically predicted. The correlation between carbon-related defects and magnetism has become an important issue experimentally for non-magnetic impurities induced dilute magnetic semiconductors. Due to this novel but controversial issue, nano-architectural ZnO is an ideal system to investigate. The defects-related phenomenon due to the large surface to volume ratio and intrinsic V_{Zn} on the surface of nanostructures provide an opportunity to study how carbon implantation affects the electronic structures and magnetism of ZnO.

Figure 1 shows the C K-edge XANES and XMCD spectrum of (a) carbon-implanted ZnO nano-wires (C:NWs) and (b) carbon-implanted ZnO nano-cactus (C:NCs). The XMCD signals appear around 287-292 eV suggest the origin of enhancement in room temperature ferromagnetism (RTFM) of carbon-implanted nano-architectural ZnO can be correlated to π-like hybridization states between carbon and oxygen [2], or zinc atoms. A weaker XMCD signal shows in C:NCs with respect to NWs suggests V_{Zn} may suppress ferromagnetic ordering between magnetic-impurities since C:NCs contain higher density of V_{Zn} which provides higher possibility for carbon substitution into V_{Zn} sites and hybridize with oxygen to form non-spin-polarized C_{Zn} [3]. Carbon substituted oxygen (C_O) can introduce holes into system which satisfies Stoner criterion easily and results stronger localization spins in carbon with respect to V_{Zn} [4]. Spin-polarized C_{Zn}-C_I (interstitial carbon) complex in V_{Zn} sites should be considered since highly dense C_I can form carbon-related complexes easily, but relatively weak magnetization and XMCD signal in C:NCs with respect to C:NWs suggests dominant spin-polarized carbon impurity is C_O [5].
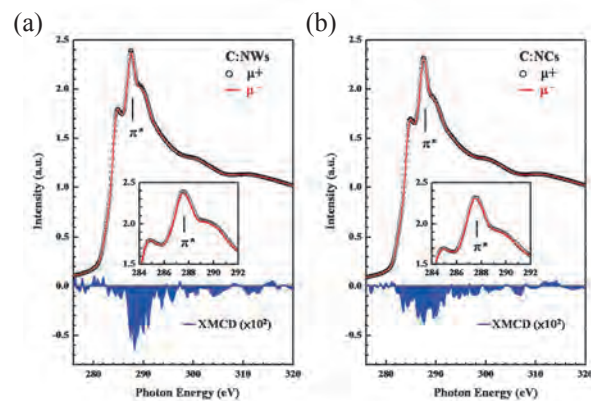

Fig. 1. C K-edge XANES and XMCD spectrum of (a) C:NWs and (b) C:NCs.

[1] Shashi B. Singh Nanoscale **6** (2014) 9166.
[2] Y. F. Wang *et al.,* Sci. Rep. **5** (2015) 15439.
[3] S. K. Nayak *et al.*, Phys. Rev. B **86** (2012) 054441.
[4] H. Peng *et al.*, Phys. Rev. Lett. **102** (2009) 017201.
[5] S. Sung *et al.*, Semicond. Sci. Technol. **26** (2011) 014038.

UV-Induced Infrared Absorption Change in SrAl$_2$O$_4$:Eu Crystals: Influence of Eu^{2+} Concentration on Trap Filling Process

Y. Tsurumi[1], M. Kitaura[1], A. Ohnishi[1], T. Ishibashi[2], S. Furukawa[2], H. Oda[2] and A. Yamanaka[2]

[1]*Facalty of Science, Yamagata University, Yamagata 990-8560, Japan*
[2]*Chitose Institute of Science and Technology, Chitose 444-8585, Japan*

The control of shallow electron traps is most significant in the development of high luminance long-persistent phosphors. So far, the energies of trap depths have been evaluated from both sides of experimental and theoretical approaches. The so-called "Dorenbos model" [1] provides us fruitful information on the optimization of co-dopants working as photocarrier traps. On the other hand, the trap filling process is also important; however, it has not been discussed so much, and still remains obscure. It is thus necessary to clarify the factors dominating the trap filling process, and to determine the optimal condition which gives rise to high luminance long persistent phosphorescence. For these purposes, we have studied the influence of europium concentration on trap filling process in SrAl$_2$O$_4$:Eu^{2+} crystals grown by the Floating zone method.

Figure 1 shows absorption spectra of SrAl$_2$O$_4$:Eu crystals with europium concentrations of 0.1 (a), 0.3 (b), and 1 mol% (c). These data were observed at 9 K. Blue and red lines indicate absorption spectra observed before and after UV-irradiation at 375 nm, which can cause long persistent phosphorescence [2,3]. An absorption band appears around 2000 cm^{-1} under UV-irradiation. The UV-induced band around 2000 cm^{-1} could not be observed for undoped SrAl$_2$O$_4$ crystals. This result suggests that the Eu^{2+} 4f-5d absorption triggers an appearance of the UV-induced band. According to the Dorenbos model, the lowest-energy 5d level in the Eu^{2+} 4f^5 5d^1 configuration locates just below the bottom of the conduction band of host SrAl$_2$O$_4$. Excited electrons at the lowest-energy 5d level can easily migrate to be trapped by lattice imperfections. Therefore, it is more likely that the UV-induced band is caused by the formation of electron traps.

The UV-induced band was weakened when the europium concentration is increased from 0.1 to 1.0 mol%. Apparently, the efficiency of trap filling is influenced by the concentration of Eu^{2+} ions. As the europium concentration becomes higher, the penetration depth becomes smaller. If excited electrons cannot migrate a long distance, they will be trapped by lattice imperfection in the vicinity of Eu^{2+} ions exited by UV-light. Since the amount of such imperfections becomes low with increasing europium concentration, the UV-induced band is weakened as we observed.

The present study demonstrated that the trap filling occurs most efficiently in the case of low Eu^{2+} concentration. This information gives a guiding principle for the material design of high luminance

long-persistent phosphors. Unfortunately, we could not exhibited UV-induced absorption change for SrAl$_2$O$_4$:Eu^{2+} crystals with Eu^{2+} concentrations less than 0.1mol%, because of difficulties for adjusting such extremely low europium concentration. This subject is now under investigation.
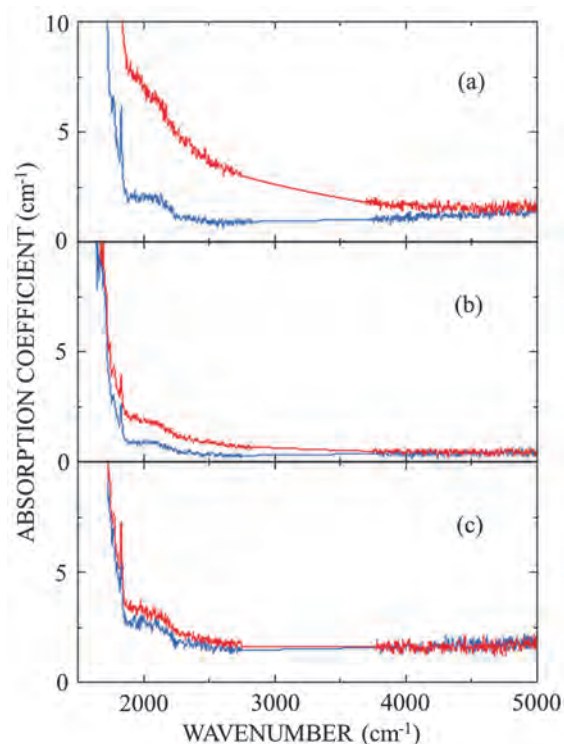

Fig. 1. Absorption spectra of SrAl$_2$O$_4$:Eu crystals with europium concentrations of 0.1 (a), 0.3 (b), and 1.0 mol% (c). These data were observed at 9 K. Blue and red lines indicate absorption spectra observed before and after UV-irradiation at 375 nm.

[1] P. Dorenbos and J. J. Bos, Rad. Meas. **43** (2008) 139.
[2] Y. Kamiyanagi *et al.*, J. Lumi. **122-123** (2007) 509.
[3] M. Kitaura, J. Ceram. Proc. Res. **12** (2011) s33.

BL6B

Suppression of Electron Traps in Ce:GAGG Crystals by Mg^{2+} Co-Doping

R. Inaba[1], M. Kitaura[2], K. Kamada[3], S. Kurosawa[3], A. Ohnishi[2] and K. Hara[4]

[1] Graduate School of Science and Engineering, Yamagata University, Yamagata 990-8560, Japan
[2] Department of Physics, Faculty of Science, Yamagata University, Yamagata 990-8560, Japan
[3] New Industry Creation Hatchery Center, Tohoku University, Sendai 980-8579, Japan
[4] Reserch Institute of Electronics, Shizuoka University, Hamamatsu 442-8529, Japan

Cerium doped $Gd_3Al_2Ga_3O_{12}$ (Ce:GAGG) crystals have been developed as an inorganic scintillator with excellent features such as high density, high light yield, and short decay time [1]. The scintillation properties are influenced by the existence of lattice imperfections, because they are responsible for the occurrence of delayed luminescence [2]. In order to improve scintillation properties, it is necessary to find out how to suppress lattice imperfections in the process of crystal growth. Therefore, the information of crystal defects is indispensable. Recently, it was reported that co-doping of alkali-earth ion is effective for the improvement of scintillation properties [3]. However, the mechanism of such alkali-earth ion co-doing has not yet been clarified. So far, we have investigated infrared absorption spectra of Ce:GAGG crystals under UV-irradiation at low temperatures [4]. The data were limited in the energy range of 0.05-1.2 eV. In the present study, we have extended the measurement of absorption spectra to higher energy side. Furthermore, we have investigated UV-induced absorption change for Mg co-doped Ce:GAGG (Ce,Mg:GAGG) crystals.

Ce:GAGG and Ce,Mg:GAGG were grown by the Cz method. The concentration of cerium and magnesium ion was set to 1.0 and 0.1 mol%, respectively. Experiment was performed at the beamline BL6B of UVSOR. The UV-irradiation was carried out at 3.31 eV with a picosecond light pulser. The sample temperature was set to 9K.

Figure 1 shows absorption spectra of Ce:GAGG crystals. A black line represents the absorption spectrum obtained before UV-irradiation. When the UV-irradiation is turned on, the absorption spectrum exhibits a broad band with the peak at 1.5 eV, as indicated by a blue line. The UV-light can excite electrons to a Ce^{3+} 5d level in the conduction band, and triggers the formation of electron traps [4]. In addition, the Ce^{3+} 4f-4f peak around 0.5 eV is weakened by 3 % under UV-irradiation at 9K. As the formation of electron traps is responsible for the weakening of the Ce^{3+} 4f-4f peak, the concentration of electron traps is estimated to be 10^{18} cm^{-3}. This value is two orders of magnitude higher than the concentration of lattice imperfections in typical intrinsic semiconductors.

Figure 2 shows absorption spectra of Ce,Mg:GAGG crystals before and after UV-irradiation. The UV-induced band around 1.5 eV

disappears by Mg ion co-doping. This fact indicates that the Mg co-doping hinder the formation of electron traps. There are two hypotheses concerning the rope of Mg co-doping: One is that Mg^{2+} ions play as charge compensators to suppress lattice imperfections, and the other is that electron traps are destabilized by controlling the energy band of host crystals. Further experimental works are needed to solve the role of Mg co-doping.
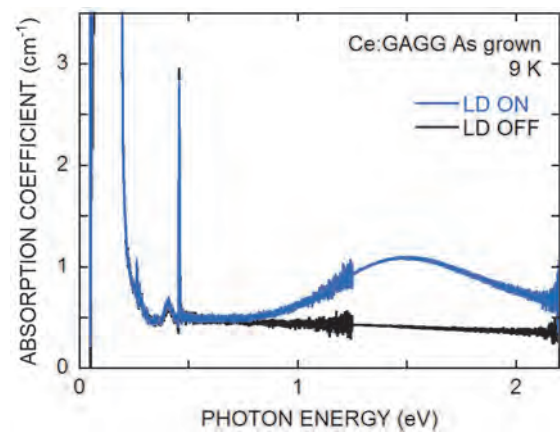

Fig. 1. UV-induced change of absorption spectra in Ce:GAGG crystals measured at 9 K.
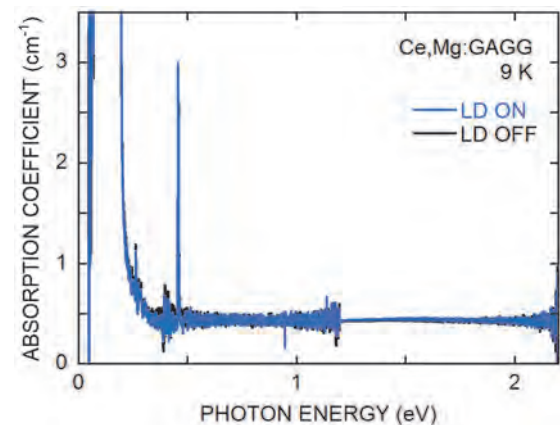

Fig. 2. UV-induced change of absorption spectra in Ce,Mg:GAGG crystals measured at 9 K.

[1] K. Kamada et al., J.Cryst. Growth 352 (2012) 82.
[2] M. Kitaura et al., J. Appl. Phys. 115 (2014) 083517.
[3] K. Kamada et al., Opt. Mater. 41 (2015) 63.
[4] R. Inaba et al., UVSOR Activity Report 42 (2015) 83.

BL6B

Measurement Temperature Dependency of Ultrashallow Thermal Donors and Observation of Shallow Donors in Carbon- and Hydrogen-Doped Czochralski Silicon Crystals

A. Hara and T. Awano

Department of Electronic Engineering, Tohoku Gakuin University, Tagajo 985-8537, Japan

We previously reported on ultrashallow thermal donors (USTDs) in carbon- and hydrogen-doped Czochralski silicon (CZ Si) crystals [1, 2]. USTDs are hydrogen-like donors with slightly different energy levels, some of which show negative central-cell correction. To the best of our knowledge, these are the shallowest energy levels as compared with those of previously reported donors in Si crystals. However, we identified USTDs as shallow donors by a comparison with effective-mass theory. In this study, we measured the intensity of USTDs as a function of measurement temperature to identify USTDs as shallow donors.

Carbon-doped CZ Si samples were doped with hydrogen by annealing in wet oxygen at 1300°C for 60 min. The samples were then cooled to room temperature by rapidly exposing to air. For carbon doping, the Si melt for preparing the ingot was doped with carbon powder during CZ Si crystal growth. Transmission spectra were obtained with a far-IR spectrometer of the BL6B beamline at different temperatures using a flowing cryostat.

Figure 1 shows the temperature dependency of USTDs and STD(H)s at different measurement temperatures. Both spectra decrease as the measurement temperature increases up to 70 K. Figure 2 shows variations in the peak intensity of USTDs and STD(H)s against the measurement temperature. The intensities of both defects show a similar dependency on the measurement temperature, which indicates that the energy levels of both are very close. Since STD(H)s are identified as shallow donors [3], it is reasonable that the energy levels of USTDs are very close to those of STD(H)s. This is consistent with our previous proposal that USTDs are donors with energy levels close to the conduction band.

In addition, we observed broad peaks at high measurement temperatures of around 50 K. They are indicated as A, B, and C in Fig. 1. The differences in wavenumber between A and B, and B and C, are consistent with the predictions of effective-mass theory. Thus, the peaks A, B, and C are identified as $1s-2p_0$, $1s-2p_{+-}$, and $1s-3p_{+-}$ transition of new shallow donor, respectively.

In summary, we observed the measurement temperature dependency of the spectra of USTDs. This behavior is consistent with our previous results, which were derived from effective-mass theory. Moreover, we found new broad optical absorption peaks, which is consistent with the predictions of effective-mass theory.
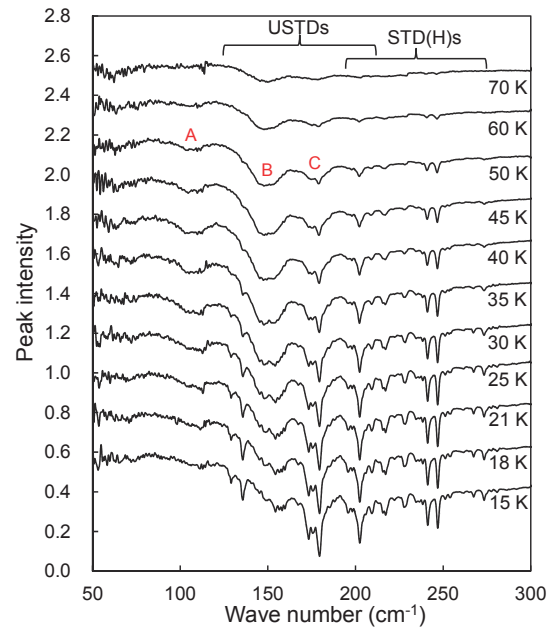

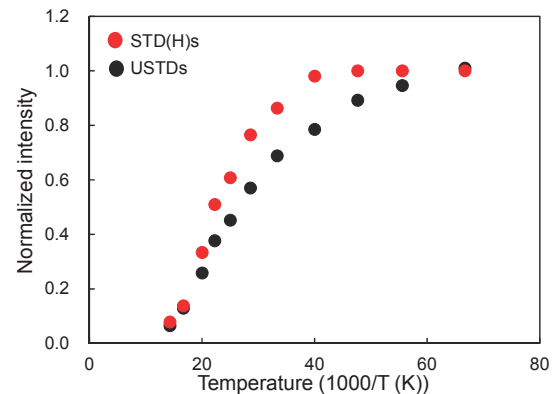Fig. 1. Temperature dependency of optical absorption peaks of USTDs and STD(H)s.

Fig. 2. Temperature dependency of USTDs and STD(H)s.

[1] A. Hara, T. Awano, Y. Ohno, and I. Yonenaga, Jpn. J. Appl. Phys. **49** (2010) 050203.
[2] A. Hara and T. Awano, Jpn. J. Appl. Phys. **54** (2015) 101302.
[3] R. C. Newman, J. H. Tucker, N. G. Semaltianos, E. C. Lightowlers, T. Gregorkiewicz, I. S. Zevenbergen, and C. A. J. Ammerlaan, Phys. Rev. B **54** (1996) R6803.

BL6B

Evaluation of Domain Wall in Alkali Niobate Piezoelectrics by Far-Infrared Reflective Method

Y. Taniguchi, N. Matsubara, K. Yoshida, T. Fuchigami and K. Kakimoto

Graduate School of Engineering, Nagoya Institute of Technology, Nagoya 466-8555, Japan

It is generally accepted that domain structure is a major factor for the origin of piezoelectric property, and specifically that domain walls contribute significantly to the properties. We evaluated domain walls both for $(Na,K)NbO_3$ crystal and ceramics by Raman spectroscopy and suggested that ferroelectric and piezoelectric properties at the walls might be different far from those of adjacent domain regions [1]. In the previous work, we observed various permittivity depending on the focused regions of $(Na,K)NbO_3$ crystal by using mid-infrared as a light source [2]. However, there were some problems of the short distance in mapping measurement and of the low intensity of Infrared(IR) reflectivity. Therefore, long-distance and high-intensity line mapping measurements were performed in this work using synchrotron radiation source, and we tried to evaluate domain walls especially for the permittivity in a stripe domain structure.

$(Na_{0.55}K_{0.45})(Nb_{0.995}Mn_{0.005})O_3$(NKN) crystal with stripe domains(20-80 μm width) was measured by a FT-IR spectrometer (Bruker, VERTEX 70v). IR measurements were performed vertically to the domain wall every 10 μm in a total range of 100 μm. The spectra were fitted to obtain permittivity according to the following equation:

$$\varepsilon(\omega) = \varepsilon_\infty + \Sigma_n \omega^2_{pn} / \omega^2_{on} - \omega^2 - n\gamma_n\omega \qquad (1)$$

where, ε_∞ is the high-frequency dielectric constant, ω_p and ω_o the plasma and longitudinal frequencies, and γ the damping constant. The complex dielectric function is related to the reflectivity spectrum by the equation

$$R = |\sqrt{\varepsilon(\omega)} - 1 / \sqrt{\varepsilon(\omega)} + 1|^2 \qquad (2)$$

Figure 1 shows IR reflectivity spectra of NKN crystal. The reflectivity was 0.6 when using mid-infrared. On the other hand, the reflectivity significantly increased by using synchrotron radiation, and it was 0.8 at a maximum even in 0.25 aperture diameter. The reason is that the synchrotron radiation had a more than 6 times larger reflection intensity in Si bolometer than that of mid-infrared. Hence, IR reflectivity measurement by synchrotron radiation should give reliable data of permittivity.

Considering the width of the stripe domains in the NKN crystal (20-80 μm), permittivity ε' should change periodically in 20-80 μm measurement range owing to the effect of domain wall. Figure 2 shows the permittivity of NKN crystal at each measurement position with an aperture diameter of 0.25 mm. The permittivity ε' showed values between 65 and 70 except at the measurement positions of 30, 50 and 100 μm. Permittivity ε' increased periodically in 20-50 measurement range, and the values at 30, 50 and 100 μm positions were approximately 80, which is approximately 20% higher compared to the other positions. These results suggested that the permittivity increases at the domain walls. Therefore, domain walls could be evaluated on the basis of the increase in permittivity by IR reflectivity measurement. In addition, we think that ferroelectric and piezoelectric properties remarkably improve with increasing the density of domain wall in the materials.
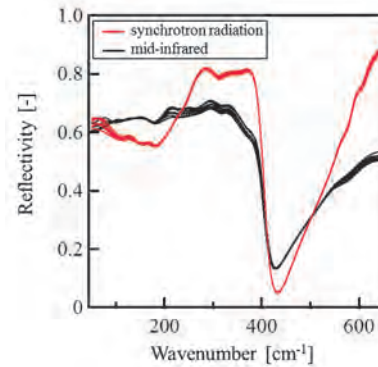

Fig. 1. IR reflectivity spectra of NKN crystal obtained using synchrotron radiation and mid-infrared as light source.
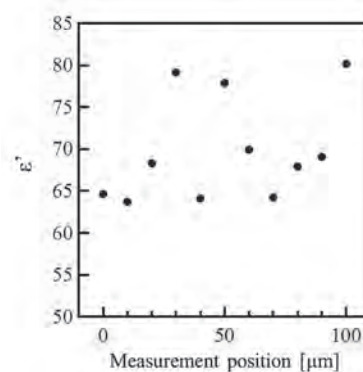

Fig. 2. Permittivity ε' of NKN crystal at measurement positions obtained using synchrotron radiation as light source.

[1] Y. Taniguchi and K. Kakimoto, Japanese Journal of Applied Physics **54** (2015) 10ND09.
[2] Y. Taniguchi, T. Yamazaki, M. Kato and K. Kakimoto, UVSOR Activity Report **42** (2015) 85.

High-Resolution ARPES Study of Noncentrosymmetric Weyl Semimetal Candidate NbP

S. Souma[1], Z. Wang[2], H. Kotaka[2], T. Sato[3], K. Nakayama[3], Y. Tanaka[3], H. Kimizuka[3],
K. Yamauchi[2], T. Oguchi[2], K. Segawa[4], Y. Ando[2,5] and T. Takahashi[1,3]

[1]WPI Research Center, Advanced Institute for Materials Research, Tohoku University, Sendai 980-8577, Japan
[2]Institute of Scientific and Industrial Research, Osaka University, Ibaraki 567-0047, Japan
[3]Department of Physics, Tohoku University, Sendai 980-8578, Japan
[4]Department of Physics, Kyoto Sangyo University, Kyoto 603-8555, Japan
[5]Institute of Physics II, University of Cologne, Köln 50937, Germany

Weyl semimetals (WSMs) manifest a novel quantum state of matter where the bulk conduction and valence bands cross at discrete points, defined as Weyl nodes, with linear dispersion in all the momentum (k) directions in three-dimensional Brillouin zone, which can be viewed as a three-dimensional analogue of graphene breaking time-reversal or space-inversion symmetry [1,2]. The WSMs can host many exotic physical phenomena such as anomalous Hall effects, chiral anomalies, and magnetoelectric effects. The most intriguing prediction for WSMs is the emergence of Fermi arcs on their surfaces. Unlike two-dimensional metals showing *closed* Fermi surface (FS), the Fermi arcs in WSMs are disjoint, *open* curves. Recently, density functional theory predicted that noncentrosymmetric transition-metal monopnictide family TaAs, TaP, NbAs, and NbP are WSMs [3,4]. To firmly establish the WSM nature of monopnictides and to build a basis for the proposed exotic phenomena, it is of particular importance to experimentally establish the fermiology of transition-metal monopnictide family.

In this study, we have performed high-resolution angle-resolved photoemission spectroscopy (ARPES) of NbP. By utilizing the low photon energy and variable polarization characteristics of the beamline BL-7U, we have succeeded in observing the fine electronic structure that supports the WSM nature of NbP [5].

Figure 1(a) displays a schematic summary of the experimentally observed FS of NbP around $\bar{\mathrm{X}}$. The energy bands labeled here, S_1-S_4, all of which are surface states, obey different selection rules of photoelectron intensity. For example, band S_1 is dominantly seen with vertical polarization [Fig. 1(b)]. On the other hand, the intensity of outer band S_2, which forms a tadpole FS, is greatly enhanced with circularly polarized photons [Fig. 1(c)]. There exist another dog-bone-shaped FSs, S_3 and S_4, elongated along $\bar{\mathrm{X}}$ $\bar{\mathrm{M}}$, which are better resolved with horizontally polarized photons [Fig. 1(d)]. We found that overall cross-shaped FS in the experiment is reasonably reproduced by our calculation and the FS (S_2) which connects Weyl nodes $W2^{\pm}$ can be viewed as a combination of two Fermi arcs. Namely, one arc starts and ends at W2, and the other is connected to W1. It is thus likely that only S_2 forms a Fermi arc and all the others (S_1, S_3, and S_4) form trivial FS.

To examine the WSM nature of NbP, we choose closed k-loop ($\bar{\Gamma}$- $\bar{\mathrm{X}}$- $\bar{\mathrm{M}}$- $\bar{\Gamma}$) surrounding the odd number of (three) Weyl nodes and counted the total number of FS crossings. Since only an open Fermi arc can cross this loop an odd number of times, the total odd number of FS crossings would be a hallmark of the existence of Fermi arcs in WSM. As seen from Fig. 1(a), the Fermi arc (S_2) crosses this loop only once, and the trivial FSs (S_1, S_3, and S_4) cross six times. Therefore the observed FSs cross the k-loop seven times in total, supporting the WSM nature of NbP. The present result opens a pathway for the Fermi-arc engineering of Wey semimetals.
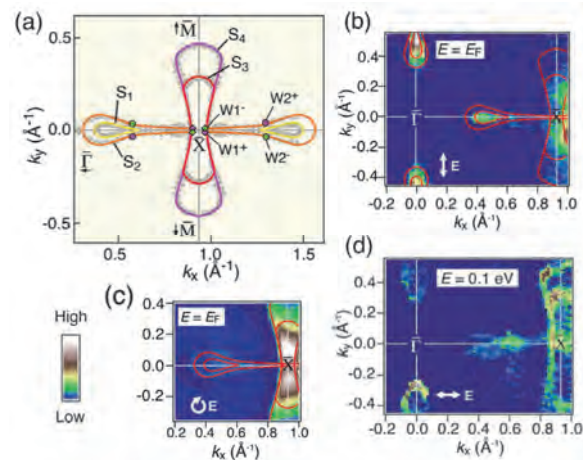

Fig. 1. (a) Experimental FS around $\bar{\mathrm{X}}$ of NbP. (b)-(d) Second-derivative intensity of the ARPES spectra measured with vertically-, circularly-, and horizontally-polarized photons, respectively. Polarization vector of lights is indicated by arrow.

[1] X. Wan *et al*., Phys. Rev. B **83** (2011) 205101.
[2] L. Balents, Physics **4** (2011) 36.
[3] H. Weng *et al*., Phys. Rev. X **5** (2015) 011029.
[4] S.-M. Huang *et al*., Nature Commun. **6** (2015) 7373.
[5] S. Souma *et al*., arXiv:1510.01503. (Phys. Rev. B Rapid Commun., *in press*)

BL7U

Angle-Resolved Photoemission Study of the Quasi-One-Dimensional Organic Conductors (TMTTF)$_2$X (X = AsF$_6$, SbF$_6$)

T. Ito[1,2], A. Kawakita[1], T. Hajiri[1], K. Tanaka[3,4], S. Kimura[5,6] and T. Nakamura[3,4]

[1]Graduate School of Engineering, Nagoya University, Nagoya 464-8603, Japan
[2]Nagoya University Synchrotron Radiation Research Center, Nagoya University, Nagoya 464-8603, Japan
[3]Institute for Molecular Science, Okazaki 444-8585, Japan
[4]School of Physical Sciences, SOKENDAI (The Graduate School of Advanced Studies), Okazaki 444-8585, Japan
[5]Graduate School of Frontier Biosciences, Osaka University, Osaka 565-0871, Japan
[6]Department of Physics, Osaka University, Osaka 565-0871, Japan

The Fabre salts (TMTTF)$_2$X and Bechgaard salts (TMTSF)$_2$X (X = PF$_6$, AsF$_6$, etc.) belong to a family of quasi-one-dimensional organic conductors. As the chemical pressure of the system tuned with the combination of TMTTF/TMTSF and anion X, these materials allow for a variety of ground states, such as antiferro magnetic insulator, spin-Peierl state, spin-density wave state and superconductor; furthermore one observes a crossover from a Luttinger liquid toward a Fermi-liquid metal, charge-ordred (CO) and charge-localized (loc.) insulator [1, 2].

In this study, we have performed temperature dependent angle-resolved photoemission spectroscopy (ARPES) on single-crystalline (TMTTF)$_2$X (X = AsF$_6$, SbF$_6$) to clarify the relation between the electric structure and the thermodynamic properties. ARPES measurement were performed at UVSOR-Ⅲ BL7U by utilizing the bulk-sensitive low photon energy (hν = 8 eV) as well as the micro focus beam (15×100 μm^2).

Figures 1 (A1-A8) and (S1-S6) show the temperature dependence of ARPES image along the ΓX direction of (TMTTF)$_2$AsF$_6$ and (TMTTF)$_2$SbF$_6$, respectively. The schematic illustrations of the corresponding electronic structure have been shown in Fig. 1 (M1) and (M2) for comparison. At low temperature CO states (T = 30 K < T_{CO} = 102 and 157 K for X = AsF$_6$ and SbF$_6$, respectively [3]), we found highly dispersive band away from the Fermi level (E_F) which is accompanied with the lower energy shoulder around X point, and that the band folded around the top of the dispersive features ($k_F \sim 0.25$ and 0.2 Å^{-1} for X = AsF$_6$ and SbF$_6$, respectively). From the comparison with the previous ARPES results of metallic (TMTSF)$_2$X [4, 5], we have expected that the observed dispersive features can be ascribed as the spinon and holon bands, which is characterized by the spin-charge separation in the one-dimensional system (Figs. 1 (M1) and (M2)).

With increasing temperature, the main dispersive feature of X = AsF$_6$ and SbF$_6$ gradually becomes weak around T = 50 – 150 K and T = 100 – 200 K, respectively. On the other hand, at T = 200 – 300 K, the broad non-dispersive feature (shaded area in Figs.1 (M1) and (M2)) around 1 eV dominates the electronic structure of both compounds, though the

slight dispersive feature remains in X = AsF$_6$. The observed temperature dependence seems to roughly scale with the charge-order transition temperature of each compound. Therefore, we expect that the observed spectral weight transfer from the dispersive spinon-holon bands near E_F to the localized bound state is caused by the transition from charge-ordered insulator to charge-localized state. It should be noted that the metallic states of (TMTTF)$_2$AsF$_6$ at T = 300 K have been found as a sizable spectral weight at E_F originating from the tail of the localized bound states.
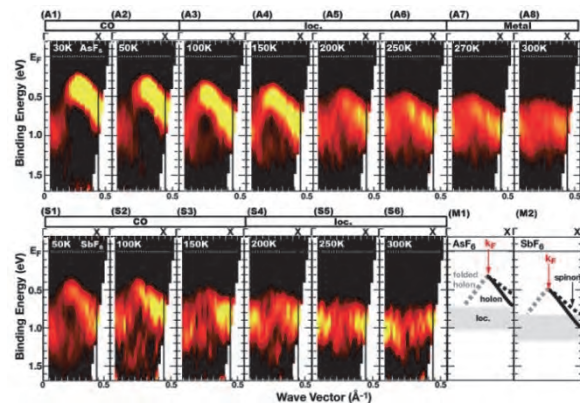

Fig. 1. Temperature dependence of ARPES images of (TMTTF)$_2$AsF$_6$ (A1-A8) and (TMTTF)$_2$SbF$_6$ (S1-S6) along ΓX direction. (M1, M2) The schematic picture of spinon-holon dispersions (solid and dashed lines) and localized bound state (shaded area) of (TMTTF)$_2$AsF$_6$ (M1) and (TMTTF)$_2$SbF$_6$ (M2), respectively.

[1] T. Ishiguro et al., Organic Superconductors (Springer-Verlag, Berlin, 1998).
[2] E. Rose et al., J. Phys.: Condens. Mat. **25** (2013) 014006.
[3] M. Dressel et al., Adv. Cond. Mat. Phys. **2012** (2012) 398721.
[4] S. Hirate et al., UVSOR Activity Report **39** (2012) 97.
[5] M. Mitamura et al., UVSOR Activity Report **40** (2013) 110.

BL7U

Systematic Change of Fermi Surfaces with As Doping in Iron Pnictide Superconductor NdFeP$_{1-x}$As$_x$(O,F)

S. Miyasaka[1], A. Takemori[1], T. Adachi[1], M. Uekubo[1], T. Kobayashi[1], S. Tajima[1], T. Hajiri[2,3],
M. Matsunami[3,4] and K. Tanaka[3,4]

[1]*Department of Physics, Graduate School of Science, Osaka University, Toyonaka 560-0043, Japan*
[2]*Department of Crystalline Materials Science, Graduate School of Engineering, Nagoya University, Nagoya 464-8603, Japan*
[3]*UVSOR Facility, Institute for Molecular Science, Okazaki 444-8585, Japan*
[4]*School of Physical Sciences, The Graduate University for Advanced Studies (SOKENDAI), Okazaki 444-8585, Japan*

The iron-based superconductors have various Fermi surface states, which are closely related with the local crystallographic structure around Fe ion. Recently, we studied the physical properties in 1111-type P/As solid solution system, RFeP$_{1-x}$As$_x$O$_{0.9}$F$_{0.1}$ (R = La, Pr and Nd). In these systems, the local structural parameters coupled with Fermi surface conditions are systematically varied by P/As solid solution. Our results have revealed that these systems have two different Fermi surface states and nesting conditions below and above $x = 0.6 \sim 0.8$ [1, 2]. To observe the change of Fermi surfaces by P/As solid solution directly, we have investigated the angle resolved photoemission spectroscopy using single crystals of NdFeP$_{1-x}$As$_x$(O,F) with x = 0.4, 0.8 and 1.0 for F concentration $y \sim 0.1$.

The single crystals of NdFeP$_{1-x}$As$_x$(O,F) were grown by high pressure technique using cubic anvil press and self-flux method [3]. T_c of the single crystals in the present work were 12 K for $x = 0.4$, 23 K for $x = 0.8$ and 44 K for $x = 1.0$, respectively. The angle resolved photoemission spectroscopy were measured at BL7U of UVSOR facility in Institute for Molecular Science using incident photons with $h\nu$ = 36 eV linearly polarized.

As shown in Figs. 1(a)-(f), the results of angle resolved photoemission spectroscopy indicate the existence of three hole and two electron Fermi surfaces in $x = 0.4$, and two hole and two electron ones in $x = 0.8$ and 1.0 samples, i.e. the change of FS state around $x = 0.8$. The orbital characters of these Femi surfaces and electronic bands have been assigned by polarization-dependent angle resolved photoemission spectroscopy, and the d_{xz} hole band around zone center particularly shows the systematic and important x dependence. As shown in Fig. 1(c), the d_{xz} hole Fermi surface exists around zone center at $x = 0.4$. The energy level of d_{xz} band decreases with increasing x, and this band almost sinks below Fermi energy in the $x = 0.8$ sample. With further increasing x, this d_{xz} Fermi surface completely disappears at $x=1.0$ (See Fig. 1(a).).

Other distinct change of Fermi surfaces has been observed around zone boundary. In the $x = 0.4$ and 0.8 samples, we observed two electron Fermi surfaces with circle or elliptic shapes around zone boundary. In

$x = 1.0$, however, the quietly different Fermi surfaces exist. As shown in Figs. 1(a) and (d), this sample has the electron Fermi surface with circle shape and the propeller-like one. These clear changes of Fermi surfaces around zone center and boundary at $x \sim 0.8$ are related with the change of transport and other properties, and supports the scenario of two T_c-rising mechanisms and two Fermi surface states in RFeP$_{1-x}$As$_x$(O,F).

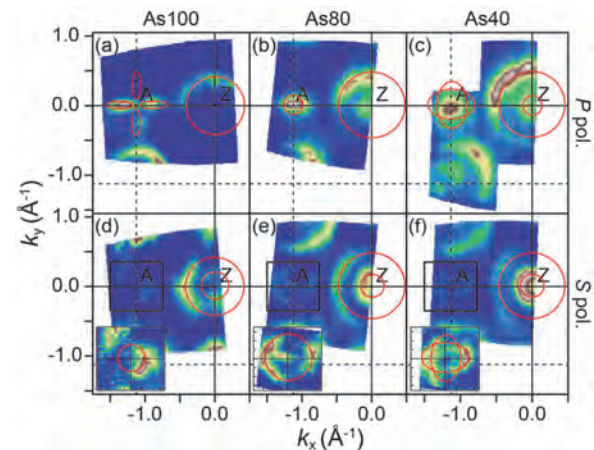Fig. 1. Fermi surface mapping on k_x-k_y plane of NdFeP$_{1-x}$As$_x$(O,F) with $x = 1.0$ (As100) ((a) and (d)), $x = 0.8$ (As80) ((b) and (e)) and $x = 0.4$ (As40) ((c) and (f)), respectively. The upper and lower panels show the results by using P- and S-polarization configurations, respectively. The insets of panel (d)-(f) show the detail of Fermi surface mapping around zone boundary in the S-polarization configuration. The red lines indicate the observed Fermi surfaces.

[1] S. Miyasaka *et al.*, J. Phys. Soc. Jpn. **82** (2013) 124706.
[2] K. T. Lai *et al.*, Phys. Rev. B **90** (2014) 064504.
[3] A. Takemori *et al.*, JPS Conf. Proc. **1** (2014) 012111.

BL7U

Electronic Structure of Sr$_{1-x}$Ca$_x$Fe$_2$(As$_{1-y}$P$_y$)$_2$ (x = 0.08, y = 0.25) Revealed by Angle Resolved Photoemission Spectroscopy

T. Adachi[1], S. Ideta[2,3], K. Tanaka[2,3], S. Miyasaka[1] and S. Tajima[1]

[1]Graduate School of Science, Department of Physics, Osaka University, Toyonaka 560-0043, Japan
[2]UVSOR Facility, Institute for Molecular Science, Okazaki 444-8585, Japan
[3]School of Physical Sciences, The Graduate University for Advanced Studies (SOKENDAI), Okazaki 444-8585, Japan

It is well known that there is a remarkable correlation between a crystal structure and T_c in iron based superconductor. Thus, it is essential for unraveling the superconducting (SC) mechanism in this system to clarify how the electronic structure changes with the crystal structure. Recent ARPES study has reported that in SrFe$_2$(As$_{1-y}$P$_y$)$_2$ whose c/a (the ratio of a- and c-axes lattice constants), which is index of structural anisotropy, is smaller than that of BaFe$_2$(As$_{1-y}$P$_y$)$_2$, innermost d_{xy} hole Fermi surface shrinks and splits into two pockets, while in BaFe$_2$(As$_{1-y}$P$_y$)$_2$, all the hole Fermi surfaces are connected in the entire k_z region [1, 2]. The reason is considered to be the stronger three-dimensionality (3D) in SrFe$_2$(As$_{1-y}$P$_y$)$_2$ originates from enhanced interlayer hopping matrix elements due to the smaller c-axis lattice constant and thus structural anisotropy (c/a).

In this measurement, we observed the electronic structure of Sr$_{1-x}$Ca$_x$Fe$_2$(As$_{1-y}$P$_y$)$_2$ (x = 0.08, y = 0.25, T_{cmax}=32K) whose c/a is smaller than that of SrFe$_2$(As$_{1-y}$P$_y$)$_2$ and whose Fermi surfaces are considered to be more three-dimensional. A momentum distribution curve (MDC), a E-k intensity plot and a second derivative plot of hole Fermi surfaces around Γ point measured by using linearized s-polarized light are shown in Fig. 1. As seen in Fig. 1, around Γ point, the hole band whose orbital character is assigned to d_{xy} sinks below E_F, consistent with the ARPES result of SrFe$_2$(As$_{1-y}$P$_y$)$_2$. Figure 2 shows SC gaps around Γ and X points as a function of θ_{FS} in Sr$_{1-x}$Ca$_x$Fe$_2$(As$_{1-y}$P$_y$)$_2$ (x = 0.08, y = 0.25). SC gaps of hole Fermi surface around Γ point are isotropic within the error bar. On the other hand, SC gaps of electron Fermi surface around X point show a different behavior. The SC gap for outer α electron Fermi surface decreases rapidly toward θ_{FS} ~ 40 deg and at θ_{FS} ~ 40 deg, node of SC gap is observed. Moreover, the SC gap for inner β electron Fermi surface decreases gently with θ_{FS} increasing. These SC gap anisotropy are different from those of BaFe$_2$(As$_{1-y}$P$_y$)$_2$ (y=0.30) [3] and it suggests that there is a relationship between SC gap anisotropy and structural anisotropy (c/a).

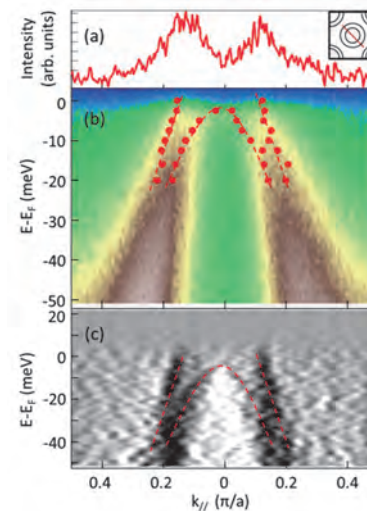Fig. 1. The electronic structure of Sr$_{1-x}$Ca$_x$Fe$_2$(As$_{1-y}$P$_y$)$_2$ (x = 0.08, y = 0.25) around Γ point. (a) MDC at E_F, (b) E-k intensity plot, and (c) second derivative plot.
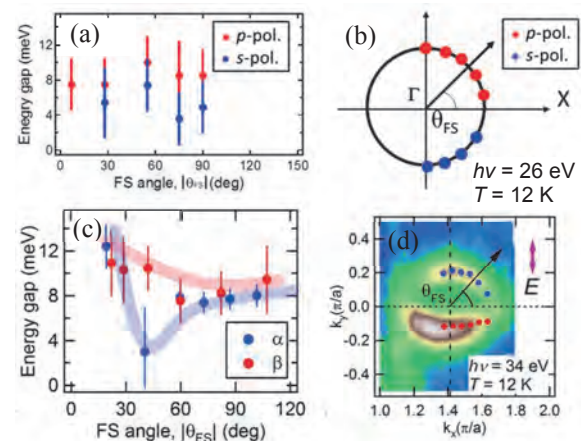

Fig. 2. (a), (c) SC gaps around Γ and X points as a function of θ_{FS} in Sr$_{1-x}$Ca$_x$Fe$_2$(As$_{1-y}$P$_y$)$_2$ (x = 0.08, y = 0.25). (b), (d) k_F around Γ and X point where SC gaps were measured. The Fermi angle is defined so that the Γ-X line is θ_{FS} = 0 deg.

[1] T. Yoshida et al., Phys. Rev. B **106** (2011) 117001.
[2] H. Suzuki et al., Phys. Rev. B **89** (2014) 184513.
[3] T. Yoshida et al., Sci. Rep. **4** (2014) 7292.

BL7U

Superconducting Gap of the Electron-Doped Cuprate Superconductor Pr$_{1.3-x}$La$_{0.7}$Ce$_x$CuO$_4$ Studied by Angle-Resolved Photoemission Spectroscopy

M. Horio[1], K. Koshiishi[1], T. Ohgi[2], S. Ideta[3], K. Tanaka[3], T. Adachi[4], Y. Koike[2] and A. Fujimori[1]

[1]Department of Physics, University of Tokyo, Tokyo 113-0033, Japan.
[2]Department of Applied Physics, Tohoku University, Sendai 980-8579, Japan.
[3]UVSOR Facility, Institute for Molecular Science, Okazaki 444-8585, Japan
[4]Department of Engineering and Applied Sciences, Sophia University, Tokyo 102-8554, Japan.

The momentum dependence of the superconducting (SC) gap carries rich information about the mechanism of superconductivity. While it is generally accepted that the SC gap of hole-doped cuprates has d-wave symmetry, the symmetry for electron-doped cuprates is still controversial.

The most direct probe of the symmetry of the SC gap is angle-resolved photoemission spectroscopy (ARPES). Although rapid surface degradation and the small size of the SC gap have prevented thorough investigation of the momentum dependence [1,2], an ARPES study on optimally doped electron-doped cuprates reported that the symmetry was basically d-wave but the gap took a maximum around the hot spot where the Fermi surface and antiferromagnetic (AF) Brillouin zone boundary cross, suggesting large contribution of AF spin fluctuations to the superconductivity [3]. However, some studies have raised the possibility that the gap symmetry changes from d-wave to s-wave by electron doping [4].

Recently, a new annealing method, which is called protect annealing and conducted to remove impurity oxygen that stabilizes AF order and destroys superconductivity, has enabled superconductivity in electron-doped cuprates with less Ce concentration [5]. An ARPES study has revealed that sufficient protect annealing strongly suppresses the quasi-particle scattering at the hot spot while the SC transition temperature (T_c) remains high [6]. In order to reveal the momentum dependence of the SC gap of protect-annealed samples, we have performed ARPES measurements with higher energy resolution.

Pr$_{1.3-x}$La$_{0.7}$Ce$_x$CuO$_4$ (x = 0.10, PLCCO) single crystals were grown by the traveling-solvent floating-zone method. We prepared two PLCCO samples which showed T_c's of 26.3 K (sample #1) and 26.9 K (sample #2) after annealing at 800 °C for 24 h. ARPES measurements were performed at UVSOR BL7U. Linearly polarized light with $h\nu$ = 16.5 eV was used. The total energy resolution was set at 8 meV. Sample #1 was measured once and Sample #2 for three times. Prior to each measurement, the samples were cleaved *in situ* under the pressure ~ 5×10^{-11} Torr.

Figure 1 shows energy distribution curves (EDCs) near (0, π) taken below and above T_c. Below T_c, the leading edge was shifted by 1.2-1.5 meV toward higher binding energy with good reproducibility, suggesting the opening of SC gap, although the amount of shift was a little smaller than 1.9 meV which was reported in previous studies [2,3]. Unfortunately, we could not reveal further detailed momentum dependence during this beam time, and additional measurements are planned in the near future.
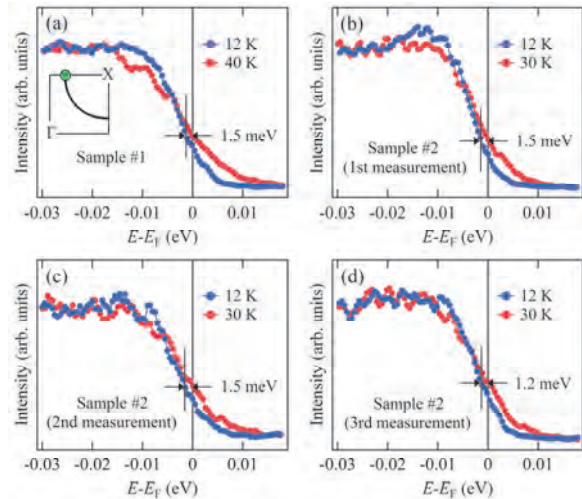

Fig. 1. SC gap of PLCCO. EDCs taken below and above T_c for (a) sample #1 and (b)-(d) sample #2. (b) to (d) are results of the first to third measurements, respectively. All the EDCs were taken at the momentum indicated by a green point in the inset of (a).

[1] T. Sato *et al.*, Science **291** (2001) 1517.
[2] N. P. Armitage *et al.*, Phys. Rev. Lett. **86** (2001) 1126.
[3] H. Matsui *et al.*, Phys. Rev. Lett. **95** (2005) 017003.
[4] J. A. Skinta *et al.*, Phys. Rev. Lett. **88** (2002) 207005.
[5] T. Adachi *et al.*, J. Phys. Soc. Jpn. **82** (2013) 063713.
[6] M. Horio *et al.*, Nat. Commun. **7** (2016) 10567.

BL7U

Electron-Phonon Scattering in Graphene: Probing of the Phonon-Dispersion by the Angle-Resolved Photoelectron Spectroscopy

S. Tanaka

The Institute of Scientific and Industrial Research, Osaka University, Ibaraki 567-0047, Japan

The electron-phonon coupling rules many properties of solids, and have been extensively studied. Recently, we proposed a new experimental method which enables us to probe the electron-phonon scattering, which is the elemental process of the electron-phono coupling, in HOPG graphite by using the angle-resolved photoelectron spectroscopy (ARPES). Here, we report an investigation using the same method for the epitaxial graphene on SiC.

The sample used was the single-layer graphene on the SiC crystal manufactured by Graphene Platform Inc. (Tokyo, Japan). ARPES measurements were carried out at the BL7U at the UVSOR facility in Institute for Molecular Science. Figure 1(a) shows the photon-energy dependence of the surface normal photoelectron spectra of the graphene. There are steps near 160meV of the binding energy at the photon energy of near 10.8eV. These steps are converted to the peak shapes by differentiating the spectra with the binding energies as shown in Fig. 1(b). The heights of the steps are plotted as a function of the photon energy [Fig. 1(c)]. There are no electronic band near the Γ-point in graphene, and in fact these steps are the Fermi edge which are shifted as much as the energy of the phonon which is scatters the electron from the Dirac cone at the K-point to the Γ-point of the unoccupied band located at 10.3eV above the Fermi level. The energy shift is due to the energy conservation rule during the phonon emission process of the electron. Possible phonon modes are LO- and TO-branches whose calculated dispersions are shown in Fig. 2(b). The ARPES map whose intensities are differentiated with the binding energy are shown in Fig. 2(c) for two directions (Γ-K and Γ-M). Obviously, the energies shift as a function of the electron-momentum. This is due to the momentum conservation rule, and these relate to the phonon dispersion. It should be noted that the electron momentum at the Fermi level of the Dirac cone is somewhat ambiguous since Fermi circle is formed in the case of the graphene/SiC due to the substrate effect. Therefore, a convolution with a phonon momentum should be taken into account. Fig. 2(d) shows simulation for the scattering process including the broadening induced by the experimental resolution. The TO-phonon is assumed in the simulation, and the agreement between the experiments and the calculation are good. The simulation assuming LO-phonon (not shown here) cannot reproduce the experiments at all, indicating that the TO-phonon is responsible for the electron-phonon scattering in this case. Although this suggests a high

efficiency of the TO-mode for the electron-phonon coupling, what observed here is the electron-phonon scattering between specific wave functions of the graphene, and detailed comparison with the theoretical calculation including the matrix elements both of the electron-phonon scattering and the optical transition will be necessary for more detailed discussion.
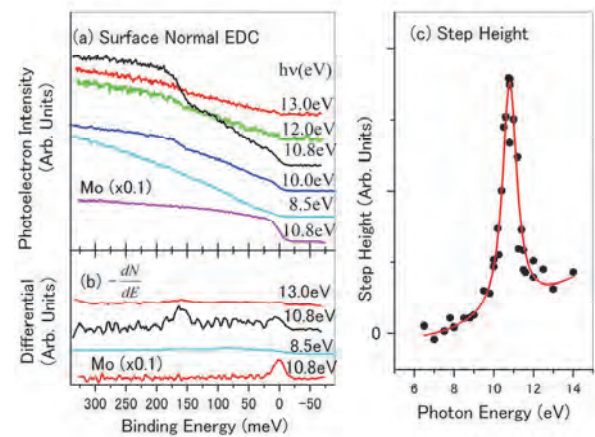

Fig. 1. (a) Surface normal ARPES spectra, (b) their differentiation, and (c) step heights in the spectra as a function of the photon energy.
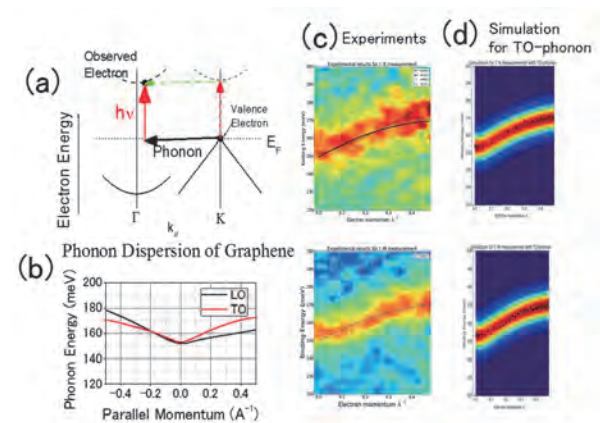

Fig 2. (a) Schematic drawing of the electron emission process, (b) phonon dispersions of graphene, (c) diffrentciated ARPES maps along the Γ-K (upper) and Γ-M (lower) directions at hv = 10.8eV (d) Simulation of the electron-phonon scattering in graphene.

BL7B

Electronic Structure and Decay Profiles of Auger-Free Luminescence from α- and β- BaLu$_2$F$_8$ Crystals

H. Tsuchida[1], S. Tanaka[2], M. Kitaura[1], A. Ohnishi[1], J. Pejchal[3], A. Yamaji[4] and S. Kurosawa[3]

[1]*Faculty of Science, Yamagata University, Yamagata 990-8560, Japan*
[2]*Faculty of Science and Engineering, Kinki University, Higashiosaka 577-8502, Japan*
[3]*New Industry Creation Hachery Center, Tohoku University, Sendai 980-8579, Japan*
[4]*Institute for Materals Research, Tohoku University, Sendai 980-8679, Japan*

Auger-Free Luminescence (AFL) is caused by radiative transition of core holes to the valence band [1]. The spectral shape and radiative lifetime of AFLs mainly reflect electronic structure such as density of states (DOS) and wave functions of valence and outermost core bands, which are dependent on local ionic or covalent bonds. AFLs of compounds with different modifications are very much interesting in controlling AFLs. From this viewpoint, we have much attention to the AFL of BaLu$_2$F$_8$. This compound has two modifications of α- and β-phases [2]. The former and latter belong to orthorhombic and monoclinic systems, respectively. The α- and β-phases are stable above and below 900 ºC, respectively. In the present study, we have studied electronic structures of α- and β-BaLu$_2$F$_8$ crystals by measurements of x-ray photoelectron spectroscopy (XPS), and reflectance spectra. Furthermore, we have measured emission spectra and decay profiles of Auger-free luminescence (AFL) from α- and β-BaLu$_2$F$_8$ crystals under the single bunch operation of UVSOR.

Figure 1 shows reflectance (red) and absorbance (blue) spectra of α- and β-BaLu$_2$F$_8$ crystals, which were measured at room temperature. The absorption edge of α-BaLu$_2$F$_8$ is higher than that of β-BaLu$_2$F$_8$. Furthermore, the reflectance spectrum of α-BaLu$_2$F$_8$ is clearly different from that of β-BaLu$_2$F$_8$. On the other hand, it was confirmed that the XPS spectra are in good agreement with each other, indicating that the electronic structures of valence and outermost core bands are almost same between them. Therefore, the difference between reflectance and absorbance spectra is attributed to that in the structure of the conduction band.

From the analysis of XPS spectra, the energy difference between the top of the valence band and that of the outermost core band was determined to be 7.9 eV, the value of which is smaller than the band-gap energy estimated from the higher energy side of the lowest reflectance peak. Therefore, it is evident that α- and β-BaLu$_2$F$_8$ crystals accompany radiative core hole transitions between the valence band and the top of the outermost core band, resulting in AFLs. Actually, emission spectra exhibited an AFL band around 5 eV. The spectral shape is same between α- and β-BaLu$_2$F$_8$ crystals. Decay profiles of the AFLs were also same, as shown in Fig. 2. The lifetimes of AFLs were determined to be 610 ps (α-BaLu$_2$F$_8$) and 560 ps (β-BaLu$_2$F$_8$), respectively. Apparently, similarities in emission spectra and decay curves of AFLs reflect the results of XPS spectra.
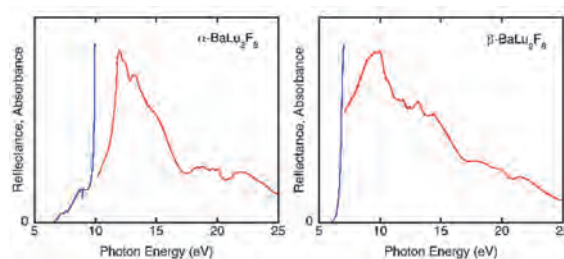

Fig. 1. Reflectance (red) and absorbance (blue) spectra of α- and β-BaLu$_2$F$_8$ crystals, measured at room temperature.
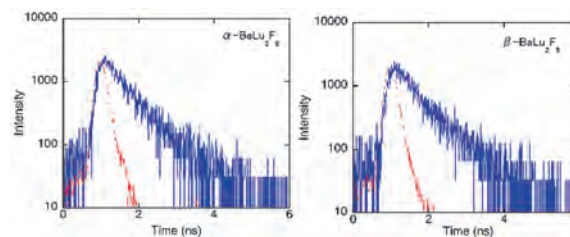

Fig. 2. Decay profiles of AFLs from α- and β-BaLu$_2$F$_8$ crystals, measured at room temperature under excitation at 21.4 eV. A red line indicates the pulse profile of an excitation light pulse.

[1] M. Itoh, Recent Res. Devel. Physics **4** (2003) 205.
[2] A. A. Kaminskii *et al.*, J. Alloys Compd. **275-277** (1998) 442.

BL7B

Analysis of the Luminescence Properties of $Gd_2Si_2O_7$:Ce and $Gd_2Si_2O_7$:La, Ce with Vacuum Ultraviolet Excitation

M. Koshimizu[1], T. Yanagida[2], Y. Fujimoto[1] and K. Asai[1]

[1] *Department of Applied Chemistry, Graduate School of Engineering, Tohoku University, Sendai 980-8579, Japan*

[2] *Graduate School of Materials Science, Nara Institute of Science and Technology, Ikoma 630-0192, Japan*

Ce-doped $Gd_2Si_2O_7$ (GPS) has been attracting considerable attention owing to its excellent scintillation properties [1]. Recently, it is proved that La-doing is an effective method to enhance the performance [2]. In this study, we analyzed the luminescence properties of Ce-doped GPS with and without La with vacuum ultraviolet (VUV) excitation to elucidate the effect of La incorporation on the energy transfer process from the host matrix to Ce^{3+} ions.

The single crystals of Ce-doped GPS with and without La incorporation were grown via floating-zone method. The luminescence properties were characterized at BL7B of UVSOR. Luminescence spectra were obtained using an optical multichannel analyzer equipped with a liquid-nitrogen-cooled CCD at different excitation wavelengths. For the measurements of luminescence time profiles, single bunch operation of UVSOR was used. The luminescence photons were monochromatized and detected with a multichannel-plate-mounted photomultiplier tube.

Figure 1 shows the luminescence spectra of the Ce-doped GPS crystals with and without La incorporation. A prominent band was observed at 370–400 nm for all the crystals, and is attributed to the $5d$-$4f$ transition of Ce^{3+}.

Figures 2 and 3, respectively, show the luminescence time profiles of the Ce-doped GPS crystals with and without La incorporation with excitation at 60 and 300 nm. The decay behavior was expressed satisfactorily with single exponential functions for all the time profiles. For GPS doped with Ce and La at 1 and 10 mol% respectively, the decay time constants were 52 and 60 ns with excitation at 300 and 60 nm, respectively. On the other hand, the decay time constants were 41 and 52 ns with excitation at 300 and 60 nm, respectively. The excitation at 300 nm corresponds to the direct excitation of Ce^{3+}, whereas the excitation wavelength at 60 nm corresponds to the host excitation. The difference in the luminescence process is that energy transfer is involved in the luminescence process for the excitation wavelength of 60 nm. It is clearly seen that the GPS crystal with La incorporation has a similar decay behavior for excitation wavelengths of 60 and 300 nm, whereas a considerable difference was observed for the GPS crystal without La. This result indicates that the La incorporation has an influence on the energy transfer process.
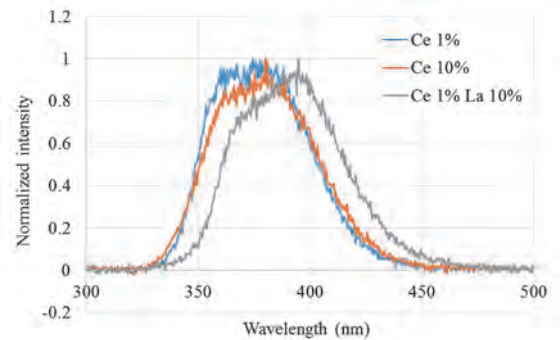

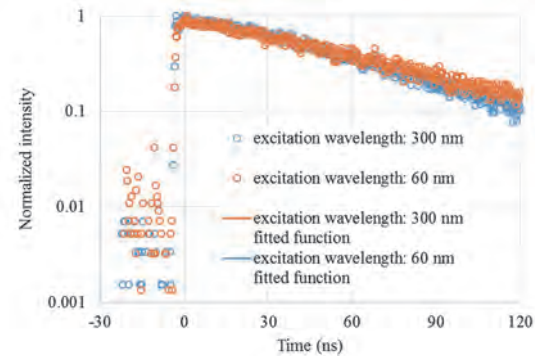Fig. 1. Luminescence spectra of the Ce-doped GPS crystals with and without La incorporation.

Fig. 2. Luminescence time profiles of GPS doped with Ce and La at 1 and 10 mol%, respectively.
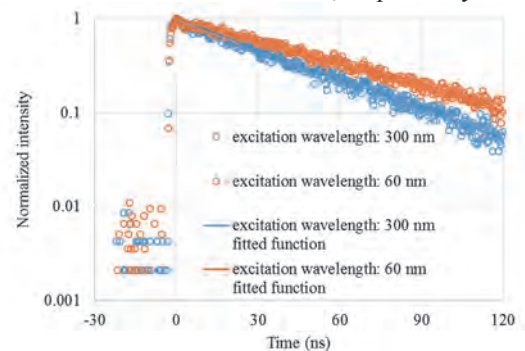

Fig. 3. Luminescence time profiles of GPS doped with Ce at 10 mol%.

[1] S. Kawamura, J. H. Kaneko, M. Higuchi, F. Fujita, A. Homma, J. Haruna, S. Saeki, K. Kurahige, H. Ishibashi and M. Furusaka, Nucl. Instrum. Methods Phys. Res. A **583** (2007) 356.

[2] S. Kurosawa, T. Shishido, A. Suzuki, J. Pejchal, Y. Yokota and A. Yoshikawa, Nucl. Instrum. Methods Phys. Res. A **744** (2014) 30.

BL7B

Influence of Barium Concentration on the Reflection Spectra for Ternary Niobium Bismuth Phosphate Glasses

N. Kitamura[1], K. Fukumi[1], Y. Hisano[2], A. Uchiyama[2] and H. Kozuka[2]

[1]National Institute of Advanced Industrial Science and Technology, Osaka 563-8577, Japan
[2]Kansai University, Osaka 564-8680, Japan

BaO-Nb_2O_5-P_2O_5 glass is one of niobium phosphate glass systems having a wide glass forming region with high Nb_2O_5 contents [1]. In this system, NbO_x polyhedra construct glass network structure with PO_4 tetrahedra. Since the glass shows high refractive index due to high niobium concentration. It is of interest for the application to optical glasses in precision optical devices. However, the glass with high niobium content gives yellowish and blue colours and the relationship between optical properties, such as refractive index, dispersion, absorption edge, etc., and structure around niobium ions or connection of niobium-oxygen polyhedra in the network structure are not clear yet. In the present study, reflectivity of the bismuth phosphate glasses has been measured to investigate compositional dependence of the band structure in the vacuum ultraviolet region.

Ternary $xBaO$-$10Nb_2O_5$-$(90\text{-}x)P_2O_5$ (x = 10, 20, 30, 40, 50 and 55 mol%) glasses and $xBaO$-$20Nb_2O_5$-$(80\text{-}x)P_2O_5$ glasses (x = 10, 20, 30, 40, 50 and 55 mol%) were prepared by using a conventional liquid-quench method. Reflectivity of optically polished samples was measured in the photon energy region of 4-25 eV with an incident angle of 10° at the BL7B. Figure 1 shows reflection spectra of the $xBaO$-$10Nb_2O_5$-$(90\text{-}x)P_2O_5$ glasses. Strong reflection peak was observed at around 9.5eV and 22 eV for all the glasses. The peak are assigned to the transition from O 2p and P 3p states to Nb 4d and Ba 5d states from a report of DFT calculation for barium niobium phosphate compounds [2]. The origin of the higher band at 22 eV is not clear yet. The unknown peak at 22 eV increased with increasing BaO content. Therefore, the peak could be due to the state of Ba^{2+}. Contrary, intensity of the 9.5 eV peak did not show remarkable change with the BaO content. However, the peak position shifted toward lower energy by about 0.3 eV, while the band width (HWHM) decreased by about 0.6 eV from an analysis of multi-Gaussian deconvolution for the K-K transformed absorption spectra. These changes predicted a higher energy shift of absorption edge energy and the prediction was consistent with the experimental result of absorption spectra in visible region [3].

On the other hand, reflection spectra of ternary $xBaO$-$20Nb_2O_5$-$(80\text{-}x)P_2O_5$ glasses are shown in Fig. 2. As shown in the figure, the similar peaks were observed. The peak around 22 eV increased with increasing BaO content. The intensity of the 9.5 eV band was almost constant against the BaO content too.
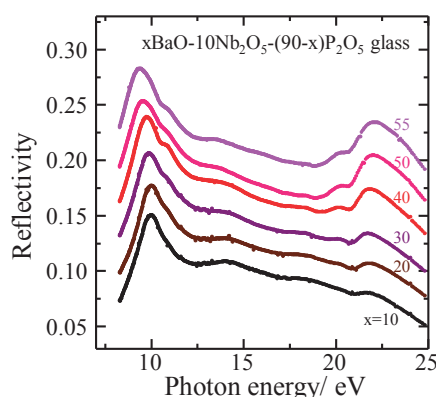
Fig. 1. Reflection spectra of ternary $xBaO$-$10Nb_2O_5$-$(90\text{-}x)P_2O_5$ glasses.
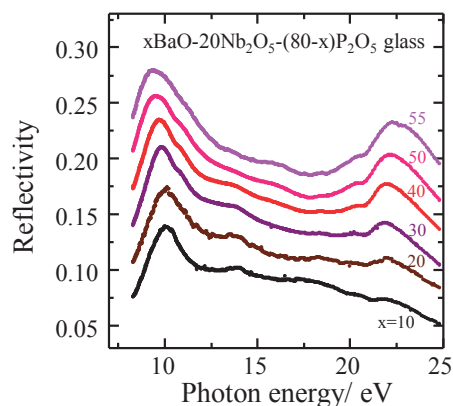

Fig. 2. Reflection spectra of ternary $xBaO$-$20Nb_2O_5$-$(80\text{-}x)P_2O_5$ glasses.

[1] N. Shcheglova and T. V. Avlas, Fiz. Khim. Stekla **16** (1990) 879.
[2] I. Cho *et al.,* Eur. J. Inorg. Chem. **2011**(2011) 2206.
[3] N. Kitamura *et al.,* Extended abstract 1st Int. Nat'l. Conf. Phosphate glasses, Pardvice, 2014.

BL7B

Optical Conductivity Spectra in the Course of Bandwidth-Control Metal-Insulator Transitions in $Nd_{1-x}Pr_xIr_2O_7$

J. Fujioka[1], K. Ueda[1] and Y. Tokura[1,2]

[1] Department of Applied Physics, University of Tokyo, Tokyo 113-8656, Japan
[2] RIKEN Center for Emergent Matter Science (CEMS), Wako 351-0198, Japan

Strongly correlated electron system has been one of the central topics in the condensed matter physics where the interplay among charge, spin, orbital degree of freedom frequently induces a variety of intriguing states. Among them, interplay between electron correlation and relativistic spin-orbit coupling in 5d-transition metal oxides has recently attracted much attention for the realization of the correlated topological insulator/semimetals [1]. The Weyl semimetal (WSM) is an example, which is characterized by a Weyl dispersion in bulk and nontrivial surface states with Fermi-arc.

The pyrochlore iridates $R_2Ir_2O_7$ (R = rare-earth, Y, and Bi ions) is one of representative materials to explore these phenomena. The metal-insulator transition (MIT) can be tuned by changing R-ions via the modulation of 5d electron hopping interaction and accordingly of effective electron correlation (U). The R = Pr compound is metallic down to the lowest temperature, while others with smaller R-ionic radius (r) thermally turns into an insulator concomitantly with or separately from the antiferromagnetic (all-in all-out) order at low temperatures. So far, there have been many theoretical studies on the evolution of electronic/magnetic state upon the MIT. For example, it is proposed that the Weyl semimetal can be realized in the vicinity of MIT. Despite extensive research, a systematic study regarding the evolution of electronic structure upon this enigmatic MIT is still lacking.

In this study, we investigate the charge dynamics upon the MIT on series of pyrochlore iridates $(Nd_{1-x}Pr_x)_2Ir_2O_7$ by means of optical spectroscopy. For the measurements, high-quality (hard, dense, and well-stoichiometric) polycrystalline samples are prepared. We measured reflectivity spectra for polycrystals of $Nd_2Ir_2O_7$ between 12 meV and 5 eV using Fourier-transform spectrometer and grating-type spectrometer in temperature range between 5 K and 290 K. We obtained the reflectivity between 5 and 30 eV at room temperature by using synchrotron radiation at BL7B in UVSOR. We determined complex optical constants through the Kramers-Kronig transformation with proper extrapolations of reflectivity in the low and high energy regions.

In Fig. 1(a), we show the optical conductivity spectra for the mixed compounds of R = $Nd_{1-x}Pr_x$ (x = 0, 0.2, 0.5, and 1) at 5 K (< T_N), which are located in vicinity to the quantum phase transition of the all-in all-out magnetic order [2]. An optical gap is observed for x = 0.5 as well as for x = 0, while the magnitude of the gap systematically decreases as x increases (0.035

eV for x = 0.2 and 0.012 eV for x = 0.5). Figure 1 (b) exhibits the T variation of optical conductivity spectra for x = 0.5. Upon cooling below T_N, the spectral weight (SW) rapidly piles up around 0.04 eV at the expense of a strong depletion of conductivity in lower energy, resulting in the formation of the charge gap as small as 0.012 eV. It is quite different T evolution of spectra from other compounds indicative of the emergence of unconventional ground states.

We discuss the possible electronic states of x = 0.5, which is located near the quantum MIT point. At first glance, the observed T evolution of the spectra is reminiscent of the band reconstruction due to the formation of charge/spin density wave states, in which the SW transfers to right above the optical gap. This is however not likely since the band reconstruction by the folding of Brillouin zone may not occur in the case of all-in all-out type magnetic order. Another possible scenario is emergence of Weyl Mott insulator. It is theoretically proposed that the electronic band can be gapped while maintaining topological aspects by electron-electron correlation. In this state, characteristic absorption peaks due to interband interactions are predicted to show up in optical conductivity, which is not inconsistent with the presently observed results.
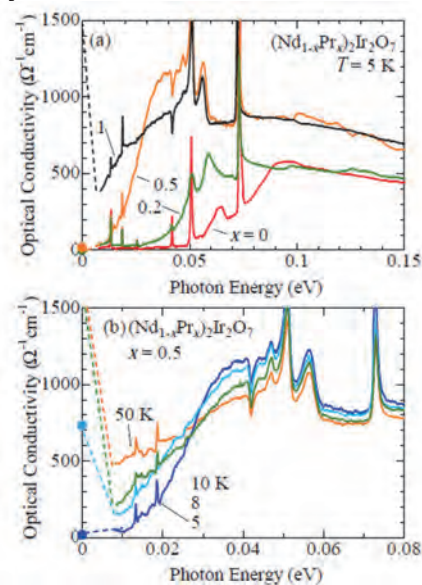

Fig. 1. (a) Optical conductivity spectra for x = 0, 0.2, 0.5 and 1 of R = Nd1-xPrx at 5 K. (b) Optical conductivity spectra at several temperatures for x = 0.5.

[1] X. Wan *et al*., Phys. Rev. B **83** (2011) 205101.
[2] K. Ueda *et al*., Phys. Rev. B **92** (2015) 121110(R).

BL8B

Ultraviolet Photoelectron Spectra of $Sc_3C_2@C_{80}$

T. Miyazaki[1, *], H. Yagi[1], T. Zaima[1], R. Sumii[2],
H. Okimoto[3], N. Izumi[3], Y. Nakanishi[3], H. Shinohara[3] and S. Hino[1]

[1]*Graduate School of Science and Engineering, Ehime University, Matsuyama 790-8577, Japan*
[2]*Institutes for Molecular Science, Okazaki 444-858, Japan*
[3]*Graduate School of Science, Nagoya University, Nagoya 464-8602, Japan*
(*Present address: Faculty of Science, Okayama University, Okayama 700-8530, Japan)

Fullerene cages often encapsulate metal atoms. C_{80} endohedral fullerenes attract attention because of the reasons such as empty I_h-C_{80} is not stable and cannot be isolated but it becomes stable upon encapsulation of metal atoms. Intramolecular charge transfer from encapsulated species to the carbon cage gives them unique and different characteristics from empty fullerenes. $Sc_3C_2@C_{80}$ is one of such endohedral cluster fullerenes and well studied because its highly symmetric I_h cage structure is expected to result in unique properties. Recently, Sato et al. [1] reported considerably high carrier mobility (the highest among the polycrystalline endohedral fullerene films) and high electrical conductivity of polycrystalline $Sc_3C_2@C_{80}$ film compared to those of $La_2@C_{80}$ and $Sc_3N@C_{80}$. Their DFT calculation suggests that high conductivity of $Sc_3C_2@C_{80}$ is attributed not only to the high carrier mobility but also to its small band gap (0.07 eV), and that $Sc_3C_2@C_{80}$ can be considered as a semimetal at room temperature. To examine whether $Sc_3C_2@C_{80}$ really has such a small bandgap, we measured the Ultraviolet Photoelectron Spectra (UPS).

$Sc_3C_2@C_{80}$ was synthesized according to the previous procedures. The UPS were measured by the photoelectron spectrometer at the beamline 8B2 at the Ultraviolet Synchrotron Orbital Radiation Facility (UVSOR), and by our laboratory equipment which consists of He-I, (hv = 21.218 eV) discharge lamp (combination of MB Scientific L-1 and M-1) and a SCIENTA SES-100 electron energy analyzer. All the spectra are referenced to the Fermi level of the substrate, which was determined by measuring the Fermi edge of the gold. The $Sc_3C_2@C_{80}$ specimen for the UPS measurements were deposited by sublimation from a resistively heated quartz crucible.

Figure 1 shows the UPS of $Sc_3C_2@C_{80}$ obtained with hv = 20 ~ 60eV. The spectra exhibit seven peaks denoted as A-G in the figure. The intensity ratios of those peaks oscillate with the incident photon energy, which is due to the spherical shape of the molecule and is the characteristics of the UPS of fullerenes. The onset energy of the UPS (E_{onset}), which is the energy separation between the Fermi level and the valence band maximum, is 0.2 eV for $Sc_3C_2@C_{80}$. This value is much smaller than the E_{onset} of $La_2@C_{80}$ (0.77 eV) and $Sc_3N@C_{80}$ (1.1 eV). The Fermi level of the n-type semiconducting fullerene thin film usually does not situate at the mid gap but closer to the conduction band minimum, so the band gap of $Sc_3C_2@C_{80}$, $La_2@C_{80}$ and $Sc_3N@C_{80}$ is probably between E_{onset} and twice of

the E_{onset}. The small onset energy of $Sc_3C_2@C_{80}$ is qualitatively consistent with the previous DFT calculation by Sato et al. [1] in which the band gap of $Sc_3C_2@C_{80}$, $La_2@C_{80}$ and $Sc_3N@C_{80}$ is estimated to be 0.07, 0.41 and 1.23 eV, respectively.
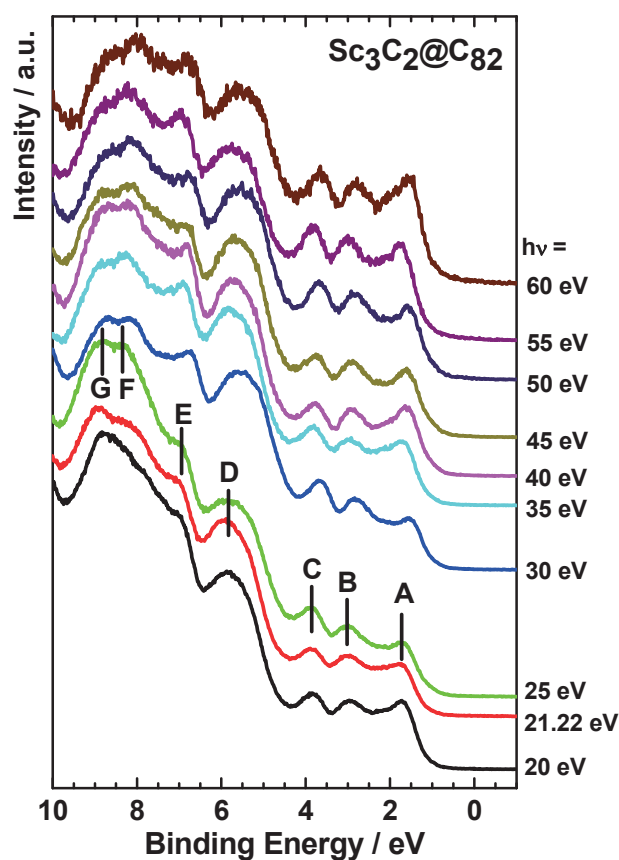

Fig. 1. Ultraviolet photoelectron spectra of $Sc_3C_2@C_{80}$ with incident photon energy at hv = 20 ~ 60 eV.

[1] S. Sato, S. Seki, G. Luo, M. Suzuki, J. Lu, S. Nagase and T. Akasaka, J. Am. Chem. Soc. **134** (2012) 11681.